Ultrafast Charge Separation and Relaxation in Novel Nanostructures

by

Zhen Xu

A dissertation submitted in partial fulfillment
of the requirements for the degree of
Doctor of Philosophy
(Electrical and Computer Engineering)
at the University of Michigan
2023

Doctoral Committee:

Professor Ted Norris, Chair
Professor Zetian Mi
Professor Liuyan Zhao
Professor Zhaohui Zhong

Zhen Xu
xuzhen@umich.edu
ORCID: 0000–0002–6477–8108

Acknowledgments

The experience as a Ph.D. student is a special one, where one is free to and encouraged to explore the cutting edge science and technologies in an inclusive and permissive culture. It is never the easiest or the most cheerful experience due to its nature of making unique original intellectual contributions and the inherent uncertainty in research work itself in addition. My life as a Ph.D. student is accompanied by many that made it a little more enjoyable. I would like to thank them all for their help, in the form of but not limited to financial support, technical consulting, emotional support and simply hanging out with me.

First, I would like to thank my advisor, Professor Ted Norris for his help, support and inspiration throughout my Ph.D. student journey. All the work presented in this dissertation was accomplished in his lab. I would not be able to finish this work without the resources of the lab and Dr. Norris's insight of physics and of research itself. I have learned much that are not easily obtainable elsewhere. I also thank my other committee members, Prof. Zhaohui Zhong, Prof. Zetian Mi, and Prof. Liuyan Zhao for supporting me during my last months of my Ph.D. student life. Our group also have close collaborations with Prof. Zhong and Prof. Mi group. Those experiences are invaluable.

Next I would like to thank my collaborators, Dr. Dehui Zhang, Dr. Zhe Liu from Prof. Zhong group, and Dr. Ayush Pandey and Mr. Arthur Xiao from Prof. Mi group for providing me with the samples and in-depth understanding from the material science's perspective.

I also enjoyed working with my lab mates: Momchil Mihnev, Jessica Ames, You-Chia Chang, Miao-Bin Lien, Gong Cheng, Heather George, Nooshin Mohammadi Estakri, Zhengyu Huang, Yifan Shen, Liangqing Cui and Josey Hanish. I would like to give my special thanks to Jessica and Miao-Bin for their fantastic Labview programs I use for my daily lab work.

I very much admired how you could make elegant and organized Labview programs for controlling our instruments and I learned a lot from reading the code. Gong, and Heather, I enjoyed the months of time we spent doing experiments together. It was from you that I learned the ins and outs of ultrafast experiments and the optics lab techniques. And Josey, I appreciate that you helped me proofread my thesis and provided me with valuable language and writing suggestions. I would also like to thank Prof. Roberto Merlin, who allowed us to continue with experiments in his lab when our laser was down for a year. And Steve Katnik, thank you as always for helping us with laser maintenance and troubleshooting for all these years.

Lastly, I would thank my family: my wife, Linyan, who gave me her most support with love, care, and trust, in the better days and in the darker days, and our two cats Lily and Allyah, for sparing my laptop while trying to chew on everything else.

TABLE OF CONTENTS

Chapter

LIST OF FIGURES

LIST OF ABBREVIATIONS

PMT photon multiplier tube

TRPL time-resolved photoluminescence

DR differential reflectance

TRDR time-resolved differential reflectance

SHG second harmonic generation

DT differential transmittance

TRDT time-resolved differential transmittance

TA transient absorbance

CVD chemical vapor deposition

MOCVD metalorganic chemical vapor deposition

PL photoluminescence

CW continuous wave

SEM scanning electron microscopy

RegA regenerative amplifier

BBO Barium Borate

PTD Porter-Thomas distribution

JDOS joint density of states

IQE internal quantum efficiency

MBE molecular beam epitaxy

SAE selective area epitaxy

FROG frequency-resolved optical gating

ps picosecond

fs femtosecond

KL Kerr lens

CPA chirped pulse amplification

CL cathodoluminescense

PC photocatalysis

ABSTRACT

Nowadays, a significant part of the research interest in optoelectronic devices is in making nanostructures such as heterojunctions, nanowires, quantum wells and quantum dots that dramatically change the electron behavior of the material compared to their bulk counterpart. In this dissertation, we applied ultrafast spectroscopy to study specifically the hot carrier separation and recombination dynamics in the CVD-grown monolayer molybdenum disulfide (MoS_2) and graphene heterostructure, III-nitride quantum well LED structure and self-organized InGaN nanowires for photocatalysis.

By using ultrafast pump-probe spectroscopy, we observed efficient electron and hole separation within a few hundred femtoseconds by interlayer charge transfer from graphene to MoS_2 monolayer following initial excitation and thermalization. The transfer-back process to graphene happens in multiple timescales, the dynamics of which after the thermalization can only be modeled by a Porter-Thomas distribution for the charge transfer rate because the transfer back process after the thermalization is dominated by material disorder.

The III-nitride quantum well has been the most common LED structure since the 1990s. III-V compounds are also the only known material that can have tunable valence and conduction band levels that cover the chemical potential of a few important photochemical reactions such as water splitting and methane oxidation thus making them ideal for photocatalysis in converting solar energy into electrochemical energy. We studied the time-resolved photoluminescense (TRPL) and the time-resolved differential reflectance (TRDR) of the self-organized InGaN nanowires observed a fast decay component in the PL decay dynamics that were not observed in the DR measurements only when the InGaN is p-doped. We argue that the fast decay component in the PL decay dynamics indicates the charge separation due to the built-in polarization field near the surface of the nanowires. We also studied the temperature-dependent TRPL experiments and room temperature TRDR of the quantum disk-in-wire micro-LED structure that contains tilted quantum wells grown along the semi-polar facets. The TRPL decay curves always show faster dynamics than the TRDR. This is modeled with a thermal activated non-radiative process that can be explained with Arrhenius's Law applied to the lateral charge transport over

the local indium composition fluctuation.

Throughout this thesis, we study the ultrafast charge separation and relaxation by direct probing and by combining the PL and DR dynamics in different nanostructures. We have demonstrated a novel approach for detecting carrier spatial separation and the results revealed the important microscopic physics such as material disorder, band bending and local fluctuation that are crucial for future research and development.

CHAPTER 1

Introduction

The optoelectronic materials and devices are an essential part of communications, computations, lighting, display, imaging, clean energy, and many others. Traditionally the most widely used optoelectronic materials in photodetectors, a major category of optoelectronic devices, are based on silicon, where its carrier density, Fermi levels and conductivity can be dramatically changed via doping with family III or V atoms thus enabling the device physics research and device structure development of LEDs, photodiodes and phototransistors. The 1970s to 1990s saw the development of III-V compound systems for light emitting and light sensing applications. These materials have direct bandgap which can be engineered by incorporating two kinds of III-V compounds to form mixed crystalline alloys. More recently researchers have been exploring the possibilities of new materials and structures that create higher performance devices: high responsivity, high operation speed, or wide sensing bandwidth range.

The physical process of light and matter interactions in the optoelectronic materials and devices frequently involves the separation, scattering, tunneling, diffusion, and recombination of charges. The device physics largely involves investigating and harnessing the charge carriers in the optoelectronic material systems, and understanding the charge carrier dynamics is crucial for the study, design and development of optoelectronic devices. For example, Figure 1.1 shows the band diagram of an el-

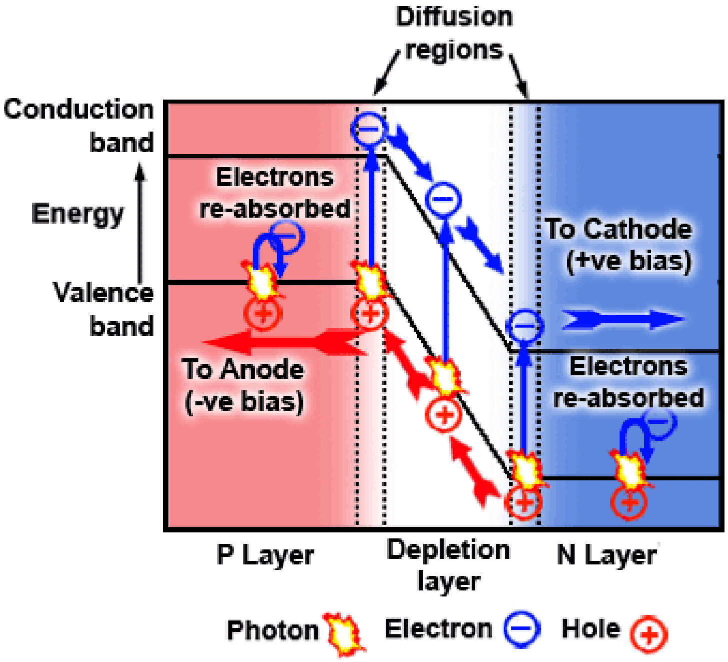

Figure 1.1: The operation of a photodiode illustrated with band diagram.

ementary photoelectronic device, the photodiode which essentially consists of a PN junction. The photon detection process involves the creation of electron and hole pairs by photo-excitation in the active region, the separation of the e and h, and the signal extraction or the charge carrier extraction to accomplish the conversion from the optical signal to the electric signal. The signal conversion efficiency, in one part, depends on the conversion rate in the active material, on the other part, depends on the charge carrier extraction efficiency after they are created. And the carrier extraction process is an interplay of carrier separation, scattering, transport, and recombination. Efficient photodetectors will need fast charge separation, fast transport to the metal contact, and slow scattering and recombination. In the applications where the responsiveness of the photodetector is required, the fast recombination, which means a shorter time it takes to return to the equilibrium will be desirable.

Experimental study of charge carrier dynamics will help resolve the physical process that is happening in the optoelectronic devices thus guiding the device physics design. Similarly, the light emitting devices involves the injection of electrons and holes into the active region and the radiative recombination, while competing with the non-radiative side channels. While a large part of the development of the next-generation semiconductor devices are on the fabrication process, device structure design, and utilizing novel materials, studies on the fundamental physics, especially the carrier dynamics in the semiconductor systems have made been guiding the development of the optoelectronic devices. Understanding the mechanisms and the physical processes in the semiconductor systems is a driving force and an important part of developing and engineering the novel optoelectronic materials and structures.

Other than the traditional bulk materials researchers have explored a wide range of other semiconducting nanostructures, most notably 2D layered materials and their heterostructures, and the III-V compounds and their quantum well and nanowires. The purpose of utilizing the nanostructures in most of the time are twofold: (a) to utilize the quantum confinement of the nanoscale interfaces and modulate the electronic states, and (b) to leverage the nanoscale size for increased charge separation and charge transfer efficiency.

In this dissertation we will utilize the ultrafast pulsed lasers to directly observe in the time domain the dynamics of electrons at the scale of femtoseconds to picoseconds in those recently developed novel nanostructures made for various optoelectronic applications. The techniques we are going to use are the ultrafast differential reflectance/transmittance pump-probe spectroscopy and the time-resolved photoluminescense measurements accomplished with a streak camera. The charge carrier dynamics in three semiconductor nanostructure systems, the 2D material heterostructure, III-nitride (III-N) quantum well in nanowires, and the photo-catalytic III-N nanowires, will be studied in details in this dissertation. We will try to combine the techniques of spectroscopy and time-resolved measurements with the previous understanding of the physics to explore and understand a little more about these new nanostructure systems.

To fully understand the studies presented here it is crucial to know the details of the techniques applied here. In the next chapter (Chapter 2) we will primer the reader with the techniques that we use in the research presented here. We will introduce the necessary details of the ultrafast time resolved spectroscopy techniques including the pump-probe technique, which was developed following the invention of high peak power pulsed lasers in the 1990s, for temperally resolving the physical processes that happen in the scale of femtoseconds (fs) to picoseconds (ps), and the streak camera instrument that we will be using to study the time dependent photoluminescense (TRPL).

The next two chapters (Chapter 3 and 4) are related to the studies on the charge carrier dynamics in the three nanostructures. In Chapter 3, we will first introduce the previous studies of the similar heterostructure systems and the motivations of this study. Then we will present our discoveries on the charge transfer process in two-dimensional (2D) material heterostructures. We study specifically the most common 2D materials, graphene and MoS_2, all grown with the chemical vapor deposition (CVD) technique. These materials, as a layer cleaved from their bulk counterparts that have layered structures, have very distinct electronic and optical properties and are potentially high performance building blocks for finely engineered optoelectronic applications. We will see how the time resolved ultrafast experiments can look into the electronic structures of the materials and guide the development of novel micro and nano devices.

The next two systems we will be looking into after the 2D heterostructures is the III-nitride quantum well systems and self-assembled III-nitride nanowires. We mention them together because the central part of the two material systems are both InGaN, a ternary alloy of III-nitrides, thus sharing the backgrounds. The family of III-V compounds have very similar lattice structure and can form uniform alloys, the bandgap energy of which can be engineered by tuning the mixing rates of the base components. The study of III-nitride materials became prominent since 1990s with the development of quantum well light emitting diodes (LEDs) in the blue light to UV range. Recent studies of our group and collaborators involves exploring the possibility of making LED materials with high efficiency in the green light range, and of making the semiconductor photocatalyst based on the III-nitride nanowires for the purpose of water splitting or the synthesis of ammonia or aromatic organics. This dissertation will focus on the hot carrier dynamics studies instead of the material growth or chemistry. In Chapter 4 we will first introduce the relevant previous results and motivation of our studies. We will then present the experimental study of the carrier dynamics of the self-organized InGaN nanowires and the InGaN quantum well in nanowires, motivated by photocatalysis and high efficiency LED applications, respectively. We found evidence of charge separation in both the self-organized nanowires and the quantum well in nanowires systems. This is desirable for the photocatalysis purpose, but unwanted for the LED application. We find that the nanostructure plays a crucial role in the carrier dynamics. Additionally, the combination of two kinds of ultrafast spectroscopy demonstrated a novel approach for characterizing the charge separation in the nanostructures. We will lastly conclude this thesis with a brief summary and outlook in Chapter 5.

CHAPTER 2

Ultrafast Spectroscopy

Optical spectroscopy is an essential tool for physics, material science, biology, astronomy, and chemistry because it provides us with in-depth understanding of the object in a non-invasive manner with great detail due to the close connection of electronic and atomic structures and the light-matter interaction. The development of spectroscopy has lead to some of the most important findings in the history. Along with the development of lasers since its not-so-long journey of only a few decades starting from the 1960s, where researchers have been seeking the techniques of creating extremely strong coherent optical field using the techniques of Q-switching, mode-locking and pulse amplification techniques, nowadays, we have much more reliable access to laser pulses that are shorter than 100 femtoseconds (10^{-15}s) and with a peak power of tens of megawatts. This chapter will introduce the methods we utilized in our studies. The short pulse duration, as a "ruler" in time, provides us with a tool to directly observe the very fast physics that happens within picoseconds.

In this dissertation, we will be utilizing two ultrafast time resolved spectroscopy techniques to study the charge carrier dynamics in the semiconductor nanostructures developed in the recent years: the ultrafast pump-probe experiments, and the streak camera.

First we will introduce the ultrafast pump-probe spectroscopy. In the literature it can be referred to by a few different names, time-resolved differential transmittance

(TRDT) or time-resolved differential reflectance (TRDR), pump-probe spectroscopy, or transient absorbance (TA). It utilizes two pulses that are strictly synchronized with a controlled variable delay, with one pulse hitting the sample slightly earlier than the other, to measure the transient change of optical properties of a system, which characterizes the ultrafast physical dynamics. When the first pulse (called "pump") hits on the sample the light-matter interaction perturbs the sample system off its equilibrium (through heat, single photon absorption, multi-photon absorption or other forms of light-matter interaction) causing its optical properties to change. And when the second pulse (called "probe") arrives at the sample it will sense the change and how much the sample is off equilibrium, and a differential measurement on the probe signal that is dependent on the pump-to-probe delay can reconstruct the transient dynamics after the excitation of the pump pulses. Since this measurement is not carried out in a straightforward manner, but on the other hand make up a major part of the research of this dissertation, it is important to understand this technique thoroughly. In the following parts of this chapter, we will describe in detail the experiment setup, the common decision choices, the common mechanisms of the measured signal, and the related physical processes.

The other ultrafast spectroscopy technique, or more accurately, instrument, utilized in the experiments is the streak camera. The streak camera is an example of pushing the electronics to its limits to achieve almost the highest possible time resolution by electronic engineering. It has a photocathode screen that emits electrons upon the arrival of photons. The photo-electrons are biased and accelerated towards a phosphorous screen that images the arrival of the photo-electrons. The timing of the electron emission can be considered the same as the photon arrival. Then a perpendicular electric field that scans at a certain rate will be spatially dispersed. Since the time-resolved mechanism is pure electronic the time resolution of this technique is instead limited by the electronic circuits and their parameters. The streak camera technology has been improving since the 1990s, and the time resolution can achieve the order of 1 ps these days, which gives us tools of measuring the transient dynamics such as the PL or cathodoluminescense (CL) of semiconductor materials. We will be utilizing a streak camera to measure the time-resolved photoluminescence (TRPL) of our samples and compare the PL dynamics with the DR to draw some interesting physical conclusions in the coming chapters. Since the streak camera is usually in the form of manufactured instruments we will not go into details about the mechanisms. For this chapter, we will be describing the basic principles, the specifications of the instrument and our setup for measuring the TRPL.

2.1 Pump-probe experiments

Optical and electronic measurements we have access to all rely on the electronic signals. The most common instrument for optical detection is the photodiode detector that converts photons into photo-electrons, which can then be collected by the electrodes to create a photo-current signal. The bandwidth of normal photodiode detectors is limited to the electronic time constant (the RC constant) of the measurement circuitry, which can hardly go above tens of gigaherts (corresponding to an electronic time constant of sub-nanoseconds). Any time-domain dynamics faster than the response time of a normal photodiode including the femtosecond laser pulse shape that is normally about tens of femtoseconds will get completely smoothed out to the detector's intrinsic electronic response timescale. Practically the fastest photodiodes are capable of separating the femtosecond (fs) pulse trains generated by the Ti:sapphire lasers, which can have a repetition rate ranging from 100 MHz to kHz, but they are never able to trace the shape of the pulses. The pump-probe technique, which was developed after the invention of mode-locked lasers, was devised to reconstruct the time domain signals with the resolution comparative to the pulse duration used for the measurement, without relying on extremely fast photodetectors.

2.1.1 Ultrafast laser source

The excitations sources used for the pump-probe experiments are the pulsed lasers. Initially the mode-locking technique was invented to overcome the peak power limit of continuous wave (CW) lasers. In a CW laser, the gain medium is operated with saturated population inversion where the electron population pump is balanced with the depletion due to the stimulated emission. The idea of pulsed laser is that instead of letting the gain medium amplify the laser signal at all times, one can suppress the laser signal to let the inversion build up when the laser is not lasing. When the laser cavity resumes lasing, the elevated inversion provides a much higher amplification of the laser signal that rapidly depletes the inversion, creating a sharp pulsed laser emission. This is achieved through the mode-locking technique. More details of mode-locking techniques can be found in ultrafast optics textbooks[1].

The output of a mode-locked laser is a periodic train of pulses, the intensity in time domain of which, if we denote the periodicity as T, can be described with a convolution of a comb function $C(t) = \sum_{n=-\infty}^{\infty}$ with a pulse shape function $P(t)$: $I(t) = C(t) \otimes P(t)$. In practice one actually only has access to the average power (P) of a pulsed laser beam due to the bandwidth limitation of normal photodiode or bolometer based power calibration mechanisms, we will usually use two numbers, the average power and the repetition rate to estimate the pulse energy, between which the repetition rate is a design parameter of the laser source that is only rarely changed. When the pulse is a transform-limited Gaussian pulse, the pulse energy and duration will provide a reasonably accurate estimate of the peak intensity of the pulse, and for a semiconductor system, the charge carrier injection density.

One of the most common pulsed laser system, which is the laser source used in this work, is the Ti:sapphire based solid-state mode-locked laser system that are nowadays available as commercial modules. The main components of the laser system are a passively mode-locked Ti:sapphire oscillator seed and a chirped pulse amplification (CPA) system which consists of a pulse stretcher, a regenerative amplifier (RegA) and a pulse compressor. The passive mode-locking of the oscillator is achieved through a Kerr lens (KL), which consists of a self-focusing crystal and an aperture, acting as a fast saturable absorber in the cavity which suppresses the CW signal in the laser cavity through increased loss from clipping at the aperture. The pulsed signal will be able to pass the aperture due to decreased beam profile size as a result of self-focusing effect. In the experiments presented in the following chapters, we use an oscillator that operates at about 76 MHz with a maximum average power output of about 500 mW. The RegA by itself (meaning without the input of previous stage laser pulses) is a Q-switched laser that operates with a pump source and an alterating modulator. The output of the oscillator is stretched to a longer pulse with a reduced peak power by introducing chirp with a pair of gratings (the pair of gratings effective consist the pulse stretcher we just mentioned) thus avoiding saturating the amplifier and then sent to the RegA cavity. The pulses are amplified in the RegA cavity during the high Q half cycle and a pulse dumper synchronized with the Q-switch will pick off the amplified pulses right after it reaches the max pulse energy. After the amplification, the pulse will be compressed with another pair of gratings to cancel the chirp and shorten the duration. In the experiments presented in the following chapters, we use a RegA system that has a repetition rate of 250 kHz and an average total output power of about 1.2 W.

2.1.2 Autocorrelation and crosscorrelation

Historically the researchers studying the ultrafast optics have widely utilized the nonlinear effects for characterizing ultrafast laser pulses even if we never have a detector responding as fast as the laser pulses, most notable techniques being the autocorrelation and the crosscorrelation of ultrafast pulses. The frequency-resolved optical gating (FROG) is another good example of the application of nonlinearity for characterizing the ultrafast laser pulses[2]. We will use autocorrelation as an example to first demonstrate the idea behind the ultrafast time-resolved measurement techniques. Instead of directly tracing the pulse shape with some photodetectors in the hope of them being fast enough, one can use the pulse itself to make the "comparison". In this measurement (with a typical schematic shown in Figure 2.1), the beam is split into two paths; one of them will go through a controlled delay before it merges with the other path and hit on a piece of $\chi^{(2)}$ material. With the second order nonlinear effect, there will be the second harmonic generation (SHG), the intensity of which is proportional to the square of the total intensity of the two split pulses. For simplicity, we can assume that the two paths are split evenly, each having the same intensity $I_1 = I(t+\tau)$, and $I_2 = I(t)$. They are time dependent because they are, after all, pulse trains: $I(t) = \sum_{n=0}^{\infty} E(t+nT)$, E(t) denoting the pulse shape function. The SHG can be written as

$$\begin{aligned} I_{SHG} &= \chi^2\big(I(t) + I(t+\tau)\big)^2 \\ &= \chi^2[I(t)^2 + I(t+\tau)^2 + 2I(t) \cdot I(t+\tau)] \end{aligned} \tag{2.1}$$

Now since the detector is much slower than the pulses, it only sees the average SHG intensity. With the averaging, the first two terms are the average intensity squared of one pulse, which are simply constant. The detected signal then is given by

$$S_{SHG} = \beta < I_{SHG} >= 2I_0^2 + 2\int_t I(t)I(t+\tau) \tag{2.2}$$

Other than the constant terms, there is a cross correlation term of the two paths that depends on τ, the timing difference between the two pulses.

The main idea of autocorrelation and crosscorrelation is that instead of directly

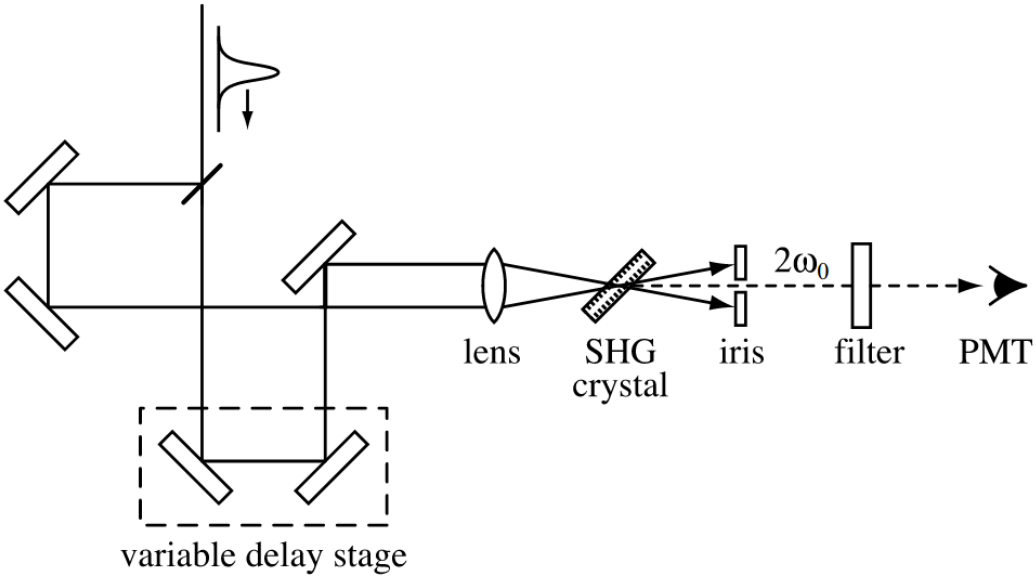

Figure 2.1: A schematic diagram of a (background-free) autocorrelator setup

measuring a fast pulse shape by naively relying on a fast enough photodetector, a delay is used to sample the pulse and reconstruct the pulse with a varying delay τ, and result of this measurement is not dependent on the response time of the detector.

The pump-probe technique employs a similar idea as the autocorrelation or cross-correlation in that the time-resolved measurement is also reconstructed from the sampled optical response of the material perceived by the probe pulse, similar to the schematics of the autocorrelation, with varying the delay between the two paths, For each delay time τ, the system is kept steady with repeated pump and probe pulse trains, thus making repeated measurements of the transient optical response, in the case of this dissertation the transient differential reflectance and transmittance, and then the measurements of the differential signals are repeated for an array of controlled delay times. Fig. 2.2 shows a schematic diagram of a typical non-degenerate pump-probe differential reflectance setup.

The delay control is implemented with a linear motorized stage with its direction of motion aligned with the incident beam and sending it back in the same direction.

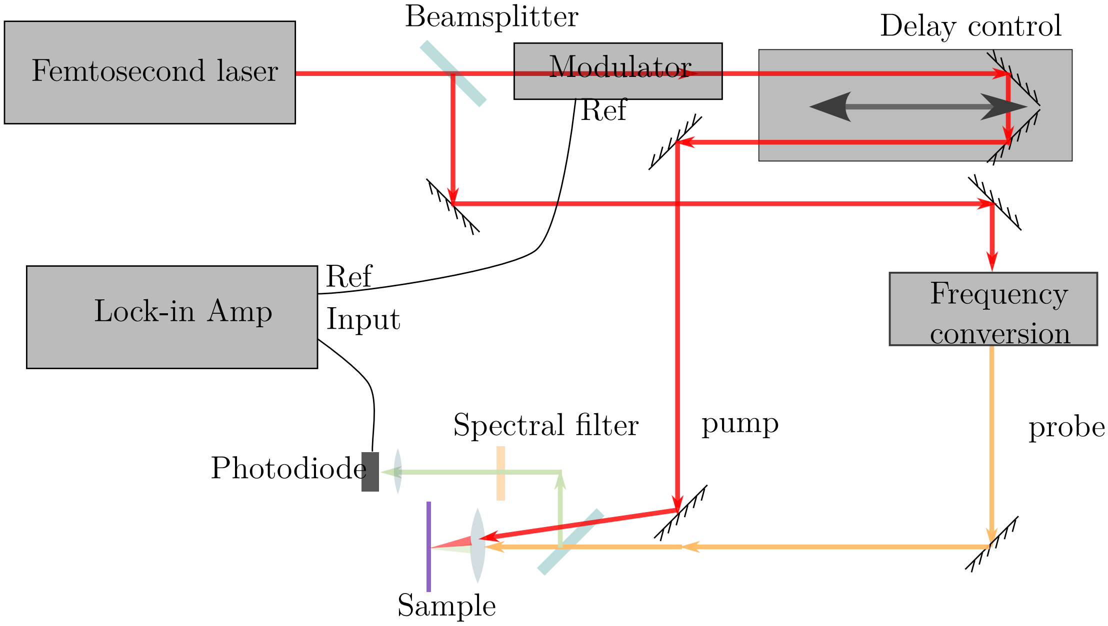

Figure 2.2: A schematic diagram of a bare bones (non-degenerate) pump-probe differential reflectance setup.

This ensures that only the pulse timing is changed while not losing its pointing direction. In order for this schematic to work, the pump and probe beams should also overlap well on the target sample at the focus of the lens (lenses if the two paths are focused separately).

2.1.3 System response

To demonstrate how the measurements are conducted we first simplify the experiment setup a bit. For this part we can just take it for granted that upon the excitation of the pump pulses, the perturbed system to be measured will change its optical properties, which are usually measured by its complex dielectric function $\tilde{\epsilon}(\lambda)$ or equivalently the complex refractive index $\tilde{n}$. In some works these are also expressed as the complex optical conductance $\tilde{\sigma}$. Off from its original dielectric function $\tilde{\epsilon}_0$, the perturbation of the pump introduces a change, denoted by $\Delta\tilde{\epsilon}$, can cause a change of the transmission of the probe pulse through the sample, or cause a change of the reflection off of the sample. The measurement of the pump-probe experiments are based upon the differential measurements of the reflectance and or the transmittance, thus we interchangeably call them differential reflectance (DR) or differential transmittance (DT), corresponding to measuring the $\frac{\Delta R}{R_0}$ and $\frac{\Delta T}{T_0}$, and we call the measured quantities the relative DR and DT, respectively. In most of the cases, the amount of relative DR or DT is in the range of 10^{-2} to 10^{-4} level, which are quite small, so they can be reliably used to estimate the relative change of the dielectric constant $\frac{\Delta\epsilon}{\epsilon_0}$.

But how can the instruments sense the differential signal? We start with the Dirac delta function pulse trains for the excitations sources (both the pump and the probe) to find the Green's function for the measured signals. Assume that the impulse response of the differential transmittance rate is $H(t) = H(t)\eta(t)$ where $\eta(t)$ is a unit step function in the form $\eta(t) = 0$ for any $t < 0$, and 1 otherwise. In other words, when there is a unit delta function excitation $I(t) = \delta(t - t0)$ on the system, here using transmittance as an example, the transmittance response of the system can be written as $T(t) = T_0 + \Delta T(t) = T_0 + H(t - t_0)\eta(t - t_0)$. And assuming that the system has a near linear transmission, the laser that transmits the sample should also be given just by $I_{\text{trans}}(t) = T(t) \times I'(t) = T_0 I'(t) + \Delta T(t) I'(t)$. Again here we are only writing down the DT directly without any detailed deduction, which we will cover in the coming parts. Both the pump and the probe are ideal unit pulse trains with infinitesimal pulse duration (delta functions), so we denote the pump as $I(t) = \sum_{k=-\infty}^{\infty} \delta(t - kT_r)$ and the probe as $I'(t) = \sum_{k=-\infty}^{\infty} \delta(t - kT_r - \tau)$, where T_r is the pulse repetition intervals, and τ is a controlled delay between the two pulse trains. Here we assume an infinitely long pulse trains in order find out the steady state and τ is limited to be between 0 and T_r without losing any generality.

Upon the excitation of the pump pulses the differential transmittance coefficient response of the system is given by

$$\begin{aligned} \Delta T(t) &= I(t) \otimes H(t) \\ &= \sum_k H(t - kT_r)\eta(t - kT_r) \end{aligned}. \tag{2.3}$$

The probe pulses that goes through the sample system will be modulated by the transmittance, so the probe pulse becomes

$$I'_{\text{trans}}(t) = \sum_{m,n} H(t - mT_r)\eta(t - mT_r)\delta(t - nT_r - \tau) + \sum_n T_0\delta(t - T_r - \tau) \tag{2.4}$$

as opposed to the transmitted probe pulse without the pump which is simply $I'^{(0)}_{\text{trans}}(t) = T_0 \sum_n \delta(t - T_r - \tau)$, and I'_{trans} is identical to the second part of the I'_{trans} in (2.4).

2.1.4 Detection

Under the assumption that the detector is much slower than the laser pulses, the readouts are simply averaged over the pulse cycles; the difference of the average probe power is then

$$G(\tau) = \frac{1}{T_r}\int_0^{T_r} (I'_{\text{trans}} - I^{(0)}_{\text{trans}})\mathrm{d}t = \frac{1}{T_r}\sum_{m=0}^{\infty} H(\tau + mT_r) \approx \frac{H(\tau)}{T_r} \tag{2.5}$$

When the impulse response $H(t)$ is much faster than the repetition interval, i.e. $H(\tau + mT_r) \ll H(\tau)$ for $m > 1$, which is the case in most of the practical situations, the measured signal can be reduced to $G(\tau) = \frac{1}{T_r}H(\tau)$, and, with a controlled varying delay τ, it reconstructs the impulse response of the system's absorption rate.

It is trivial to verify that the measured signal at the detector $\Delta\bar{I}'_{\text{trans}}$ is a bilinear function of the two inputs, pump $I(t)$, and probe $I'(t)$. In reality the pulses have widths, and they can be expressed with a convolution of an envelope function $p(t)$ with the delta function pulse train: $I(t) = p(t) \otimes \sum_m \delta(t - mT_r)$. Therefore, when taking into consideration the pulse shapes of both the pump and the probe, the measured signal is a convolution with both the pulse shapes

$$\Delta T_m(\tau) = \int_{t_1} \int_{t_2} p_{\text{pump}}(t_1) p_{\text{probe}}(t_2) G(\tau - t_1 - t_2) \tag{2.6}$$

2.1.5 Charge carrier dynamics in semiconductors

Now we get down to how the perturbation of the pump changes the dielectric function. First, the dielectric function of a material system is closely tied with the electronic structure, in the case of semiconductor and solid-state materials, the band structure and the excitonic states[3, 4]. The main mechanism for photon absorption in the solid-state materials in the optical wave range is the interband transition. The imaginary part of the dielectric function, or the real part of photoconductance, which corresponds to the optical transition rate is determined by the Fermi's Golden Rule, which, in solid state systems, should be

$$\Gamma(\omega) = \frac{2\pi}{\hbar} \int_{\text{BZ}} \frac{\mathrm{d}\mathbf{k}}{4\pi^3} \langle \psi_c | \hat{V} | \psi_v \rangle \delta(E_c(\mathbf{k}) - E_v(\mathbf{k}) - \hbar\omega) \tag{2.7}$$

where the polarization Hamiltonian $\hat{V}$ is normally the dipole Hamiltonian $\hat{V} = \mathbf{E} \cdot \mathbf{p}$, $\mathbf{p}$ being the dipole moment of the electron-hole pair. The equation given above is the single electron approximation. When we consider the ensemble average we should put in the joint density of states (JDOS) and the occupation rate of the electrons and holes, and the optical transition rate is proportional to all of them:

$$\Gamma(\omega) \propto (\mathbf{E} \cdot \mathbf{p}_{vc}(\omega)) \rho_{vc}(\omega)(1 - f(e))(1 - f(h)) \tag{2.8}$$

ρ_{vc} is the JDOS at the given optical transition that depends on the band structure, in other words, the dispersion relationship of electrons at the given transition; $p(\omega)$ is the matrix element of the dipole momentum, and $f(e)$ and $f(h)$ are the occupation functions of electrons and holes, respectively. The same form is also seen in the context of PL spectroscopy. For a downward transition that is related to the PL emission, the PL spectrum will correspond to $\Gamma_{\mathrm{PL}}(\omega) \propto E \cdot p_{vc}(\omega)\rho_{vc}(\omega)f(e)f(h)$ in a bulk material. At equilibrium we can approximately consider $f(e)$ and $f(h)$ to be nearly 0. With free carrier occupations present, the most common effect is the occupation of states where both $f(e)$ and $f(h)$ increase due to photo-excitation. If we consider the probe tuned to the band edge that corresponds to an interband transition, after the excitation of a pump pulse, the differential optical conductivity real part $\mathrm{Re}\Delta\sigma$, which corresponds to Γ/E, should be

$$\mathrm{Re}(\Delta\sigma) \propto -p_{vc}(\omega)\rho_{vc}(\omega)(f(e) + f(h)) \tag{2.9}$$

Here we notice two things: (a) the $\Delta\sigma$ is proportional to the sum of the electron and hole occupation and (b) when there is a positive electron and/or hole occupation the optical conductivity decreases. In other words, the absorbtion decreases and the transmission increases. This is also why this effect is sometimes also called “bleaching”.

Shah in his book divides a typical carrier relaxation process upon pulsed excitation in bulk semiconductor systems into four regimes according to the delay timescale and the dephasing time: coherent regime, non-thermal regime, hot-carrier regime, and isothermal regime[3]. We can picturize the carrier dynamics that happens after an optical excitation in a descriptive way. The initial excitation with an ultrafast pulse is described by the optical Bloch equations, where the incident electromagnetic wave creates the excitations in electronic states that are coherent with the optical field. This is often described with a density matrix of electronic states that are correlated, meaning that the off-diagonal entries are non-zero. The free carriers will scatter and dephase into thermal states that has a much higher temperature than the lattice where the carriers are uncorrelated. Depending on the material systems, the decoherence happens in the timescale of femtoseconds to a few picoseconds. The free carriers will then thermalize with the lattice to reach a thermal equilibrium and lastly recombine and return to the ground state. When we recall the relationship between the optical conductivity and the electron and hole occupation in Equation(2.9), we see that all of the four phases will have contributions to the differential optical conductivity according to the photo-carrier occupation. For the majority of the works introduced in the next few chapters of this dissertation, we focus on the noncoherent electronic states, namely after the scattering and dephasing process.

2.1.6 Lock-in amplifier

In the pump-probe experiments the experimentalists usually estimate the signal levels by their relative DR or differential transmittance (DT) levels, which is $\frac{\Delta T}{T_0}$. For simplicity, we will only mention the DT in the following part without losing generosity. It is an indicator of both the practical signal level measured by the electronics, and an indicator of the level of perturbation since it is comparable to the relative differential dielectric function. The relative DT is usually less than the order of 10^{-3} depending on the sample and the optical system. Actually, it should not be too large as we would like to only perturb the system with a minimal effective excitation. Unfortunately the noise level of photodiodes, laser fluctuations, drifts, and electronic noise of the signal processors can easily exceed the level of 10^{-3} and overwhelm the tiny change of transmittance.

There are multiple approaches of making differential measurements, and the most common being the boxcar gated averager and the lock-in amplifier, referenced to a modulator on the pump beam. The principles of these two methods are very similar and comparable. In the work presented by this dissertation, a lock-in amplifier (SR-

850) is used to make the differential measurements. A lock-in amplifier essentially is an electronic instrument that is sensitive to the signal at a certain frequency[5], which is the frequency of a reference signal.

In the pump-probe experiments, modulation is applied on the pump path to turn it on and off at a fixed frequency f. In the experiments presented in the works here, the modulation is achieved with an optical chopper that blocks the beam at a controlled frequency. Electro-optical modulators (EOM) and acousto-optical modulators (AOM) are also common choice of modulation sources. The chopper module provides the reference signal for the lock-in amplifier obtained from an IR photodiode sensor close to the spinning blade surface that monitors the on-off frequency in the form of a square wave. The lock-in amplifier generates a pair of single frequency sine waves or square waves orthogonal to each other (i.e. having a phase difference of $\pi/4$) with the same frequency f, and a multiplier that effectively integrates the inner product of the input signal and the generated reference signals. Effectively the multiplier made a Fourier transform to the input signal and shifted the Fourier component at frequency f in the input to a DC component as a result. The output of the multiplier is then filtered with a low-pass filter to separate the DC component, which corresponds to the frequency component at the reference signal frequency.

We then recall that, according to Section 2.1.3 and upon the excitation of the pump pulses, the photo-carrier occupation induces a transient change of the optical conductance that is proportional to the electron and hole occupation rate (happening usually in the timescale of femtoseconds to picoseconds in the semiconductor systems), and this transient change is then sampled by the probe pulses at the delay time defined by the OPL difference from the pump path. We can now pick off from Eq. (2.6) and consider the resulting probe average power at the detector with an ideal square wave modulation on the pump

$$T_{\text{chopped}}(t+nT;\tau)=\begin{cases}T_0, & T/2\geq t>0\\ T_0+\Delta T_m(\tau), & 0\geq t>-T/2\end{cases} \tag{2.10}$$

Here we actually oversimplified the detection a little because in reality although not perfectly, but a normal photodiode detector which has a response time of tens of nanoseconds is still able to separate the pulse trains in our experiments which have a repetition rate of 250 kHz. Nonetheless, the lock-in amplifier, by integrating the inner product of the input probe signal T_{chopped} and the reference signal, will filter out the background and result in an average differential probe transmission. We then recall that with a positive change in the e and h occupation $f(e)$ and $f(h)$, the optical conductance decreases, so the bleaching will result in a positive differential transmission signal. Also notice that we have not mentioned the phase of the reference signal but only assumed that it is in-phase with the modulation on pump; the differential measurement mechanism of the lock-in amplifier actually only works when the reference is in-phase, which is actually never real. Practically we are allowed to tune the phase of the internally generated reference signal and align it to the pump modulation by maximizing the lock-in output while let the modulated pump beam hits on the detector before making pump-probe measurements when the pump is eliminated.

2.1.7 Practical design decisions

After we explained the principles we then discuss the practical decisions of a pump-probe setup since experimentalists need to deal with the unideal factors, perturbations and noise.

First, the time resolution of a pump-probe setup, which is the sensitivity in the time domain of τ, is conventionally described with a point-spread function. If we imagine an ideal system with an infinitely sharp impulse response of differential transmission signal, and measure the pump-probe signal with two pulses, we will get the $\Delta T(\tau)$ curve in the shape of the convolution of the pump and the probe pulse shapes (i.e. the cross-correlation) according to Eq. (2.6).

Secondly the the noise level. We would not be able to make measurements unless the signal level stands out from the noise. There are mainly three sources of noise: the laser fluctuation, the optic component drift, and electronic noise. The drift is mainly the low frequency drift related to thermal and mechanical perturbations to the optical components and to the optical paths. Sometimes systematic drift can happen, too. For example, the stage can become misaligned that will change the overlapping conditions of the pump and probe beams so the ΔT vs x_{stage} curve actually measures the overlapping conditions instead of the actual delay time dependent DR curve. Even when the delay stage is not dramatically misaligned, we normally cannot guarantee a perfect alignment. For that reason we will usually make the pump beam slightly bigger than the probe beam and move the delay of the pump instead of the probe. The electronic noise behaves as a white noise in the signal, that is, it appears as a noise floor in the measured signal. Two most common approaches for dealing with white noise are through amplification of the source signal and through prolonged integration time or averaging multiple measurements. The laser fluctuation is mainly the so-called $1/f$ noise or pink noise for a semiconductor laser used in this work[6]. It is best suppressed with increased modulation frequency. For our experiments we usually find that with 1 kHz of modulation frequency, we saw diminished return of reducing the noise level from increasing the modulation frequency. Therefore, we used a chopping frequency of 1 kHz for the pump-probe experiments in the following parts.

Last but not the least we need to consider the signal itself. Needless to say, increasing the excitation power will increase the DT/DR signal, but there are a few limitations:

1. The average power density shouldn't heat the sample too much or damage the

sample. The thermal effect should be discussed.

2. The peak power density, which is normally characterized by the pulse energy fluence, should not exceed the damage threshold.

3. The power density contrast between the pump and probe should be large enough to be able to ignore the excitation from the probe pulse itself. When the probe pulse is too strong, the early part of the probe can bleach the sample by itself thus giving no differential signal.

4. We also need to consider the saturation of the photodetector. The average total probe power should fall in the linear response range of the detector. This can be resolved by attenuating the probe before the detector.

2.1.8 Missing parts

In the above sections we have introduced the basics of ultrafast pump-probe principles and the practical considerations. There are still factors we have not been able to elaborate. One thing is the modeling of the dielectric structure of the specific physical systems. We mainly used the real part of optical conductance to explain the differential signal. It is mostly true for differential transmittance, but the differential reflectance can be related to both the real and the imaginary parts of the optical conductance. We will discuss them in their specific chapters later. We also have not mentioned the coherent effect between the pump and probe, mainly because we only conducted non-degenerate pump-probe experiments in this dissertation. But the coherent effect can be significant for the degenerate case, namely when the wavelengths of the pump and probe are the same. Lastly we only considered the DT signal of equivalently a two level system. The interpretation can be more complicated when involving multiple transitions or many-body effects.

2.2 Streak camera and TRPL

In this dissertation, we will also be using the streak camera to measure the TRPL. The streak camera is an instrument that is able to resolve the time dependent optical signal with electronic approaches. Figure 2.3 is a schematic diagram of a streak camera provided by Hamamatsu, a major manufacturer of streak cameras. A streak camera uses a photocathode screen to turn the photons into electrons and project them onto a phosphorous screen while scanning a transverse electric field synchronized with a trigger signal of the input laser pulses. The synchronized scanning transverse bias diverts the photo-electrons and spatially disperse them according to their timings similar to an old-style cathode-ray oscilloscope so that the phosphorous screen is able to measure the time-resolved photon counts of the input signal. We use a Hamamatsu C10910-01 streak camera coupled with the exit turret of a spectrograph that also disperses the input PL by spectrum. In the TRPL experiments we use the oscillator that has a repetition rate of about 76 MHz as the sample excitation source as well as the trigger source for the streak camera. The PL signal of the sample is collected by the same focusing lens and imaged to the entrance slit of the spectrograph in front of the streak camera. As we briefly mentioned in Section 2.1.5, the PL signal follows $\Gamma_{\mathrm{PL}} \propto (\mathbf{E} \cdot \mathbf{p}(\omega))_{vc} \rho_{vc}(\omega) f_e(t) f_h(t)$, it characterizes a different aspect of charge carrier dynamics and we will have discussions in Chapter 4.

2.3 Summary

In this chapter we have introduced the essential techniques we will be using to carry out the experiments throughout this dissertation. We introduced the pump-probe technique details and the relevant charge carrier dynamics in semiconductor materials. Since the TRPL and the streak camera is mainly about the instrument itself, we only

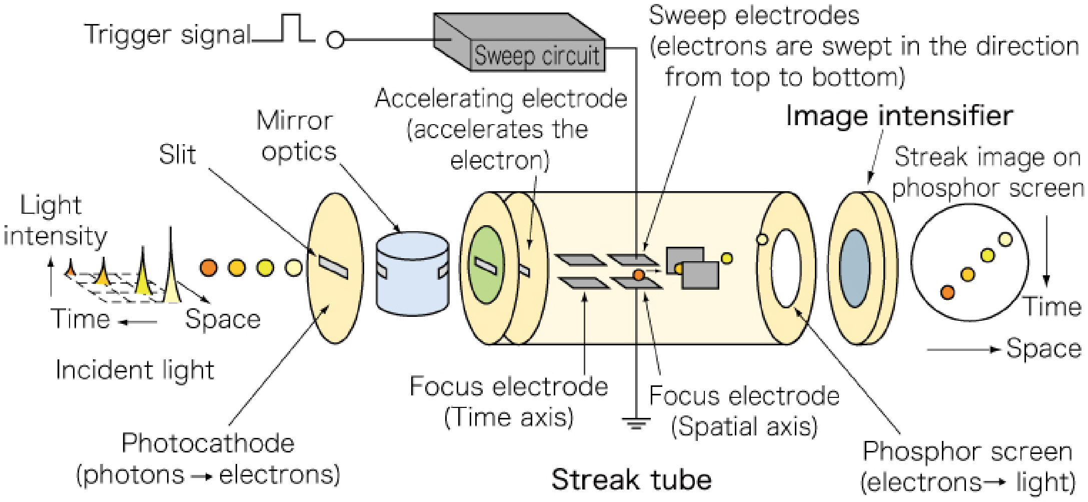

Figure 2.3: A schematic diagram of a streak camera taken from the Hamamatsu website.

briefly showed how it works. It is important to notice how the PL and pump-probe measure different physical quantities of the carrier dynamics.

BIBLIOGRAPHY

[1] A. Weiner, Ultrafast Optics. John Wiley & Sons, Sept. 2011.

[2] R. Trebino, Frequency-Resolved Optical Gating: The Measurement of Ultrashort Laser Pulses: The Measurement of Ultrashort Laser Pulses. Springer Science & Business Media, 2000.

[3] J. Shah, Ultrafast Spectroscopy of Semiconductors and Semiconductor Nanostructures, vol. 115 of Springer Series in Solid-State Sciences. Berlin, Heidelberg: Springer, 1999.

[4] R. P. Prasankumar and A. J. Taylor, Optical Techniques for Solid-State Materials Characterization. CRC Press, Apr. 2016.

[5] J. H. Scofield, “Frequency-domain description of a lock-in amplifier,” American Journal of Physics, vol. 62, pp. 129–133, Feb. 1994.

[6] R. Paschotta, “Noise of mode-locked lasers (Part II): Timing jitter and other fluctuations,” Appl Phys B, vol. 79, pp. 163–173, July 2004.

CHAPTER 3

Charge Separation and Relaxation in CVD MoS_2/graphene Heterostructures

In this chapter we will discuss the electronic dynamics in the chemical vapor deposition (CVD)-grown MoS_2-graphene heterostructures[1]. We will first review the physics of 2D electronic and photonic devices and the other related ultrafast experiments on 2D systems. Then we will briefly introduce the previous study of our group on the graphene photo-gating devices that demonstrated surprisingly high responsivity over a ultra-broadband spectrum [2] and how we utilize the transparency and the high responsivity to implement a 3-dimensional imaging system that either reconstructs the imaging lightfield or directly makes object position inference. Then we will go into details on the experimental methods, present the results and discuss our findings. In the last part of this chapter we will wrap up with our conclusions based on our findings.

3.1 Background

The recent two decades have seen a rapid growth of the studies about two-dimensional (2D) materials. The most commonly studied two-dimensional (2D) materials, graphene and transitional metal dichalcogenides (or TMDs), have stimulated wide interest partly by their properties distinct from their bulk counterparts, and partly by their potential for novel electronic and photonic applications[3]. Graphene, with its ideally zero bandgap and ultra-high carrier mobility[4], is a strong candidate for ultra-broadband photodetectors and high-speed electronic devices[5]. Monolayer MoS_2, one of the most commonly studied TMDs, has a direct bandgap of ~ 1.8 eV, in contrast to its bulk version which has an indirect bandgap of 1.23 eV. Several early works demonstrated high on-off ratio field effect transistors and photo-transistors based on MoS_2[6].

Many proposed devices based on 2D materials exploit heterojunctions between dissimilar 2D layers. Often the goal is to provide a means to separate the charges efficiently. For example, in previous work[2] our group has reported graphene-based ultra-broadband high responsivity photodetectors based on tunneling between two layers of CVD-grown graphene, enabling separation of hot photoinjected carriers and a conductivity change in the graphene transport layer. These structures have also been fabricated on transparent substrates to enable three-dimensional imaging applications[7, 8] Extensions of these device concepts to TMD-based structures are interesting for novel or improved device performance, e.g. in control of the spectral response or reducing the dark current. In general, the Van der Waals 2D material heterojunction systems are unique because they utilize both the 2D electronic systems and the interactions between the layers that can potentially be arbitrarily stacked to form interesting vertical electronic or photonic device structures. The performance of heterojunction devices is fundamentally determined by the dynamics of charge carriers, including hot electron dynamics, the transfer of charges between layers via tunneling or interlayer scattering, and the nature of the electronic states in the materials. Basic studies of dynamics are also often revealing of the nature of the electronic states in the materials. The study of the charge carrier separation and recombination dynamics is crucial to the development and engineering of heterojunction devices. There are a significant number of studies on charge and energy transfer in 2D TMD heterostructures, including the effect of monolayer defects in the efficient charge transfer from TMD monolayers to graphene in heterojunctions[9, 10, 11, 12]. Transient pump-probe methods are a common approach to studying this process; for example, Ref. [11] found near-unity efficient charge transfer from WS_2 monolayer to graphene in a heterojunction. Evidence of charge separation and formation of interlayer exciton in the MoS_2-$MoSe_2$ heterostructure was found in Ref. [13]. Ref. [9] also studied the extremely rapid charge transfer in the MoS_2-WS_2 heterostructures.

3.1.1 Graphene photodetectors

Our work is for the most part motivated by the previous work of our group on the CVD graphene based photodetector design mentioned above. It is difficult if not possible to have a clear vision of this work without mentioning the previous results. The graphene photodetector developed in Liu, et al's work, the so called photogating device, consists of two layers of CVD grown graphene that are separated with a layer of tunneling barrier[2]. Since graphene is but a single layer of carbon atoms, its electronic state is susceptible to molecules attached to them, so its doping level can vary between the different samples and between different fabrication processes. There has also been a number of studies that proposed to utilize this property of graphene to make sensitive chemical sensors[14, 15]. The operation mode of this photodetector is best described as a photo-conducting phototransistor device. A bias voltage can be applied to between the two layers of graphene to tune the silicon barrier shape and height. The bottom graphene layer is connected with the source and drain electrodes that are constantly biased. The device schematics and the band diagram is shown in Figure 3.1. Because the two layers of graphene are in contact with different environments, they have different doping levels. Specifically for this structure, the top layer that is in contact with the air is slightly more heavily p-doped. So when no

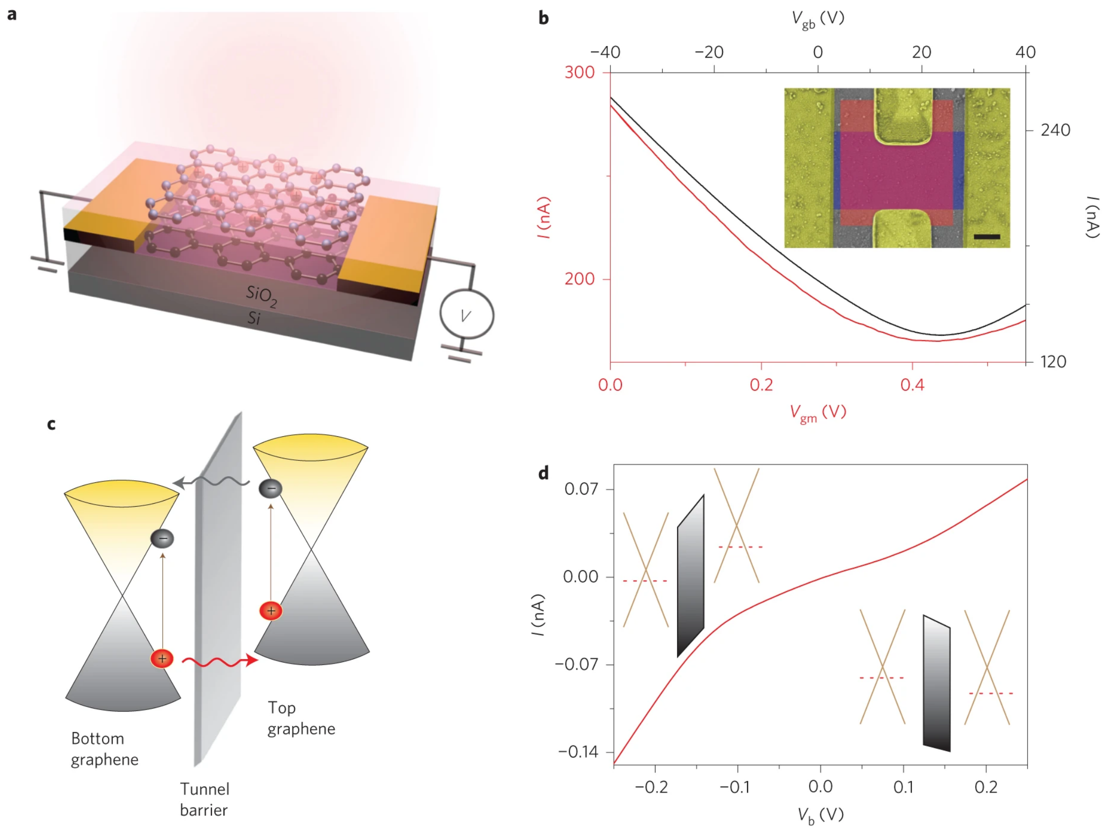

Figure 3.1: The photo-gating broadband high responsivity graphene photodetector[2].

bias is applied between the two layers there is a built-in static field across the barrier.

It is well-know that one limiting factor for the pure graphene photodetectors is the short charge recombination lifetime. In other words the electron hole pairs generated by photon excitation recombine in as short as a few picoseconds, so the portion of the carriers that are able to reach the contacts and create an electronic signal is limited by the short lifetime. With the photo-gating device structure, after the light hits on the graphene layers, electron and hole pairs are created in both of the graphene layers and tunnel asymmetrically across the layers, and the two kinds of charge carrier will tunnel into separate layers due to the built-in asymmetric bias, therefore the recombination lifetime is prolonged, leading to an enhanced photoresponsivity. Because the graphene ideally has zero bandgap, the photodetectors made from the graphene is, technically speaking, sensitive to a broad spectrum of wavelengths from visible to near- and mid-IR, only limited by the fabrication defects and the barrier properties.

The pure graphene detectors are not without drawbacks. Since the graphene ideally has zero bandgap, it suffers from a non-negligible dark current. Under room temperature it is a major source of noise in the photodetection. Replacing one of the two layers with some material with a finite bandgap is the most straightforward way of improvement. MoS_2 being the most common and well studied 2D material, is our first candidate for this purpose. The simplest form of the heterostructure consists only a single layer of graphene and a layer of MoS_2, with no separating layer in between. It is not exactly the same as the photo-gating device structure but the dynamics study will be informative to the further studies. The questions we would like to answer are whether there is charge transfer, and its limiting factors in the dynamics.

There has been a lot of other groups that studied the charge and energy transfer dynamics in 2D heterostructures. As it turns out, our work here, instead of the initial charge transfer over process, focuses more on the transfer back process and its indications on the electronic structure of the underlying material systems. Also, in the studies conducted in this work, we only photoexcited the graphene layer, and we observed evidence of charge transfer from the graphene to the MoS_2 after the excitation. Up to when this work was written we are not aware of other groups reporting similar results.

3.1.2 Fabrication of 2D materials

Natural monolayer materials do not exist in their 2D form; they are always fabricated in the laboratories. The fabrication methods of 2D materials are roughly divided into two categories: bottom-up, by chemically or physically deposit the material from molecules in a controlled way to form uniform monolayer films; and top-down, by chemically or physically split the layers from the bulk material to form monolayer films. The earliest 2D materials were made with the so-called mechanical exfoliation method, which is the most well known example of top-down method. To do so, one uses a piece of Scotch tape to repeatedly attach to both sides of a thin flake of the bulk material, be it graphite for graphene or bulk MoS_2 ore flake for making monolayer MoS_2, and split to cleave off thinner and thinner piece of the flake. The cleaved off thin flakes are then deposited onto a piece of substrate, usually silicon wafer with oxides. The resulting material is the flakes of various shapes, sizes and thicknesses on the substrate. It involves intense labor in hunting for the monolayer material on the substrate, usually only distinguishable by their coloration, that has sufficient size for the research. Even though this method looks extremely unreliable and labor intense, since the monolayer flakes come from the natural crystaline ore, they in general have very high crystal quality. Other fabrication methods include chemical exfoliation, epitaxial growth, and chemical vapor deposition (CVD).

While a majority of the previous studies on 2D materials and their heterostructures were conducted with mechanically exfoliated 2D materials, researchers have also made progress on more reliable and scalable ways of producing 2D materials. As this work was most motivated for possibilities of photo-detection in production, it makes more sense to use the CVD method for fabrication, which is compatible with mass-production applications. The MoS_2 monolayer is grown directly on top of Si/SiO_2 wafer with MoO_3 powder reacting with sulfur vapor under Ar atmosphere. Admittedly it was widely believed that the exfoliated 2D materials are less defective than the CVD grown ones and they tend to create cleaner interfaces in heterostructures, for the application purposes it is still valuable to study the CVD grown systems and understand the effect of the defects. We will address the interface disorder issue in the result discussion.

3.2 Experiments

3.2.1 Sample preparation

The MoS_2 film was grown using chemical vapor deposition (CVD) on Si/SiO_2 wafer by using MoO_3 and sulphur vapor reacting in Ar atmosphere. The process starts with 18mg of MoO_3 crucible placed at the center of the reaction zone with 0.5g of sulphur at the edge of the reaction zone. A piece of Si/SiO_2 wafer with an SiO_2 thickness of 500 nm was cleaned and sequentially rinsed with acetone, isopropyl alchohol and deionized water sequentially and dried in N_2, and then placed directly on top of MoO_3 facing down (i.e. the SiO_2 surface touches the MoO_3 powder). Then the growth tube was dehydrated at 115°C for 20∼30 minutes under a vacuum of 1.1 Torr. After filling the tube with Ar gas up to atmosphere pressure, the furnace temperature was ramped up to 700°C at a rate of 15°C/min and held at 700°C for 10 minutes before naturally cooling down to room temperature. Ar flow was kept at 700sccm during the process. After the process, a crescent-like shape of deposited MoS_2 was formed on the wafer, with a maximum width of $\sim$ 5mm. SEM imaging was performed just after the CVD process. The graphene film is commercial CVD graphene grown on copper foil. It was transferred on top of the MoS_2 sample with the wet-transfer technique as described in the literature [16]. The graphene film is square in shape and it was positioned relative to the MoS_2 area such that its edge crosses the crescent shaped MoS_2 region near where the growth was monolayer and relatively uniform. We annealed the sample in Ar gas at $300°C$ for 15 minutes to enhance graphene's interface quality with MoS_2. The SEM image in the main text showed that the MoS_2 monolayer has a high coverage of around 90% such that almost all the MoS_2 flakes are connected and unchanged after the transfer. All the optical experiments and characterization are performed with the light beam focused near the crossing of the

MoS_2 and graphene edges to avoid possible differences between experiments due to non-uniformities of the sample. Raman spectroscopy was performed (Horiba XploRA INV with 532 nm excitation) just after growth and after the transfer process. The PL characterization was measured with 400 nm CW excitation at a power of 5 mW and a spotsize of $\sim 5\mu$m, and detected with a Hamamatsu photomultiplier tube (PMT) after spectrally filtering with Horiba iHR550 monochromator with 1200 groove/mm gratings.

After the CVD growth, we transferred a layer of CVD graphene film onto the CVD MoS_2 with the wet transfer technique to form a vertical heterojunction. To perform the wet transfer, a layer of PMMA was first spin-coated onto the commercial CVD graphene film grown on copper substrate to protect the graphene, and then the copper was etched out leaving a thin film of graphene attached to PMMA. We then let the graphene and PMMA film float on top of water in a container with graphene side facing down and the target surface, which is the CVD MoS_2 on Si/SiO_2 wafer, sitting at the bottom of the water with MoS_2 side facing up. After slowly draining all the water, the floating film of graphene and PMMA touches the MoS_2 surface, and we can remove the PMMA with solvents and anneal the whole chip in argon atmosphere at $300°C$ for 15 min to remove trapped molecules between the two layers and enhance surface qualities. Previous studies have shown that the materials prepared with the wet transfer techniques can benefit in the interface quality by annealing. The two pieces of monolayer 2D materials are intentionally mispositioned as shown in so that in general vicinity of the sample crossing it is possible to find all the heterostructure and the two kinds of monolayer regions that are overall uniform.

3.2.2 Intrinsic Characterization of 2D materials

We characterized the just grown MoS_2 with scanning electron microscopy (SEM) imaging to evaluate the growth quality. Fig. 3.2(a) is the SEM image following the

CVD process showing uniform deposition and a coverage of approximately 90%. A photoluminescence (PL) measurement with 400 nm continuous wave (CW) excitation was performed on the CVD-grown MoS_2 sample at room temperature, which showed an exciton emission peak near 660 nm (Fig. 3.2(d)). The graphene layer was transferred on top of the MoS_2 film by the wet transfer technique after etching off the copper foil[16]. The whole chip was then annealed to purge possible trapped molecular impurities between layers. SEM imaging characterization of the MoS_2 sample was performed again after the transfer to evaluate possible transfer damage (Fig. 3.2(b)). Raman spectroscopy was conducted on the heterostructure and showed characteristic peaks for both MoS_2 and graphene (Fig. 3.2(c)), implying that both layers have mostly maintained their as-grown crystalline quality[17, 18]. The PL of the heterostructure shows that the MoS_2 emission is largely quenched due to the coupling with the graphene layer (as expected).

3.2.3 DR Experiment Setup

Since the substrate of the heterostructure sample, SiO_2 on Si, is opaque near the exciton resonance of MoS_2 in the visible range rendering transmission experiments impossible, the differential reflectance pump-probe technique was used to measure the ultrafast electronic dynamics in the MoS_2 monolayer. Fig. 3.3 is a schematic illustration of the optical experiment setup.

This is a typical nondegenerate pump-probe experiment setup. We first characterized the material with above the bandgap excitation that can generate electron hole pairs in both the MoS_2 and graphene layers. A 250-kHz Ti:sapphire RegA system (Coherent RegA 9000) produced 50-fs pulses at 800 nm with a few microjoules of energy. Approximately 1 μJ of the energy was focused into a sapphire wafer to generate a white light supercontinuum to serve as the probe; the remainder was used to generate pump pulses at 400 nm (3.1 eV) via second harmonic generation in a

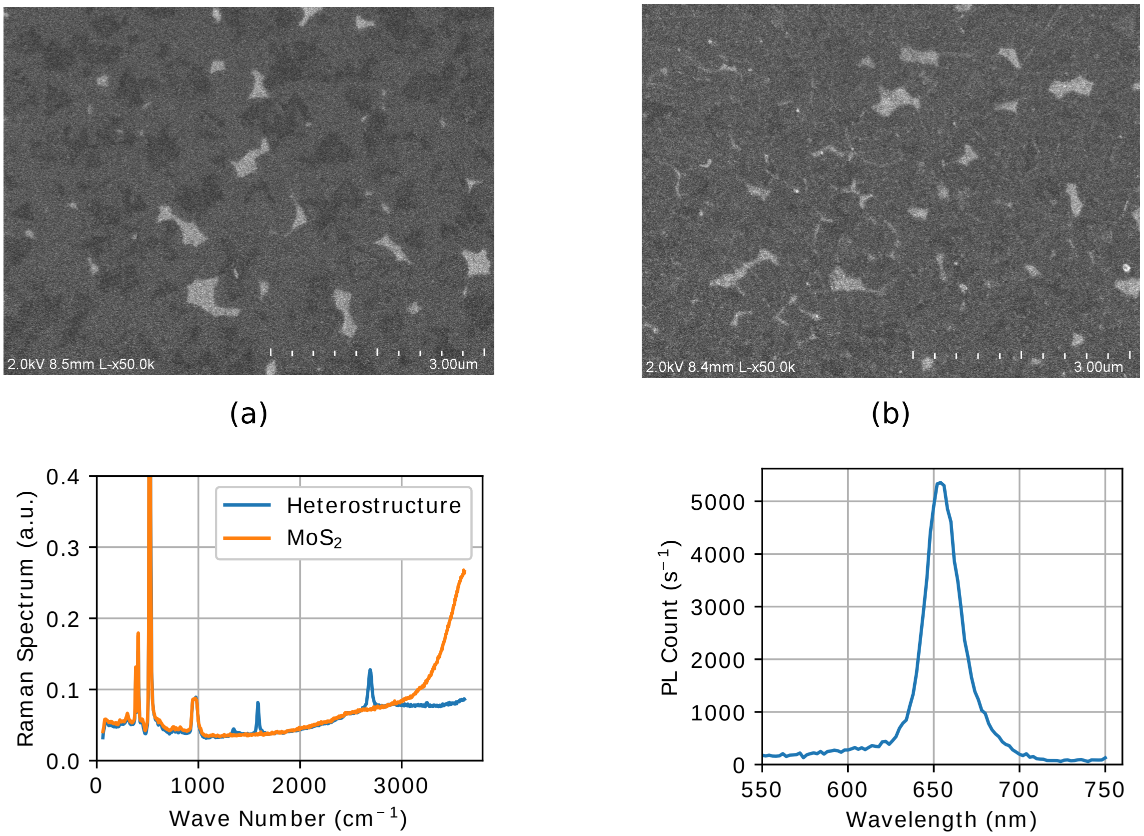

(a)

(b)

(c)

(d)

Figure 3.2: The Raman and SEM characterization of the CVD grown MoS$_2$ and the stacked graphene-MoS$_2$ heterostructure. Fig (a) and Fig (b) are the scanning electron microscopy (SEM) image of the CVD grown MoS$_2$ and also the SEM image of the fabricated heterostructure. The light gray area is where there is little to no MoS$_2$ deposition, and the darker gray area indicate the thickness of the grown MoS$_2$ layer. We can tell from the SEM image that the MoS$_2$ grown has a coverage of approximately 90% and it stayed mostly the same after the wet transfer of graphene layer. Fig (c) is the Raman spectrum of the CVD grown MoS$_2$ and the stacked heterostructure, respectively. In the Raman spectrum for CVD MoS$_2$, the two main peaks are shown clearly, with the in-plane mode (E_{2g}) at 383 cm^{-1} and out-of-plane mode (A_{1g}) at 406.5 ± 1cm^{-1}. The second peak center has an uncertainty of $\sim$ 2cm^{-1} due to the instrument resolution. Fig. (d) shows the photoluminescence (PL) characterization of the CVD grown MoS$_2$ used to fabricate the heterostructure sample. It has bright exciton peak at $\sim 660nm$.

1-mm Barium Borate (BBO) crystal. A short-pass spectral filter is inserted on the probe path to block the spectral components longer than 700 nm in wavelengths for the purpose of reducing the risk of damaging the sample, reducing the thermal effect and increasing the signal-to-noise level. The pump photon energy is significantly larger than the MoS_2 bandgap, thus creating a density of carriers in the MoS_2 layer that gives rise to a large DR signal around the MoS_2 exciton transition energy. The pump and probe beams are collinearly incident on the sample at near normal incidence, with pump and probe spot diameters of approximately 10μm and 5μm, respectively. The reflected continuum probe beam is focused onto the entrance slit of a monochromator providing 2.5-nm spectral resolution and detected with a silicon photodiode. The detector signal is measured by a lock-in amplifier referenced to an optical chopper modulating the pump beam at 1 kHz in order to directly detect the differential reflectance. The same experiment was also repeated on the heterostructure. Theoretically after the time zero was found, one can measure the spectral DR response by scan the wavelength of the monochromator with the delay between pump and probe fixed slightly positive from the time zero. Practically the supercontinuum generation can have a positive chirp, thus resulting in a different timing for different wavelength components, so the same scans of wavelength is repeated with multiple pump and probe delays after zero to cover the range of different probe wavelength components effectively forming a grid scan of probe photon energy and the delay time. To process the DR spectral response, we find the maximum of the absolute value of the DR response for each of the wavelengths and combine them to form the differential reflectance response.

To study the possible charge transfer between the graphene and the MoS_2 monolayer, we then removed the BBO crystal and used the 800 nm pulses directly output from the RegA, which has a photon energy of 1.55 eV, and is not able to create photocarriers in the MoS_2 layer. The spectral-resolved DR of the heterostructure is

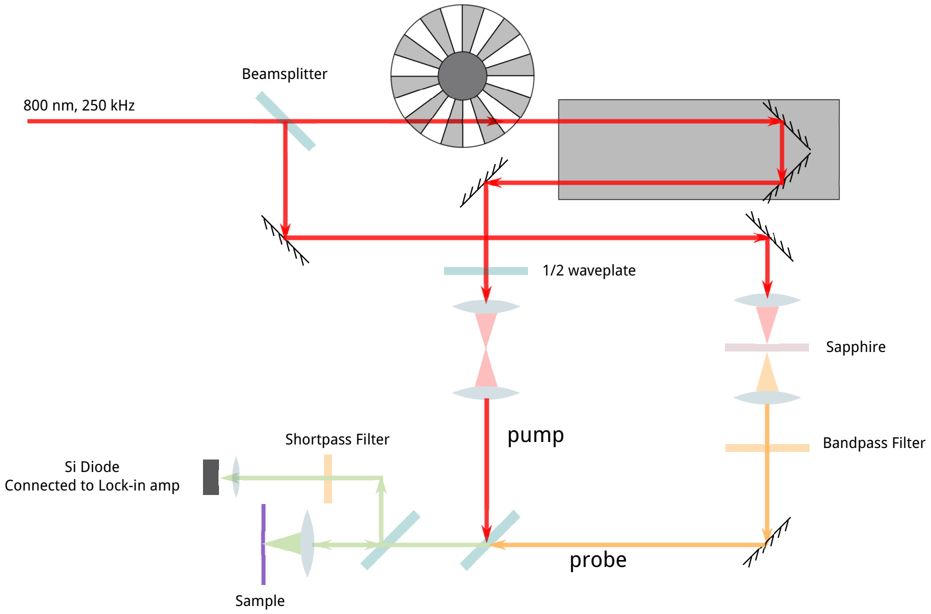

Figure 3.3: A schematic illustration of the optical setup for the ultrafast differential reflectance pump-probe experiment. In this work, a Ti:sapphire regenerative amplifier (RegA) seeded with an oscillator was used. The amplifier outputs femtosecond pulses with a wavelength of 800 nm and a repetition rate of 250 kHz that have a 4μJ pulse energy.

measured using the same procedure as the 400 nm pump experiments. Then we measured the time-resolved DR of the heterostructure to characterize the charge transfer dynamics by scanning the pump-probe delay while keeping the probe photon energy fixed near the peak DR response. The monochromator is replaced with a piece of bandpass filter with a central wavelength of 660 nm and a bandwidth of 10 nm for increased signal-to-noise ratio. We also carried out control experiments on the graphene and MoS_2 only regions to rule out the effect of one individual layer.

3.3 Experiment Results and discussions

3.3.1 Above gap excitation results

The spectral resolved DR from the MoS_2 and the heterostructure are shown in Fig. 3.4, where the pump pulse fluence is $\sim 200\mu\mathrm{J/cm}^2$ for both the heterostructure and the

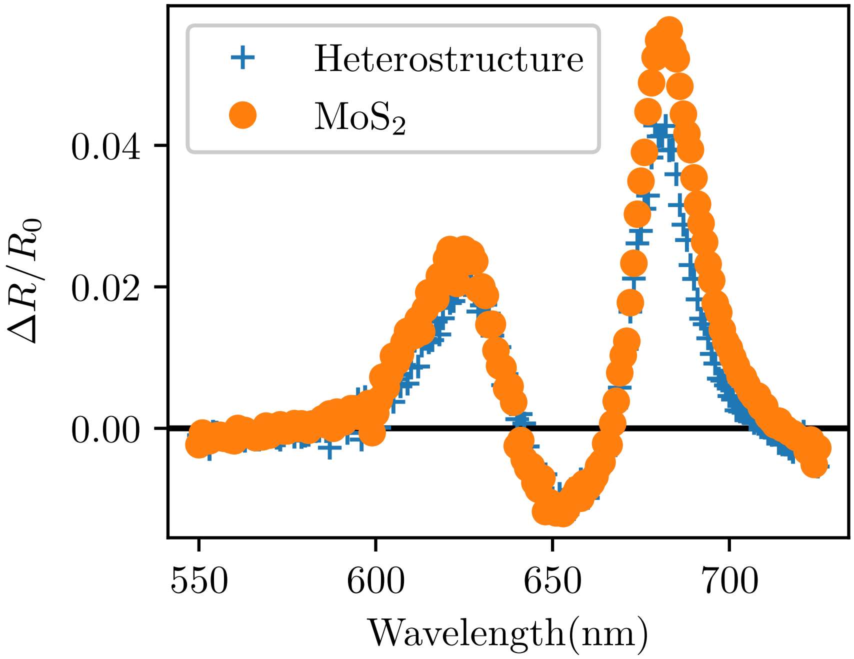

Figure 3.4: The spectral resolved differential reflectance pump probe signal of the MoS_2/graphene heterostructure and the control MoS_2 monolayer.

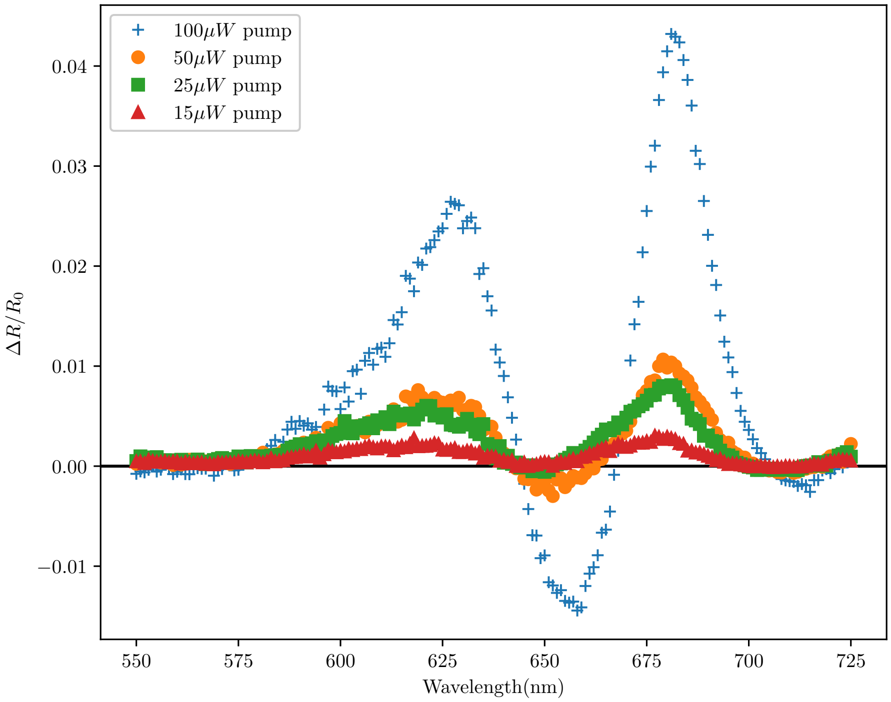

Figure 3.5: The pump power dependent DR spectrum of the MoS_2/graphene heterostructure.

control MoS_2 monolayer.The A- and B-exciton peaks are shown in the MoS_2 monolayer experiments at approximately 680 nm and 620 nm, matching well with the literature[19, 20, 21, 21, 10, 22]. The DR signal is positive, also consistent with prior reports[22]; at high pump power a small negative contribution is present indicating the DR signal has line-shift and broadening as well as the dominant contribution from bleaching. While the differential reflectivity in principle is affected by pump-induced changes to both real and imaginary parts of the optical conductivity, it has been shown in Ref. [22] that, when the carrier density is not too high, the DR signal is mainly determined by changes in the exciton absorption, which is proportional to the density of carriers. While the physical effects contributing to nonlinear DR spectra in III-V semiconductor quantum wells have been long-established [23] the detailed microscopic many-body theory of the DR spectrum of MoS_2 monolayers does not yet exist; recent many-body theories of the nonlinear absorption or transmission spectra, however, provide strong evidence that at the carrier densities relevant to our experiments (below $10^{12}\mathrm{cm}^{-2}$), the main contributions are phase space filling and bandgap renormalization[24, 25]; the key relevant point for this work is that, by measuring the dynamics of the DR amplitudes, we essentially measure the dynamics of the population in the MoS_2 layer. We finally note that thermal modulation, i.e. modulation of the MoS_2 exciton transition due to a change in temperature of the lattice, is ruled out as a mechanism contributing to the DR by the pump-probe measurements with 400-nm pump on the MoS_2 alone (); no long tail of the DR dynamics is observed that would be associated with cooling via interaction with the substrate (i.e. only a rapid recombination recovery is observed in bare MoS_2).

The DR spectrum of the MoS_2/graphene heterojunction under 400-nm pump is found to be essentially the same as that for the control bare MoS_2 layer (spectrum shown in supplemental materials); the presence of the graphene layer does not appreciably modify the MoS_2 DR spectrum when the pump injects electron-hole pairs into both layers.

3.3.2 Below gap excitation results

We now consider the DR spectrum when the pump wavelength is 800 nm (1.55 eV) which is below the bandgap of MoS_2. The spectral resolved DR response from the heterostructure is mostly positive in the range of our experiments while showing a broad feature. There are two peaks in the DR spectrum, each being blue-shifted from the A and B exciton lines of the standalone MoS_2 monolayer. The DR dynamics are shown in Fig. 3.6(b) and 3.6(c). The DR signal shows a rapid rise on the order of $\sim$ 100-fs temporal resolution of the experiment, and the decay on multiple time scales from a few to a hundred picoseconds. The DR amplitude is found to be linear with the pump power, as expected.

For the MoS_2 control sample, we only made time-resolved measurements under the same conditions of the DR dynamics of the heterostructure. We find negligible DR response at the A and B exciton lines, indicating that multiphoton generation of electron-hole pairs directly into the MoS_2 is negligible in this experiment at the pump intensities used. On the bare-graphene control sample, we find a very small DR response from the graphene layer for probe wavelengths in the 620 to 680 nm range ().

3.3.3 Mechanism of DR Signals

We then discuss the mechanisms for the DR response that was observed. Previous works on the DR experiments of the MoS_2 monolayers have shown linear dependence of DR signal and the charge carrier density [22] when the charge density is low. In our experiments for both the 400 nm and 800 nm pump measurements at a repetition rate of 250 kHz the pump pulses fluences are at a $\sim 400\mu\text{J/cm}^2$ level, and the relative DR signals $\Delta R/R_0$ are less than 3%, which still fall in the linear response range. In

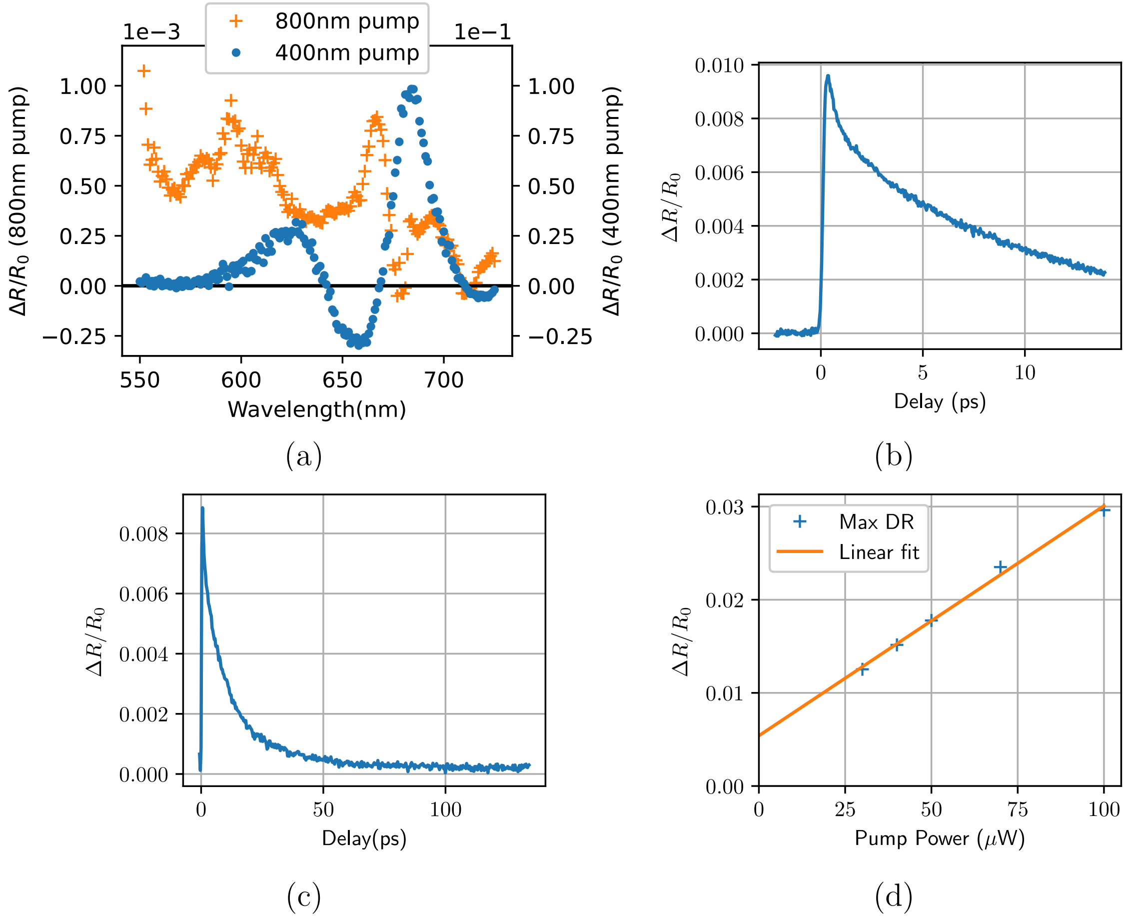

(a)

(b)

(c)

(d)

Figure 3.6: The time-resolved DR experiment results are shown. (a) is the spectrally resolved DR signal measured from the heterostructure region, conducted with 400 nm (above gap energy) and 800 nm (below gap energy) pump pulses, respectively. Both set of DR spectrum are taken with pulses at $4 \times 10^2 \mu J/cm^2$ fluence, and probed with supercontinuum filtered by a monochromator. (b) and (c) are the delay time resolved DR signals on the graphene-MoS$_2$ heterostructure region of the sample with 800 nm pump at $2 \times 10^2 \mu J/cm^2$ fluence, and probed with white light filtered by a 10 nm bandpass filter centered at 660 nm, and they only differ in the time delay range of the scan. (d) is the power dependence of the DR signal on the graphene-MoS$_2$ heterostructure region pumped with 800 nm pulse. The line depicts a linear fit of the power dependence data.

the following discussions we can interchangeably use the DT signal and the excited charge occupation in further discussions.

Because CVD-grown graphene is environmentally lightly p-doped in the air[2], and likewise as-grown MoS_2 is typically n-doped[26], then upon formation of the heterostructure, there will be a static charge transfer to align the layer Fermi levels, and the expected heterostructure band alignment would roughly appear as in Fig. 3.7, which is a schematic demonstration of the pump-probe experiment setup. In our experiments, the pump pulse, having photon energy 1.55 eV, will excite electron-hole pairs only in the graphene layer. Multiphoton absorption in the MoS_2 layer is also in principle possible, but it is found experimentally to be so weak as to be negligible (discussed below in control experiment results). Due to the band alignment of the heterostructure, electrons rapidly transfer from the graphene to the MoS_2. The transfer of electrons competes with thermalization within the graphene layer, so the transfer process illustrated in Fig. 3.7 is an idealization; in reality, electrons from a thermalizing distribution in the graphene scatter into a broad range of energy states in the MoS_2 conduction band.

Following the initial transfer, the electrons will thermalize and cool within the MoS_2 layer on a few picosecond timescale[27, 28, 29], while an excess hole population remains in the graphene layer, which has thermalized and cooled to the lattice temperature. The cooling time in the isolated graphene layers has been established to be within 2–3 ps[29][30]. For the system to return equilibrium, the electrons in the MoS_2 must scatter back into the graphene layer. This process is expected to be much slower than the forward transfer process, since now the final state for scattering from the MoS_2 will be in the graphene near the Dirac point where the density of states is low.

With our control experiment results, we can conclude that the probe response in the heterostructure will be dominated by the carrier population in the MoS_2 layer,

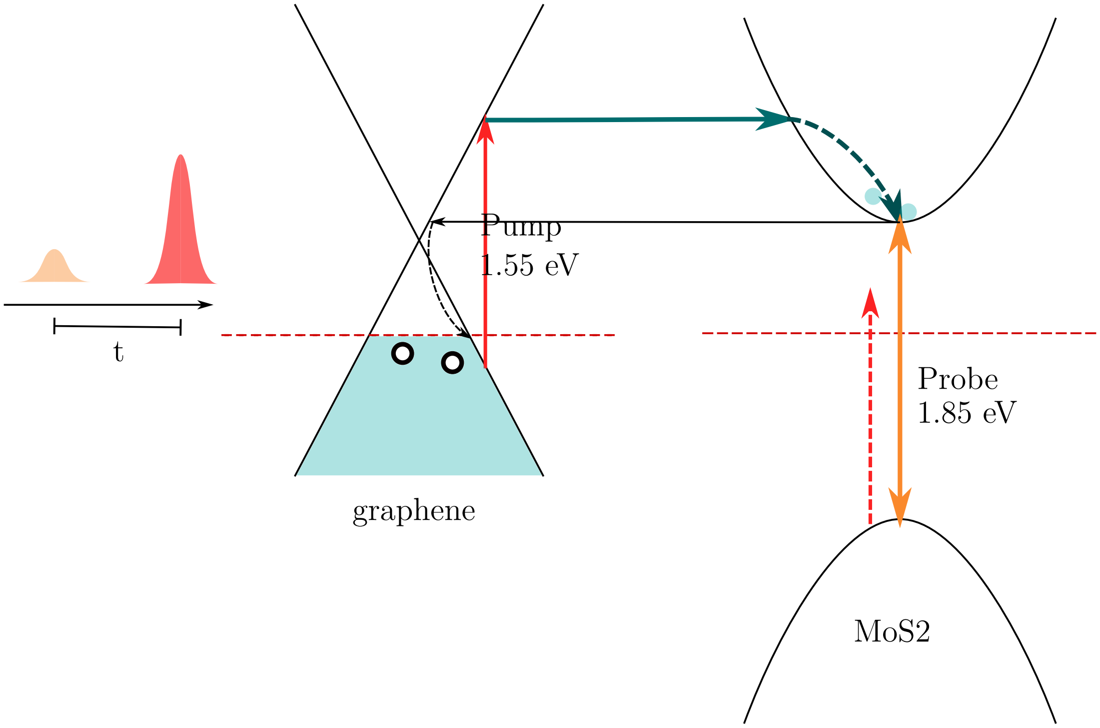

Figure 3.7: A schematic illustration of the band diagram and the pump-probe DR experiment. The two pulses (pump at 800 nm and probe at 660 nm) separated by a controlled delay hit the sample, with the pump pulse inducing e-h pairs only in the graphene layer. The dashed red arrow near the MoS_2 layer illustrates the photon hitting also on the MoS_2 layer, but it generates very few carriers because its photon energy is below the bandgap of monolayer MoS_2. The hot carriers are coupled to the MoS_2 layer and transfer over immediately before cooling down and transferring back.

and the dynamics of the DR will provide a measure of the population dynamics in the MoS_2 layer. The pump injects electron-hole pairs directly into the graphene only; hot electrons transfer rapidly to the MoS_2 layer where they relax to the band edge. The system eventually returns to equilibrium as these electrons scatter back to the graphene, and recombine with the holes that have remained in the graphene layer.

We then revisit the DR spectrum; following the electron transfer, the DR of the MoS_2 A and B excitons will be modulated by the population of electrons. The DR spectrum of the heterostructure shows a blue shift of the A and B excitons relative to the situation with 400-nm pumping, mainly because the 400-nm pump injects both e and h into the MoS_2. The precise origins of this shift remain to be calculated via microscopic many-body theory, as we see that the exciton lines are modulated quite differently by neutral e-h pairs and by an electron population alone.

3.3.4 Modeling of dynamics

From the dynamics measured from the DR experiments, the decay curve of the DR signal is obviously not single or bi-exponential; it consists of components of multiple different timescales. In this case, a physical model is desired to interpret the results as obviously an inverse problem is numerically impossible.

3.3.5 Rate equation interpretation

When there are multiple processes in the carrier dynamics, one of the most common approaches is to model it with a two temperature rate equation model. Recall that in the last chapter we discussed a normal carrier dynamics of excitation, thermalization and relaxation, where the photo-carriers are first excited to a higher energy state (because of the off-resonance excitation), and reach a high temperature quasi-equilibrium (hot carriers) before they release the energy to the lattice by phonon interactions, becoming thermally equilibrium with the lattice (cool carriers), and then recombine or

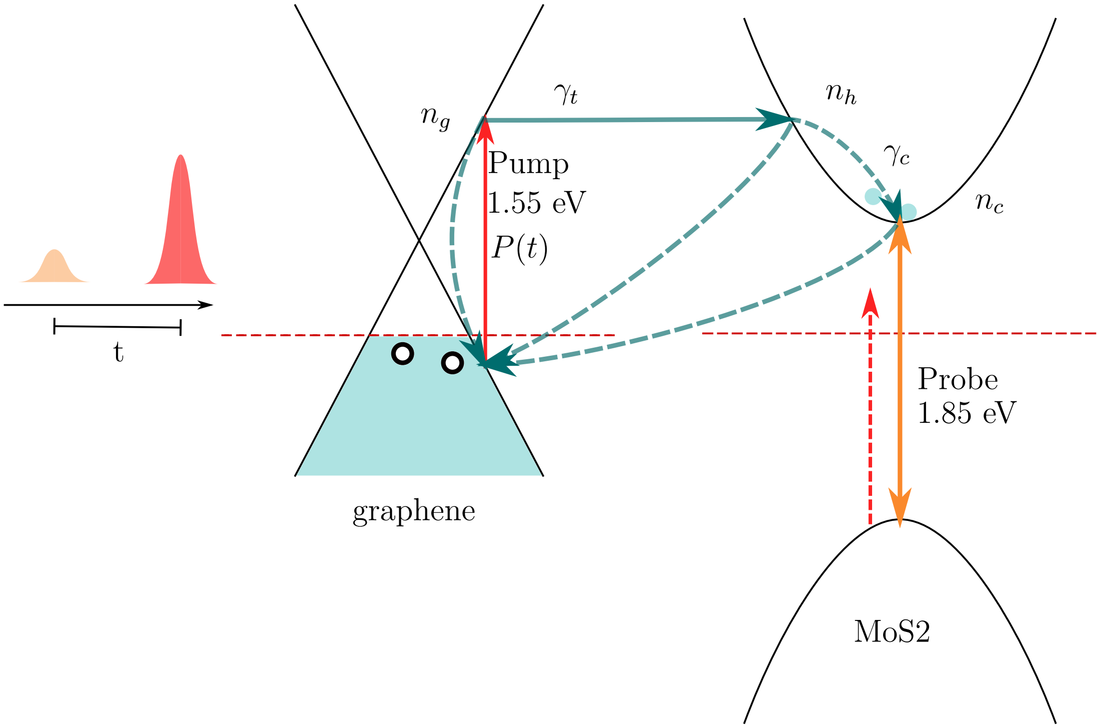

Figure 3.8: A schematic diagram for the rate equation model of the charge transfer in MoS_2/graphene heterostructure.

return to ground state. We model the DR signal by assuming that it consists of the contributions both from the cool and hot carriers, each being proportional to their densities, or, if we also simplify the model by ignoring any transport, carrier populations. A more sophisticated model will have to consider the scattering process, the exciton states and the detailed dielectric functions, but for now we used a simplified linear model which assumes that the occupations are small and that the transition between the hot and cool electrons are linked with a rate equation. The outcome of the model should be similar.

We assume that the carriers can have three excited states in the heterostructure system, in the graphene layer (n_g), hot carrier in the MoS_2 layer, and cool carrier in the MoS_2 layer. Upon the excitation of the pump pulse, carriers are only generated in the graphene, population denoted by n_g, with the injection rate $P(t)$ that is proportional to the input pulse shape. The carrier in the graphene layer transfers into the hot

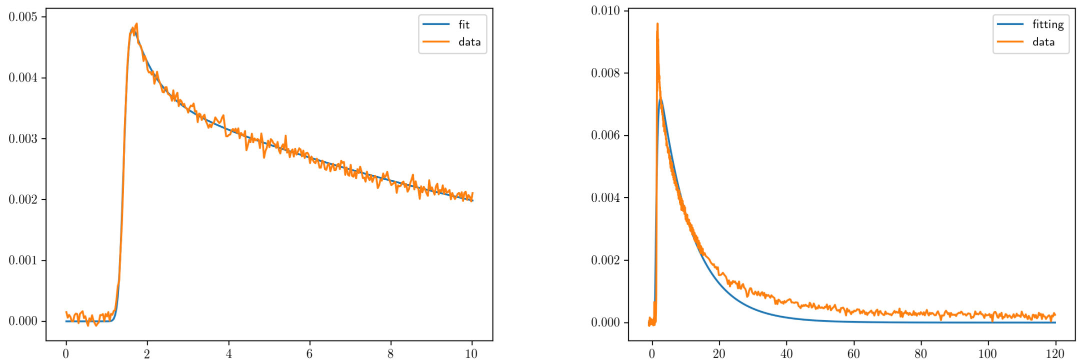

(a) (b)

Figure 3.9: The two temperature rate equation model fitted to the experimental TRDR measurement. Experimental data in both (a) and (b) use the same 800 nm pump and 660 nm probe (spectral filtered supercontinuum). (a) covers a delay range of 20 ps depicting the early charge carrier dynamics upon excitation, while (b) covers a longer 120 ps delay range. The rate equation model fits the early dynamics well but fails to fit the tail of the dynamics in the long delay range data.

state in the $\mathrm{MoS_2}$ layer (n_h) and cools down to become the cool carriers (n_g). All the carrier populations, n_g, n_h and n_h, have a channel of getting back to the ground state with some recombination rate.

$$
\begin{aligned}
\frac{\mathrm{d}n_{gr}}{\mathrm{d}t} &= P(t) - \gamma_{gh} n_g - \Gamma_{gr} n_g \\
\frac{\mathrm{d}n_h}{\mathrm{d}t} &= \gamma_{gh} n_g - \Gamma_h n_h - \gamma_{hc} n_h \\
\frac{\mathrm{d}n_c}{\mathrm{d}t} &= \gamma_{hc} h_h - \Gamma_c n_c
\end{aligned}
\tag{3.1}
$$

The rate equation model is simulated with the lsoda general ODE solver and the resulting population relaxation curve is fitted with the experimental DR data by assuming that $\Delta R = a_h n_h + a_c n_c$ and optimizing the mean square loss between the simulation and the measured data. Noticing that here we are dealing with seven fitting parameters on the relaxation curve, it makes the fitting process unstable. In practice, we assumed a fixed recombination rate for the carriers in the graphene based on the estimated carrier lifetime in the published literature. We further manually fixed a ratio of $a_h : a_c$ because the simulation result is not very critical to this number by numerical experiments. The a_h to a_c ratio is then manually scanned for an array of values to produce a series of simulated models fitted with the data. The best result (with the least mean square loss) is picked, and the ratio is set to be $a_h : a_c = 10\% : 90\%$ in this result. Fig. 3.9 shows the resulting rate equation model plotted along with the experiment data. The fitting parameters for the different transition rates are found to be $\gamma_g h = 16\text{ps}^{-1}$ (transfer rate), $\gamma_h c = 3.6^{-4}\text{ps}^{-1}$ (cooling rate), $\Gamma_h = 9.7^{-2}\text{ps}^{-1}$ (hot carrier recombination rate), and $\Gamma_c = 4.4\text{ps}^{-1}$ (cool carrier recombination rate). As it turns out, the best fitting the rate equation model can achieve requires a nonphysical model, and it cannot fit well with the long tail of the measured DR signal.

3.3.6 Stochastic model

As the simple rate equation method fails to approach the experimental results, it was found that the DR dynamics closely follow the ubiquitously observed Kohlrausch's Law, i.e. the stretched exponential function $f(t) = e^{-(t/t_0)^\beta}$, with the exception at the tail if we prolong the experimental measurement window of pump-probe delay to over 100 ps, where the stretched exponential function fitted with least squares loss drops faster than the experimental data. This result gives us hint that the dynamics we observed can be more complicated than a clean physical system but rather might involve random processes. However, as just a phenomenological formula, there is not much physics insight in the Kohlrausch's Law.

In general the stretched exponential results from a random distribution of the decay rate or time constant; the randomness of the decay rate can be either due to a cascade relaxation process, where the carriers go through a series of random steps before recombination, or due to an ensemble of parallel channels that have varied transfer rates.

It is usually easier to model the charge transfer probability thus the transfer rate γ is it is directly related to the electronic states and the interaction Hamiltonian. However, experimentally only the differential relative transmittance or reflectance $\Delta T(\tau)/T_0$ or $\Delta R(\tau)/R_0$ is measured, where τ is the relative delay between the pump and probe pulses. In this project, we are using differential reflectance to characterize the charge transfer dynamics, and $\Delta R(\tau)$ is proportional to the remaining charge occupation $\Delta n(\tau)$, which is actually the initial charge transferred over minus the accumulated charge transferred back. If we denote the charge transfer rate as $T(t)$, then the DR signal should be proportional to 1 minus the normalized transferred back charge.

$$S(t) = \Delta R(t) \propto S(0)\big(1 - \frac{1}{\int_0^\infty T(\tau)\mathrm{d}\tau} \int_0^t T(\tau)\mathrm{d}\tau\big) \tag{3.2}$$

In the following parts we will use Eq. 3.2 for converting the transfer rate models to the DR dynamics for fitting with experimental data.

While the microscopic features of the disorder in the system studied here is still open for further study, the statistical properties may be comparable to the disorder in the molecular beam epitaxy (MBE) grown III-V compound quantum well systems which has been studied extensively in theory and experiments in the last decades. Specifically, it was found in the studies of radiative porperties of III–V quantum wells that the distribution of oscillator strength for exciton transitions follow the Porter-Thomas distribution (PTD)[31], i.e. the χ^2 distribution with only one degree of freedom.

If we take a step back and look at Zimmermann, et al's study on the oscillator strengths in the III-V quantum well systems we will see how the randomness leads to the PTD[32, 31]. It is widely known that the low temperature III-V quantum well systems have disorders and the disorders lead to localized electronic states. Zimmermann asserts that in such a random system, the optical matrix element, follows PTD simply because the random potential and the wavefunction values all follow the Gaussian distribution. In the quantum well system the wavefunction of exciton center of mass ψ motion follows the Schrødinger equation

$$\left[-\frac{\hbar^2\nabla^2}{2m_X}+V(\mathbf{R})\right]\psi=E\psi(\mathbf{R}) \tag{3.3}$$

where $V(\mathbf{R})$ denotes a random potential field. The luminescence line of photon energy E corresponds to a transition from a state $|\beta\rangle$ at an energy level E above the line center to the bottom state $|\mathbf{k}=0\rangle$. And with a random potential V in Hamiltonian the perturbed state $|\beta\rangle$ should be given by

$$|\beta\rangle=\sum_{|\mathbf{k}|\approx k_E} u_{\mathbf{k}}^{\beta}|\mathbf{k}\rangle, \tag{3.4}$$

where the coefficients $u_{\mathbf{k}}^{\beta}$ diagonalize the potential V as the degenerate first perturbation. The wavefunction value $u_{\mathbf{k}}^{\beta}$ is Gaussian distributed. Therefore, the optical matrix element, which as stated above corresponds to the transition to the low energy state in the first order perturbation theory should be written as

$$M_E=\frac{\langle\mathbf{k}=0|V|\beta\rangle}{E}=\sum_{|\mathbf{k}|\approx k_E}\frac{u_{\mathbf{k}}^{\beta}\langle\mathbf{k}=0|V|\mathbf{k}\rangle}{E}. \tag{3.5}$$

The optical element M_E consists of the product of Gaussian distributed quantities $u_{\mathbf{k}}^{\beta}$ and V, which are uncorrelated, therefore it follows a Gaussian distribution as well. The optical oscillator strength, which is the square of M_E, therefore follows the PTD.

For the heterojunction system the other factor to consider is that the disorder itself can contribute to the electronic states as the lattice defective enough to ripple the crystalline Hamiltonian like in the aforementioned quantum well studies. In the experiment settings of this project, the ensemble average model is also viable as the area covered by the probe beam (5 μm FWHM in diameter) is relatively large compared to the lattice size and the MoS_2 diffusion length so that most of the charge transfer and the recombination processes happen locally and the probed area can contain a relatively large ensemble of similar systems. By using the published electron mobility of $\sim 50\mathrm{cm}^2\mathrm{V}^{-1}\mathrm{s}^{-1}$, the room temperature diffusion length of the MoS_2 is estimated to be $\sim 0.2\mu\mathrm{m}$ using a carrier lifetime of about 50 ps estimated by our experiments.

As estimated above the electrons in MoS_2 are in relatively localized states, we can write the wavefunctions for a single electron as $|\psi\rangle^r_{\mathrm{MoS}_2} = \sum_k u_k |k_{\mathrm{MoS}_2}\rangle$. The graphene layer, with a much higher carrier mobility, the electronic states can be reasonably approximated with a plane wave with wavevector $\mathbf{k}$ $|k\rangle_{gr}$. In the transfer process, the potential matrix V, the exact nature of which still not clear, responsible for the scattering between layers, should follow a Gaussian distribution as an ensemble as we assume disorder in the interface. Therefore, the total transfer rate for the transfer-back process is proportional to the square of the matrix element of the charge transfer process

$$M = \sum_{\mathbf{k}_{\mathrm{MoS}_2}} u_{\mathbf{k}_{\mathrm{MoS}_2}} \frac{\langle \mathbf{k} \approx 0|_{\mathrm{gr}} V |\mathbf{k}_{\mathrm{MoS}_2}\rangle}{E} \tag{3.6}$$

Similar to the reasoning for the III-V quantum well systems for an optical emission transition, the charge transfer matrix element here also follows a Gaussian distribution, therefore, the charge transfer rate back to the graphene layer will follow a PTD when it is squared.

3.4 Conclusions and Future Work

In this section, we have shown our studies on the charge carrier dynamics in the 2D heterostructure systems, which helped us understand the electronic states and the charge transfer dynamics. The result has shown that the carrier dynamics is dominated by the disorder in the CVD-grown materials. The main findings are:

- Very efficient initial charge transfer from the graphene to the MoS_2 was ob-

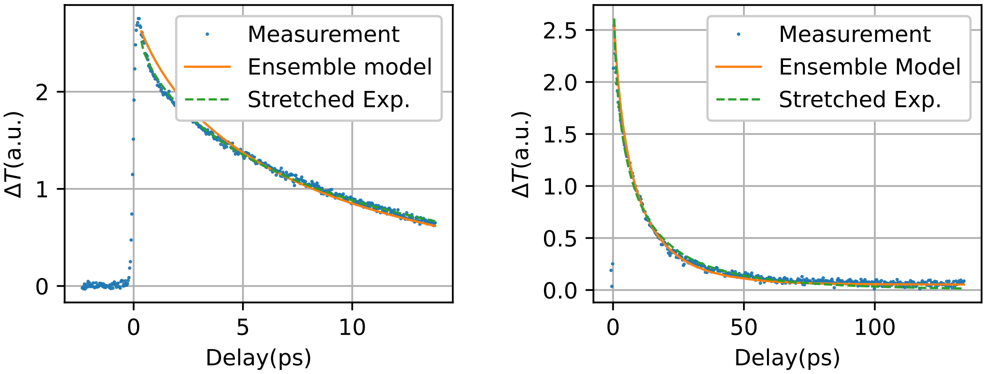

Figure 3.10: Results of the DR decay dynamics data fitted to stretched exponential function and to the Porter-Thomas distributed transfer rate. Both the left and right panels are the DR signals from the graphene/MoS_2 heterostructure sample with 800 nm pump. The probe are white light supercontinuum filtered with a 660 nm bandpass filter of 10 nm bandwidth. The left panel shows the DR of the first 10 ps delay and the right panel shows the longer delay range of 120 ps. The Porter-Thomas distributed transfer rate model fits with the long tail of the DR signal decay reasonably well while the stretched exponential function drops too fast at longer delays.

served, which in principle validates our proposed photo-detection mechanism using graphene as the absorption layer and the MoS_2 as the low dark current photoconductive transistor channel layer.

- The disorder in the MoS_2 is a limiting factor of the device performance because of the long-lived trapped charges. It limits the mobility of MoS_2, the operation speed or the bandwidth of the detector, and limits the overall responsivity due to the localized charge not contributing to the photoconductive detection process.

The next steps for further developing the 2D heterojunction photodetectors there can be three different directions: (a) to replicate the sandwich structure like the previous research; (b) to study the dependency of the charge transfer dynamics on the band alignment by applying bias voltages between the two layers; (c) to develop and optimize the CVD process of MoS_2 monolayers or substitute it with higher quality materials. The 2D material heterostructures can potentially make very unique photodetector devices.

BIBLIOGRAPHY

[1] Z. Xu, Z. Liu, D. Zhang, Z. Zhong, and T. B. Norris, “Ultrafast dynamics of charge transfer in CVD grown MoS2–graphene heterostructure,” Appl. Phys. Lett., vol. 119, p. 093102, Aug. 2021.

[2] C.-H. Liu, Y.-C. Chang, T. B. Norris, and Z. Zhong, “Graphene photodetectors with ultra-broadband and high responsivity at room temperature,” Nat Nano, vol. 9, pp. 273–278, Apr. 2014.

[3] H. Xu, J. Wu, Q. Feng, N. Mao, C. Wang, and J. Zhang, “High Responsivity and Gate Tunable Graphene-MoS2 Hybrid Phototransistor,” Small, vol. 10, no. 11, pp. 2300–2306, 2014.

[4] A. H. Castro Neto, F. Guinea, N. M. R. Peres, K. S. Novoselov, and A. K. Geim, “The electronic properties of graphene,” Rev. Mod. Phys., vol. 81, pp. 109–162, Jan. 2009.

[5] F. Xia, T. Mueller, Y.-m. Lin, A. Valdes-Garcia, and P. Avouris, “Ultrafast graphene photodetector,” Nature Nanotechnology, vol. 4, pp. 839–843, Dec. 2009.

[6] Z. Yin, H. Li, H. Li, L. Jiang, Y. Shi, Y. Sun, G. Lu, Q. Zhang, X. Chen, and H. Zhang, “Single-Layer MoS2 Phototransistors,” ACS Nano, vol. 6, pp. 74–80, Jan. 2012.

[7] M.-B. Lien, C.-H. Liu, I. Y. Chun, S. Ravishankar, H. Nien, M. Zhou, J. A. Fessler, Z. Zhong, and T. B. Norris, “Ranging and light field imaging with transparent photodetectors,” Nat. Photonics, vol. 14, pp. 143–148, Mar. 2020.

[8] D. Zhang, Z. Xu, Z. Huang, A. R. Gutierrez, C. J. Blocker, C.-H. Liu, M.-B. Lien, G. Cheng, Z. Liu, I. Y. Chun, J. A. Fessler, Z. Zhong, and T. B. Norris, "Neural network based 3D tracking with a graphene transparent focal stack imaging system," Nature Communications, vol. 12, p. 2413, Apr. 2021.

[9] X. Hong, J. Kim, S.-F. Shi, Y. Zhang, C. Jin, Y. Sun, S. Tongay, J. Wu, Y. Zhang, and F. Wang, "Ultrafast charge transfer in atomically thin MoS_2/WS_2 heterostructures," Nature Nanotechnology, vol. 9, pp. 682–686, Sept. 2014.

[10] H. Wang, C. Zhang, and F. Rana, "Ultrafast Dynamics of Defect-Assisted Electron–Hole Recombination in Monolayer MoS2," Nano Lett., vol. 15, pp. 339–345, Jan. 2015.

[11] J. He, N. Kumar, M. Z. Bellus, H.-Y. Chiu, D. He, Y. Wang, and H. Zhao, "Electron transfer and coupling in graphene–tungsten disulfide van der Waals heterostructures," Nature Communications, vol. 5, p. 5622, Nov. 2014.

[12] G. Froehlicher, E. Lorchat, and S. Berciaud, "Charge Versus Energy Transfer in Atomically Thin Graphene-Transition Metal Dichalcogenide van der Waals Heterostructures," Phys. Rev. X, vol. 8, p. 011007, Jan. 2018.

[13] F. Ceballos, M. Z. Bellus, H.-Y. Chiu, and H. Zhao, "Ultrafast Charge Separation and Indirect Exciton Formation in a MoS2–MoSe2 van der Waals Heterostructure," ACS Nano, vol. 8, pp. 12717–12724, Dec. 2014.

[14] J. D. Fowler, M. J. Allen, V. C. Tung, Y. Yang, R. B. Kaner, and B. H. Weiller, "Practical Chemical Sensors from Chemically Derived Graphene," ACS Nano, vol. 3, pp. 301–306, Feb. 2009.

[15] T. O. Wehling, K. S. Novoselov, S. V. Morozov, E. E. Vdovin, M. I. Katsnelson, A. K. Geim, and A. I. Lichtenstein, "Molecular Doping of Graphene," Nano Lett., vol. 8, pp. 173–177, Jan. 2008.

[16] J. W. Suk, A. Kitt, C. W. Magnuson, Y. Hao, S. Ahmed, J. An, A. K. Swan, B. B. Goldberg, and R. S. Ruoff, “Transfer of CVD-Grown Monolayer Graphene onto Arbitrary Substrates,” ACS Nano, vol. 5, pp. 6916–6924, Sept. 2011.

[17] H. Li, Q. Zhang, C. C. R. Yap, B. K. Tay, T. H. T. Edwin, A. Olivier, and D. Baillargeat, “From Bulk to Monolayer MoS2: Evolution of Raman Scattering,” Advanced Functional Materials, vol. 22, no. 7, pp. 1385–1390, 2012.

[18] L. M. Malard, M. A. Pimenta, G. Dresselhaus, and M. S. Dresselhaus, “Raman spectroscopy in graphene,” Physics Reports, vol. 473, pp. 51–87, Apr. 2009.

[19] E. S. Kadantsev and P. Hawrylak, “Electronic structure of a single MoS2 monolayer,” Solid State Communications, vol. 152, pp. 909–913, May 2012.

[20] K. F. Mak, C. Lee, J. Hone, J. Shan, and T. F. Heinz, “Atomically Thin ${\mathrm{MoS}}_{2}$: A New Direct-Gap Semiconductor,” Phys. Rev. Lett., vol. 105, p. 136805, Sept. 2010.

[21] F. Wu, F. Qu, and A. H. MacDonald, “Exciton band structure of monolayer ${\mathrm{MoS}}_{2}$,” Phys. Rev. B, vol. 91, p. 075310, Feb. 2015.

[22] R. Wang, B. A. Ruzicka, N. Kumar, M. Z. Bellus, H.-Y. Chiu, and H. Zhao, “Ultrafast and spatially resolved studies of charge carriers in atomically thin molybdenum disulfide,” Phys. Rev. B, vol. 86, p. 045406, July 2012.

[23] D. S. Chemla and D. a. B. Miller, “Room-temperature excitonic nonlinear-optical effects in semiconductor quantum-well structures,” J. Opt. Soc. Am. B, JOSAB, vol. 2, pp. 1155–1173, July 1985.

[24] E. A. A. Pogna, M. Marsili, D. De Fazio, S. Dal Conte, C. Manzoni, D. Sangalli, D. Yoon, A. Lombardo, A. C. Ferrari, A. Marini, G. Cerullo, and D. Prezzi,

"Photo-Induced Bandgap Renormalization Governs the Ultrafast Response of Single-Layer MoS2," ACS Nano, vol. 10, pp. 1182–1188, Jan. 2016.

[25] A. Steinhoff, M. Rösner, F. Jahnke, T. O. Wehling, and C. Gies, "Influence of Excited Carriers on the Optical and Electronic Properties of MoS2," Nano Lett., vol. 14, pp. 3743–3748, July 2014.

[26] W. Zhang, J.-K. Huang, C.-H. Chen, Y.-H. Chang, Y.-J. Cheng, and L.-J. Li, "High-Gain Phototransistors Based on a CVD MoS2 Monolayer," Advanced Materials, vol. 25, no. 25, pp. 3456–3461, 2013.

[27] J. C. Johannsen, S. Ulstrup, F. Cilento, A. Crepaldi, M. Zacchigna, C. Cacho, I. C. E. Turcu, E. Springate, F. Fromm, C. Raidel, T. Seyller, F. Parmigiani, M. Grioni, and P. Hofmann, "Direct View of Hot Carrier Dynamics in Graphene," Phys. Rev. Lett., vol. 111, p. 027403, July 2013.

[28] D. Sun, Z.-K. Wu, C. Divin, X. Li, C. Berger, W. A. de Heer, P. N. First, and T. B. Norris, "Ultrafast Relaxation of Excited Dirac Fermions in Epitaxial Graphene Using Optical Differential Transmission Spectroscopy," Phys. Rev. Lett., vol. 101, p. 157402, Oct. 2008.

[29] H. Wang, J. H. Strait, P. A. George, S. Shivaraman, V. B. Shields, M. Chandrashekhar, J. Hwang, F. Rana, M. G. Spencer, C. S. Ruiz-Vargas, and J. Park, "Ultrafast relaxation dynamics of hot optical phonons in graphene," Appl. Phys. Lett., vol. 96, p. 081917, Feb. 2010.

[30] B. A. Ruzicka, S. Wang, J. Liu, K.-P. Loh, J. Z. Wu, and H. Zhao, "Spatially resolved pump-probe study of single-layer graphene produced by chemical vapor deposition [Invited]," Opt. Mater. Express, OME, vol. 2, pp. 708–716, June 2012.

[31] E. Runge and R. Zimmermann, “Porter-Thomas Distribution of Oscillator Strengths of Quantum Well Excitons,” physica status solidi (b), vol. 221, no. 1, pp. 269–275, 2000.

[32] E. Runge and R. Zimmermann, “Optical properties of localized excitons in nanostructures: Theoretical aspects,” in Advances in Solid State Physics 38 (B. Kramer, ed.), Advances in Solid State Physics, (Berlin, Heidelberg), pp. 251–263, Springer, 1999.

CHAPTER 4

Charge Separation in InGaN Nanostructures

4.1 Introduction

The III-V compounds are unique because the large family of III-V materials, each having very different bandgaps, can form mixed crystalline alloys with varying bandgaps depending on the mixing rate, making them an extraordinary platform for optoelectronic applications since one can engineer their spectral response. The pioneers of III-V materials are phosphide and arsenide. They were widely used in the telecommunication industry since the 1980s for applications in the near- to mid-IR spectral range. The nitride generally have larger bandgaps than the arsenide and phosphide and thus are referred to as the wide-bandgap semiconductors. This allows the nitrides to be utilized in visible and UV wavelengths. Unlike silicon, the III-nitrides have direct bandgaps, which is an ideal property for better light-matter interactions, but the compound crystals are prone to have more defects, so the fabrication process is critical to their applications. They started to become widely used in optoelectronic applications since the advance of violet LEDs based on GaN technologies in the 1990s when high-quality epilayer GaN was grown and the research focused on the device physics based on III-N became possible.

4.2 InGaN in LEDs

4.2.1 III-nitride LED efficiency droop

In a typical LED structure which mainly consists of a PN junction, electrons and holes are injected into the junction region with a forward bias, emitting photons with radiative recombination. When dealing with only the light emitting material design the internal quantum efficiency (IQE) is the most relevant characteristic that describes the radiative recombination energy extraction rate that just comes out of the material. Along with the desired radiative recombination process, there can be multiple competing non-radiative processes that can reduce the IQE of an LED. Empirically the IQE is described with the ABC model where the IQE vs injection density n function is fitted with three coefficients A, B, and C each corresponding to the first, second, and third order of recombination processes as the most basic polynomial approximation. If summed up the IQE can be fitted with the model $\eta(n) = \frac{Bn^2}{An+Bn^2+Cn^3}$. At low injection density, the loss of IQE is attributed to the defect capture, i.e. the Schottky-Read-Hall or SRH recombination, and at high injection density, charge overflow and Auger recombination, which are non-radiative. If one plot out the trend of IQE vs. n, at a low injection density, the IQE increases as the defect states get saturated and it will start to drop after a point when the higher order nonradiative process becomes prominent. Although in real cases the physics are more complicated, this rudimentary curve usually follows the trend of the experimental IQE reasonably well. The drop of efficiency with increased injection charge density is often referred to as efficiency droop. It was argued that the main source of efficiency droop under high carrier injection rate often required in the green and blue LEDs for various lighting and lumination applications can be attributed to Auger non-radiative recombination [1]. The geometric and structural design of a realistic LED device will try to compensate for the efficiency droop and control the charge density within the vicinity of the maximum IQE, therefore, for the purpose of material characterization we are mostly concerned with the max IQE, which is only determined by the relative quantities of the A, B and C coefficients.

4.2.2 Quantum wells

Up to these days the most widely used microstructure for enhancing the radiative recombination efficiency is the multiple quantum well or superlattice structure. The names of multiple quantum well and superlattice physically refer to the same kind of device structure that consists of alternating hetero-epitaxial layers of two different III-V materials grown along a certain direction (usually along the c-direction of a wurtzite lattice) with well-defined boundaries between the regions. Conventionally the name multiple quantum wells refer to the structures where the wavefunction overlap between the adjacent wells is negligible. The quantum confinement of the quantum well structure makes the wavefunctions of electron and holes along the direction of the well at least have one confined state where they are compressed into 2D space (the so-called quantum confinement), thus enhancing the joint density (JDOS) of states at the exciton state compared to 3D excitons. [2, 3] If we look back at the ABC model the quantum confinement effectively enhanced the B coefficient by enhancing the JDOS of the radiative excitonic state.

4.2.3 Green gap

For lighting purposes where visible wavelengths are required, the nitrides are the ideal materials because the bandgaps of InGaN, the alloy of indium nitride and gallium nitride can cover the whole visible spectrum ranging from the near UV (with GaN) to near IR (with InN). However, the peak IQE of the LEDs in the green range has always been lower than that of the red or blue light due to a much higher indium concentration required. It is estimated to require around 25% indium to reach the range of green light. This is the so-called “green gap” of InGaN LEDs. The reason for the “green gap” is still in debate, and the following are the few main arguments. The high indium concentration leads to two effects that can cause reduced peak IQE. (a) The increased indium concentration needs a lower chamber temperature in the MOCVD or MBE processes and will lead to increased defects in the grown material. (b) The lattice constants of InN and GaN are different by $\sim 11\%$ so with high indium content the difference in the bond lengths of In–N and Ga–N will cause elastic strain in the alloy, enough to result in two effects that impair the peak IQE: First, the InGaN mixed crystal will tend to form separated In-rich regions and Ga-rich regions to relax the strain. The phase separation will result in rough terrains in the energy bands of the quantum well, making the electronic states localized and reducing the Coulomb enhancement effect.Second, there is the piezoelectric effect in the InGaN materials. The elastic strain due to lattice mismatch will induce a built-in piezoelectric field [4, 5]. When the quantum well is grown along the c-direction, the piezoelectric field will cause band bending and the e and h wavefunctions will be biased to different sides of the quantum well, resulting in a reduced wavefunction overlapping and effectively reducing the radiative recombination rate. This effect is known as the quantum confined Stark effect (QCSE). The debate on the main reason for the green gap, whether due to the defects, phase separation, or the QCSE has not come to a conclusion as of the time of writing.

4.2.4 Previous work: quantum disk in nanowires

The above introductions about ”quantum wells” are mostly concerned with one dimension, and indeed the majority of studies refer the name quantum well to the layered structure of alternating III-N epilayers grown on top of an extended surface. However, growing a large area of uniform and flat ternary (InGaN and AlGaN) quantum wells is difficult due to the strain, and this increased strain also leads to a larger piezoelectric field. So recently, to relax the strain and grow high-quality quantum wells, Prof. Mi's group at University of Michigan have grown the InGaN quantum well in the nanowires with a high indium content rate of 26% and achieved a large enhancement of radiation efficiency. Since the diameter of the nanowires are tens to hundreds of nanometers, a larger part of the InGaN is exposed to the surface on the side wall of the nanowires without creating the strain, they supposedly will tend to have less strain, thus less QCSE. The SEM images in those studies have shown that the quantum well structure formed in the hexagonal nanowires can make the well region grown into a special boomerang shape where the tilted interfaces partially align with the nonpolar facets of the lattice, possibly due to the difference in deposition speed of the center and side-wall regions, thus relaxing the QCSE and leading to a much enhanced radiative recombination efficiency that was observed in the published works [6, 7]. However, in the previous work the mechanisms for enhanced radiative recombination are still open questions that are essential for further development of these nanostructures. Understanding the charge carrier dynamics is a crucial part for finding the mechanisms for the radiative recombination enhancement and the critical limitations for the LED process, which is in turn important for designing and engineering the performance of the LED devices. With ultrafast spectroscopy, it is possible to distinguish the electronic states and the cooling and transition dynamics thus giving us further understanding of these LED structures.

4.3 InGaN in photocatalysis

4.3.1 Introduction to photocatalysis

Researchers and engineers over the years have put a vast effort into harvesting and storing solar energy in order to achieve carbon neutrality and energy sustainability.

The widely deployed photovoltaic facilities are able to convert the photon energy in the solar irradiation into electric energy and currently these facilities are directly coupled into the power grid. Also, research on the various chemical and fuel batteries provides a way of storing the electric energy in the form of chemical energy. Benefited from the development of catalysts, recent years have seen the development of hydrogen fuel cells that have an energy conversion efficiency higher than the fossil fuel generators, and they have come to application in powering the fuel cell vehicles[8]. The discoveries of photocatalysts made it possible to generate chemical fuels and ingredients under a mild ambient environment in a distributed manner, and it combines solar energy collection, conversion, and storage in the same place.

The study of semiconductor-based photocatalysis started attracting interest since Nakashima and Honda's 1970s research on the catalytic effect of TiO_2 in the water-splitting photoelectrochemical reaction [9], which for the first time demonstrated that it was possible to use semiconductor materials to bridge the gap between the solar emission energy and the bond activation barrier. Following the pioneering works, the more recent research explores the possibilities of various semiconductor catalytic material systems as well as the applications in other kinds of useful chemical reactions such as the selective oxidation of methane and the reduction of nitrogen. The capability of photocatalytic chemical reactions opens up the opportunities of scalable, low cost, portable and self-sustainable energy harvesting systems.

In general, the process of semiconductor photocatalysis consists of three main parts: (a) the hot charge carrier generation upon the absorption of the photon energy; (b) the separation of the generated electrons and holes and their transport to the surface of the catalyst body; (c) the carrier should cross the surface barrier and have the right energy level to activate the chemical bonds and induce the redox reaction. The last part largely involves the surface chemistry and the molecular electron states. Ideally the most suitable photocatalyst material should have efficient light absorption in the solar radiation range, and should be able to preserve the charge carrier energy while they transport efficiently to the surface.

Up to today, researchers have explored a wide range of photocatalysts including metal-oxides, metal-chalcogenides, silicon, III-V semiconductors and so on. The drawback of metal oxides such as TiO_2 is obvious: they usually have large bandgaps, therefore a large portion of the visible light cannot be absorbed thus utilized for redox reaction. Furthermore, the large bandgap leads to heavy holes and low mobility, so the transport efficiency to the surface is limited [10]. The metal-chalcogenides, silicon, and III-V semiconductors (other than the nitrides) suffer greatly from the corrosion that occurs in the harsh environment of photocatalysis. More recently the III-N materials have drawn the attention in the field of photocatalysis.

4.3.2 III-N in photocatalysis

There are several reasons why III-N materials are promising photocatalysts. As mentioned in the last chapter, the III-N materials have a large family that can cover the solar spectrum ranging from IR to UV. [11] This property ensures solar energy absorption efficiency. The alignment of the conduction and valence bands match with the molecular energy level of CH_4 or H_2O. Also, the III-N materials are extremely stable chemically in the harsh environments acting as catalysts compared to arsenides and phosphides, which could quickly degrade due to the chemically active ions generated as the intermediate reactants of the desired reaction. Ref[12] did a comprehensive review of III-N based photocatalysis for organic reactions.

4.3.3 Surface carriers

Catalysts do take part in the chemical reactions, and thus they make contact with the reactants. Therefore, in general, good surface-to-volume ratio is desired for good catalysts since the reactions has to happen at the interface of the catalysts and the reactants. Because of that, traditionally the catalysts are usually made in the form of powders. Although in the case of photocatalyst, it is the photo-carriers that take part in the chemical reaction rather than the “photocatalyst” themselves, they still have to make contact with the reactant nonetheless, so the surface-to-volume ratio argument also holds true for photocatalysts. However, in recent studies, researchers found that the best overall photocatalytic efficiency was achieved with 1D nanowires because compared to the powder form, the 1D nanowires are able to better preserve the crystal structure, resulting in less scattering centers when photo-carriers transport to the surface, thus having a higher overall efficiency. Nanowires that have the suitable geometry can be a good balance of surface-to-volume ratio and the charge transport efficiency[13]. Ideally to preserve most of the photon energy absorbed by the photocatalyst in the form of hot charge carriers the most desirable way would be to have ballistic transport from the point where the hot carriers are generated to the surface where the redox reactions happen. It would be of great importance if one can characterize the arrival time of the photocarriers to the surface. Since the photo-carrier energy at the surface would be the result of competing thermalization, scattering, trapping, recombination and transport, the faster the transport is, the higher efficiency and preserved photon-energy there will be.

4.3.4 Surface band bending

Previously Prof. Mi group in University of Michigan made III-nitride photocatalysts that are MBE-grown self-organized InGaN nanowires decorated with Rh/Cr_2O_3 nanoparticle cocatalysts. They found the material to be effective in unassisted water-splitting experiments. In this work, an apparent quantum efficiency of $\sim 12.3\%$ was achieved for unassisted water splitting in neutral ($pH \sim 7.0$) was achieved under visible light illumination[14] and no decrease of efficiency was found after a few hours of reaction. The nitride nanowires stayed chemically stable through the photochemical

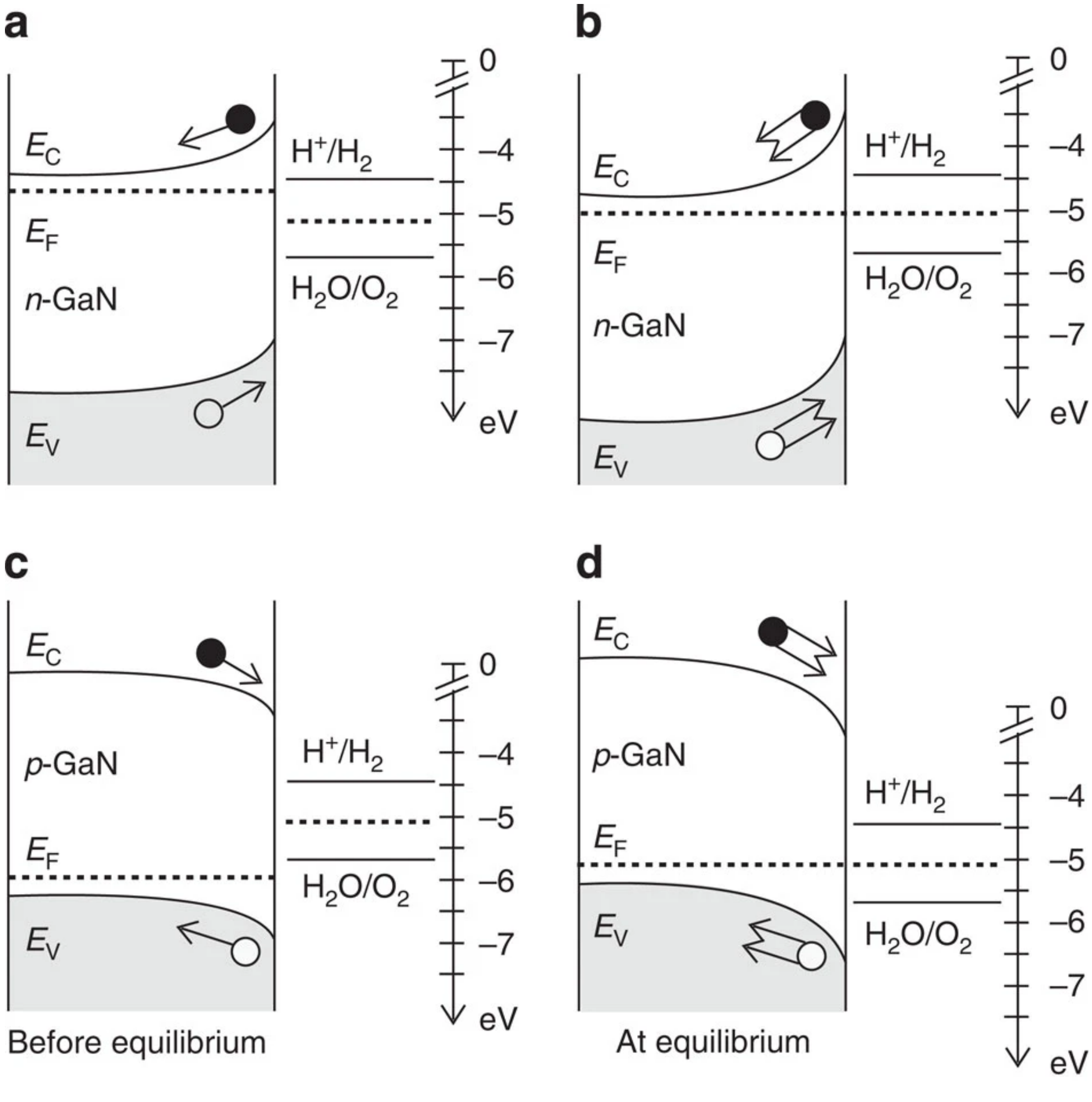

Figure 4.1: The diagram of band bending at the surface of GaN nanowires in a water-splitting experiment. a and b show the n-doped nanowires that have upward band bending at the surface. c and d show the p-doped nanowires having downward band bending[14].

reactions. The important factor related to optoelectronics is that the doping level of the InGaN nanowires have a big impact on the photocatalysis efficiency. As we mentioned on the last section the photochemical reactions happen at the catalyst surface. Further, the full water-splitting reaction consists of an oxidation part and a reduction part, the slower of which will limit the overall reaction efficiency. The surface band bending happens in most of the solid state materials when the solid state boundary condition breaks at the surface. Theoretical simulations and Raman found that the band bends upwards in n-doped nanowires and downwards in p-doped nanowires. In intrinsic nanowires, the band also bends upwards similar to the n-doped case. In water-splitting experiments it was found that there is an optimal p-doping level where the downward band bending becomes nearly flat in the water environment.

4.4 Sample preparation

The sample used in this chapter are all MBE-grown InGaN nanowires made by Dr. Mi's group at Michigan. There are two kinds of samples, one is the self-assembled nanowires used as photocatalyst, the other kind is the quantum well in nanowires with LED structures. Figure 4.2 shows the SEM images taken for similar samples fabricated for the previous works[6, 14].

4.4.1 Self-organized InGaN nanowires for photocatalysis

The samples used in the study of InGaN photocatalysis are the self-organized GaN nanowires with InGaN segments grown on top of the n-type silicon (111) surface. The nanowires are grown with the plasma assisted MBE process on the silicon wafer surface. The nanowire structure is formed from random nucleation. Due to strain effect in InGaN alloy, this material will start to have phase separation when it grows larger than a few decades of nanometers. Therefore, the InGaN is grown in the form

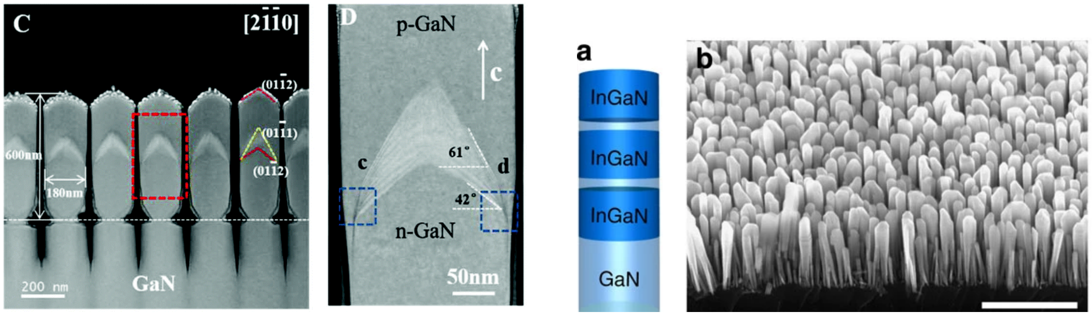

(a) Quantum well in nanowire

(b) InGaN in self-organized nanowires

Figure 4.2: The SEM images taken for samples grown with the same technique and parameters in previous works. a the quantum well in nanowire structure. It has the same structure as F1921 sample in the main text. b the GaN self-organized nanowires with InGaN segments. The samples N5099 and N4773 are grown with the same technique as this sample.

of small segment embedded in the GaN nanowires by switching the indium source. As reported in the previous work, the nanowires have an average height of $\sim 400-600$nm and the top region diameter of $\sim 40-100$nm. The embedded InGaN segments are about 20 to 40 nm thick that sum up to a total thickness of 80nm for each wire. We prepared one sample N5099 that is optimally p-doped with Mg, and the other sample N4773 that is intrinsic InGaN. The doping level of N5099 is tuned to have the optimal overall water-splitting photocatalysis performance when decorated with Rh/Cr_2O_3 particles. The only difference between N5099 and N4773 is the doping. We use the N4773, intrinsic InGaN as a reference to the doped sample. Part of the optimally p-doped InGaN nanowires are split off and decorated with Rh/Cr_2O_3 nanoparticle co-catalysts. The growth area of the wafer has a diameter of 10 cm. so there is unavoidably a temperature gradient across the wafer. The center part of the wafer has a higher temperature than the outer part, so InGaN bandgap is thus shifted from UV near the center of the substrate wafer to about 550 nm in wavelength. This can be visually recognized roughly by the coloration of the nanowires, which is grayish near the center and gradually becomes yellowish toward the wafer edge.

4.4.2 Quantum well in nanowire LED structure

The sample (F1921) used in the study of LED structure is the InGaN/AlGaN MQW in the PN junction region in the GaN nanowires grown along the *c*-axis by selective area epitaxy (SAE) technique using a molecular beam epitaxy (MBE) system (Veeco 930) equipped with a radio frequency plasma-assisted nitrogen source on top of 4.5 μm n-GaN template on sapphire wafer. The backside of the sapphire wafer is unpolished and coated with Mo metal particles so that it resembles a black body and the temperature can be easily calibrated with its IR radiation. The GaN substrate is masked with 10 nm thick Ti film and patterned with e-beam lithography and reactive ion etching to form a photonic crystal array of hexagon openings on the mask and the nanowires are grown through the unmasked GaN substrate from the bottom up. The openings on the Ti mask define the cross-section shape and the arrangement of the nanowires. There are 64 regions (arranged as a 8×8 array) of hexagonal nanowire arrays on a same piece of substrate, each having a different configuration of the wire size diameter and spacing. A typical configuration of the nanowire has a diameter of $d \sim 220$ nm and a periodicity of $A \sim 300$ nm. The periodicity denotes the lattice constant of a hexagonal lattice of the photonic crystal structure formed by the nanowire arrays. Other than the different lateral configuration defined by the Ti mask, all the nanowires are grown in parallel, therefore they have very similar vertical structure and height. The content rate of the In incorporation is controlled by controlling the temperature of the sample. The first or the bottom part of the nanowires are about 450 nm of n-GaN grown at ~ 880°C at a growth rate of ~ 120 nm/hour. This part is the n-doped side of the PN junction. Then 6 pairs of intrinsic InGaN and AlGaN layers, each having about 4 nm thickness was grown on top of the n-GaN and this is the quantum well region. A lower temperature of 640°C and an increased nitrogen source intensity was used to enhance the indium incorporation. The thickness of the quantum wells are estimated by the growth rate and the growth time, namely, 2 minutes at a rate of $\sim$ 120 nm/hour. On top of the well region, a pair of p^+/n^+ GaN tunnel junction before the final p-GaN region and cladding. Previous studies have shown that the tunnel junctions can enhance the carrier injection and mitigate the efficiency loss due to high resistance p-type GaN layers and p-type contacts in the MBE or metalorganic chemical vapor deposition (MOCVD) grown quantum well LEDs [15, 16]. It can be seen from the SEM images that the growth of the quantum well layers is not uniform across the nanowire and the few layers are not exactly the same. The center part of the nanowire grows slightly faster and outer part grows slightly slower, making the well region slightly tilted so that they are not perfectly aligned with the *c*-plane but rather toward a less polar facet. In the previous work that mentioned earlier this was the argument for the reduced QCSE that leads to the enhanced radiative recombination rate. Fig. 4.2a shows the SEM of the same kind of structure grown with identical parameters. Fig. 4.3 shows the illustrative diagrams of the wafer configuration and the exaggerated side view of the nanowire cross-section.

4.5 Charge separation in self-organized nanowires

4.5.1 TRPL and TRDR experiments

We first carried out room temperature pump-probe experiments and TRPL measurements for the N5099 and N4773 samples, which are the self-organized nanowires. Since the nanowires are grown on a piece of silicon wafer, which is opaque in wavelength range corresponding to the bandgap energy of InGaN bulk used in this work, it is not feasible to make DT measurements. The TRDR setup is very similar to the setup used for the CVD MoS_2/graphene heterostructure experiments except for slightly different spectral filtering. Refer to Figure 3.3 for a schematic diagram of the experimental setup.

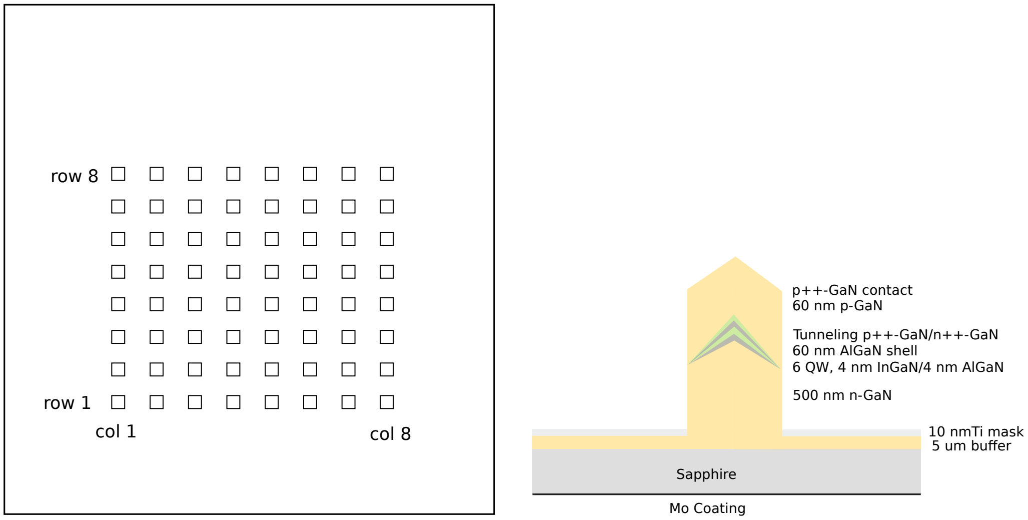

(a) (b)

Figure 4.3: The not-to-scale diagrams of the InGaN/AlGaN quantum well in nanowire structure. a The diagrams of the 8×8 array of nanowire regions. Each of the squares corresponds to a nanowire diameter and spacing setting. The size of each square is $100 \times 100 \mu\text{m}^2$. A typical setting of the nanowire size is about 220 nm in wire diameter and 300 nm in the adjacent wire distance. b The side view demonstration of the nanowire. Note that this diagram is not to-scale. The wire size is actually much smaller compared to the substrate. The quantum well region is also exaggerated in size. The actual shape of the wells are also nonphysical in this diagram.

Both the N5099 and N4773 samples have very rough and disordered top surface due to significant randomness in their growth process so that they will disperse and scatter the incident light. As a result, we found that the nanowire samples have a reflectance of less than 1%. For the purpose of $\Delta R/R_0$ measurements the low R_0 level poses challenges for the dynamic range of the differential measurements, which is also limited by the damaging threshold of the material, the fluence ratio between the pump and the probe pulses, and the noise floor of the electronic circuits and the laser source. In order to achieve a reasonable power scaling range for power dependent dynamics in the nanowires, a lens with a long focal length of 10 cm was used to focus the beam on the sample, and the pump beam is carefully defocused slightly to expand the spotsize at the sample, which is mounted on the focal plane of the probe beam in order to make the reflectance collected by the same focus lens collimated. With the 10 cm focal length lens, the spot size of the probe beam is estimated as about 50 μm at the focus, and the defocused pump beam has a spot size of about 100 μm at the focal plane of the probe beam.

4.5.2 Spectral-resolved PL and DR

Figure 4.4 shows the spectral resolved DR response and the raw TRPL trace taking with the streak camera. The three rows correspond to three different samples. From top to down, they correspond to the undecorated p-doped InGaN, the intrinsic InGaN, and the p-doped InGaN nanowires that has Rh/Cr_2O_3 nanoparticles decorated on the sidewalls. The left column corresponds to the spectral-resolved DR measured at different pump-probe delays by scanning the monochromator wavelength while keeping the delay fixed. A 450 nm long pass filter was inserted in the PL collection path in Figure 4.4b to protect the streak camera from the scattering of the excitation source. All the DR and PL measurements showed mainly a single broad peak. The central wavelengths depend on the region of the sample due to a temperature gradient across the sample during MBE growth process that leads to a gradient of indium incorporation rate that shifts the bandgap of the InGaN. The peak widths of the PL shown here are about 20 nm (corresponding to $\sim$ 100meV) that can only be attributed to non-homogeneous broadening that is related to the variation of indium incorporation rate possibly within the nanowires and between the nanowires. The sample has no positioning marker, so the central wavelength can usually vary between different measurement sessions by tens of nanometers, but the time-resolve features are similar. If we read the TRPL raw data along the time delay (y axis), we can find that the PL dynamics is similar for different wavelengths. The DR spectrum of the intrinsic sample (Figure 4.4c) showed a second peak in the spectral range where the reference reflectance power is low. More repeated experiments will be required to further study the more exact DR spectroscopy of the intrinsic InGaN nanowires. As the initial ultrafast characterization experiments here we can stay with the conclusion that both the DR and PL spectra indicated a major inhomogeneous broadening.

4.5.3 Time-resolved PL and DR

We obtained the time-resolved DR from the three kinds of samples by keeping the monochromator at a fixed wavelength of 470 nm, which is covered in the exciton peak range, while scan the pump-probe delay stage. We also extracted the time-resolved PL at the peak wavelength by summing the PL counts in a window of 10 nm. The dynamics represents an ensemble, so they are similar within the broad peak range due to the wire variations. Figure 4.5 showed the DR dynamics of the three kinds of nanowires. The pump source is the attenuated SHG of a RegA system that has a repetition rate of 250 kHz. The probe is the supertinuum generation by focusing 20% of RegA output (approximately 200 mW) onto a piece of sapphire wafer. The probe is pre-filtered to remove excessive pulse energy before incidence on the sample and the reflected probe is then spectral filtered by a monochromator. The excitation

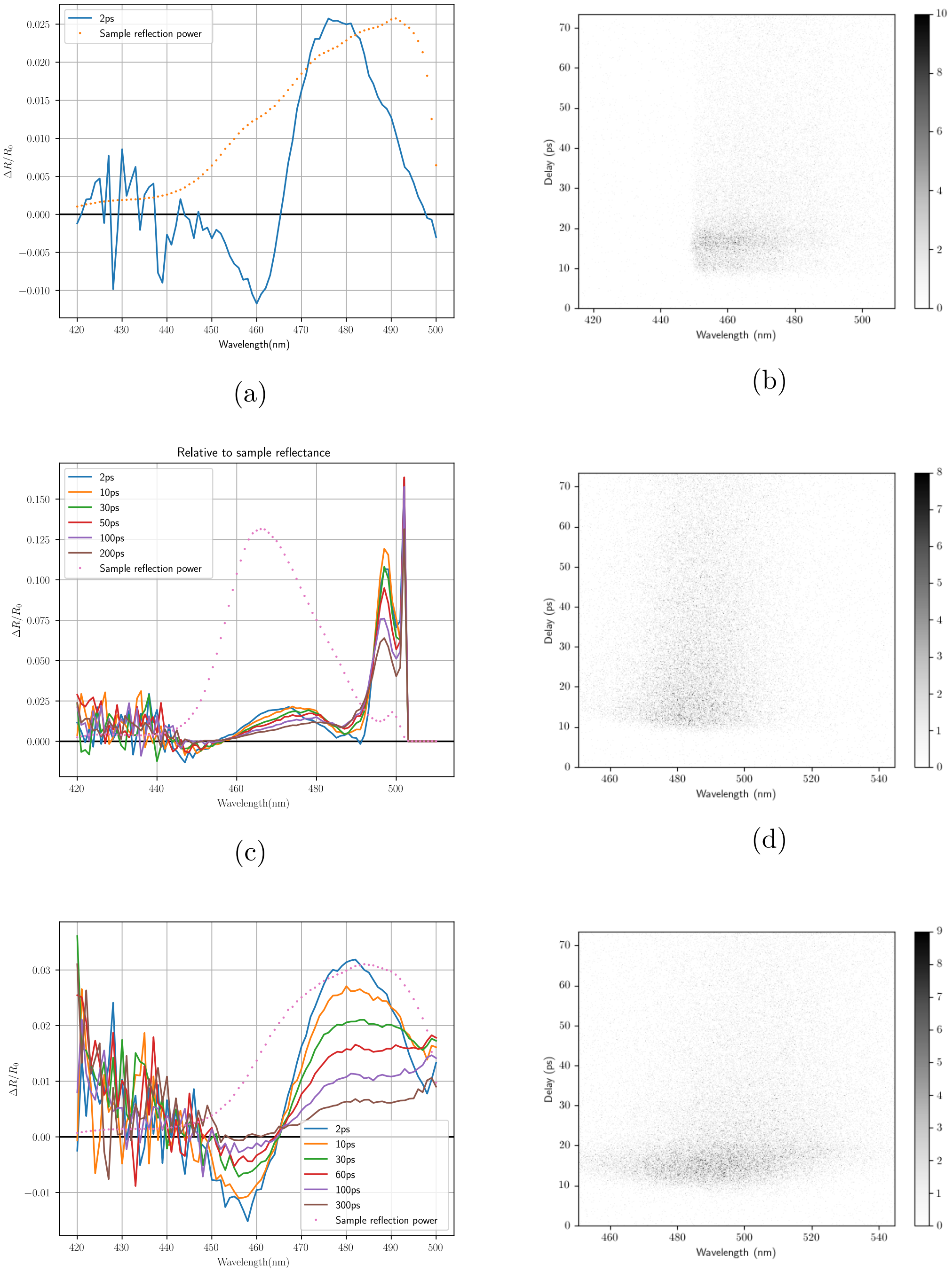

(a)

(b)

(c)

(d)

(e)

(f)

Figure 4.4: The spectral-resolved PL and DR measured on each of the samples. The three rows correspond to three different samples, each being the undecorated p-doped InGaN (N5099), intrinsic InGaN (N4773), and p-doped InGaN with Rh/Cr_2O_3 nanoparticles decorated at the sidewalls (decorated N5099). The left column is the spectral-resolved DR response from the three different samples. Different solid lines correspond to the DR spectrum measured at different delay times. The dotted line is the reference reflection power spectrum. The right column is the raw streak camera traces of the TRPL of the samples.

power (measured by the average power) of the pump beam is 15 μW for all the experiments shown in Figure 4.5, which corresponds to a pulse energy of 60 pJ and a fluence of about 6 μJ/cm^2 with a spotsize of $\sim 30\mu$m. All three time-resolved curves show a fast rising edge that is instrument limited and slow decay curves afterwards that last for a few hundred picoseconds. The three curves are qualitatively similar. Figures 4.6a and 4.6b show the TRPL curve of the three samples. The excitation source of the PL is the SHG from a Ti:sapphire oscillator with a repetition rate of 75.8 MHz and attenuated down to 10 μW, which corresponds to a pulse energy of 0.13 pW and a fluence of about 15 nJ/cm^2. The two figures showed experiments that measured the same PL signal but with different settings of the delay time range. The rising edge of the p-doped nanowire PL signal showed a "shoulder" that indicates that the PL should be attributed to two kinds of mechanisms. The rising edges of the other two samples showed immediate rise after excitation that are consistent with the DR rising edge. Unfortunately, the origin of the small shoulder is still unclear. The decay dynamics, however, show a distinct difference between p-doped and intrinsic samples, where a fast decay after initial carrier injection is observed in the p-doped samples (both undecorated and decorated) but not in the intrinsic samples. In this exploratory study of the PL and DR dynamics in the nanowires, we will focus on the decay dynamics.

We tentatively fit the decay curve of the PL and DR with a multi-exponential function model that represents multiple carrier relaxation processes. We start with bi-exponential fit and try to add or remove an exponential component if the fit fails. All three DR decay curve can be reasonably well fit with a bi-exponential function. The PL dynamics of the two p-doped InGaN nanowires can be fit with three exponential functions in the long range measurements and the curve fit to the PL decay curve of the intrinsic InGaN sample only works without the fastest component. The fitted curves are shown with the experiment data in the same plots. The fitting parameters

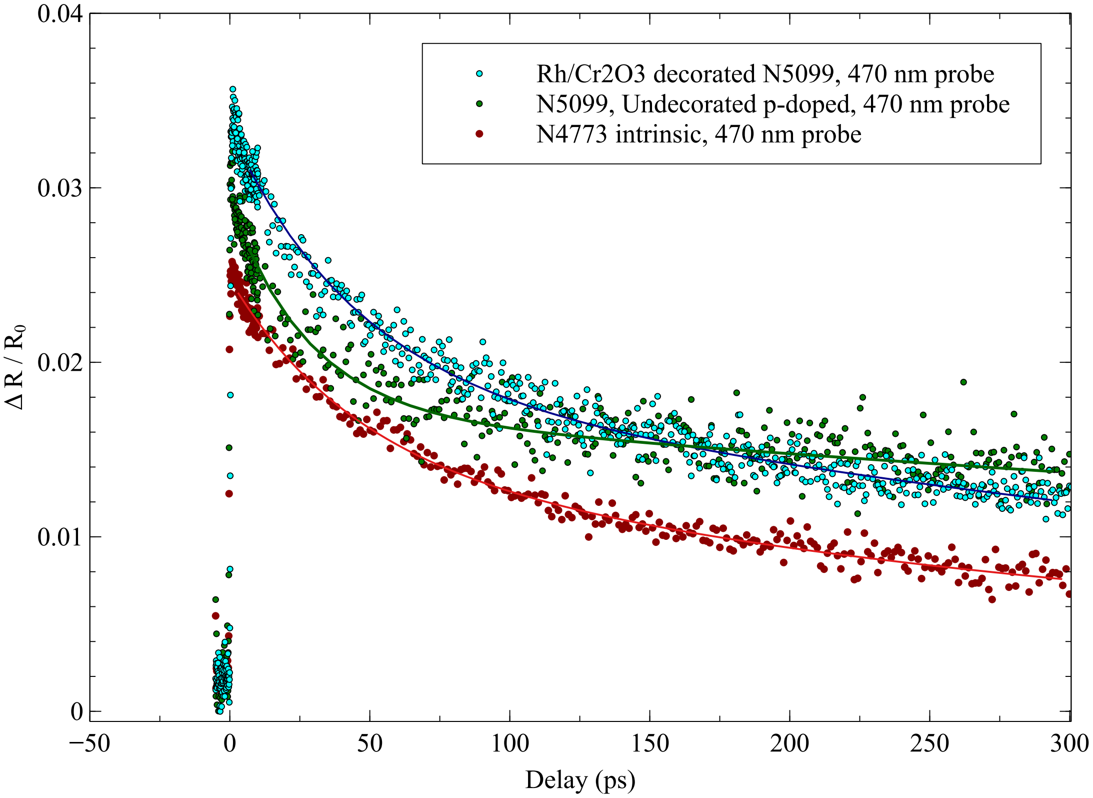

Figure 4.5: The time-resolved DR of three different kinds of samples. The circles are the experiment measurements. The solid lines are the bi-exponential fit to the experiment data. Refer to main text for the details.

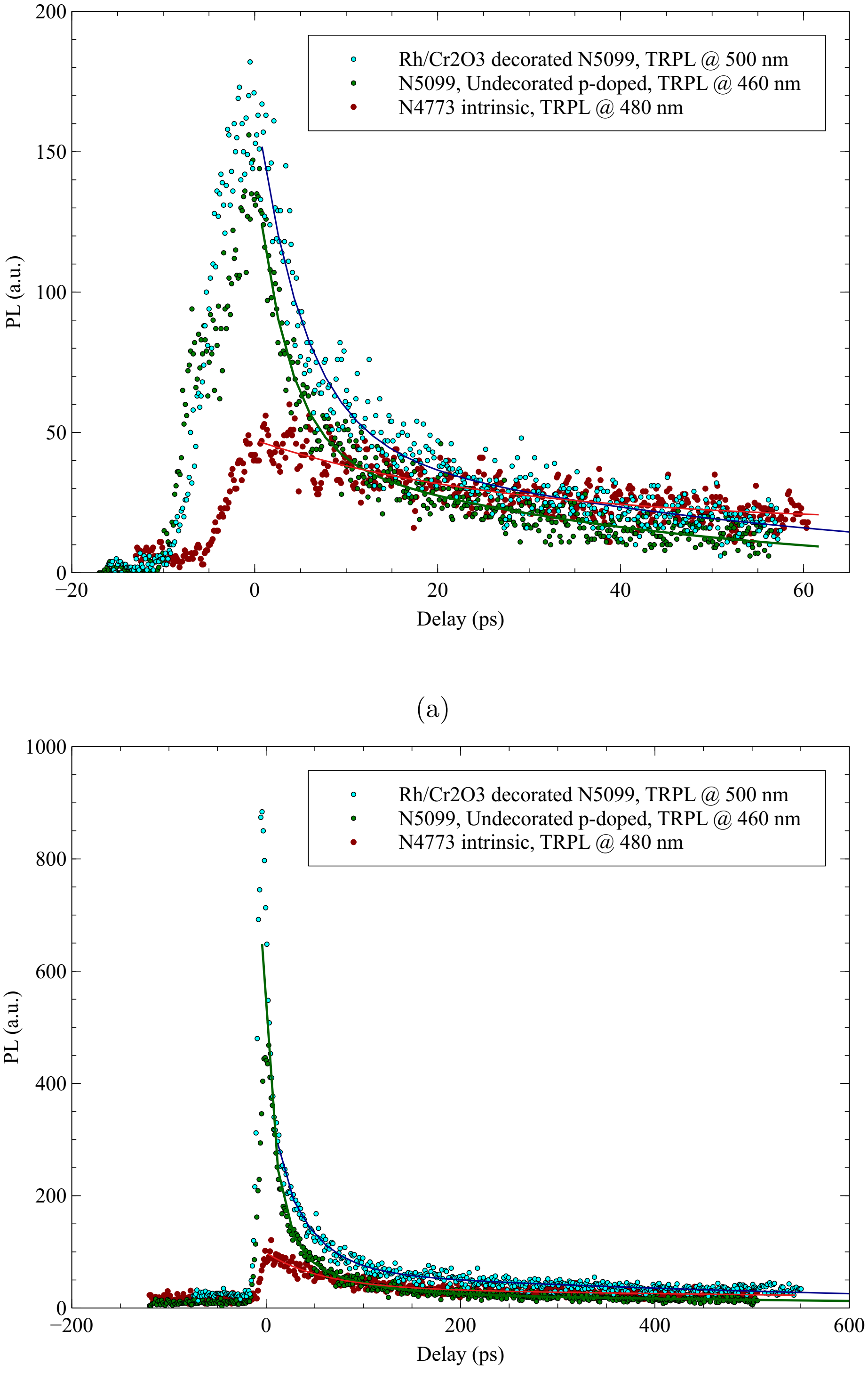

(a)

(b)

Figure 4.6: The PL dynamics of the three different samples sliced from the streak camera trace at their corresponding peak wavelengths with a spectral window of 10 nm. The circles are the experiment measurements and the solid lines are the multi-exponential fits. a and b measure the same signal but with a different time window size (and of course, the step size, because the streak camera have the same number of pixels).

	DR		PL short range		PL long range		
	t_m(ps)	t_s(ps)	t_f(ps)	t_m(ps)	t_f(ps)	t_m(ps)	t_s(ps)
Intrinsic	43	3.4×10^2	–	27	–	59	1.27×10^3
Undecorated p-dope	28	1.32×10^3	3.5	39	12	56	7.0×10^2
Decorated p-dope	44	6.3×10^2	5.1	53	4.9	36	6.2×10^2

Table 4.1: Multi-exponential fitting time constant parameters.

of the time constants are listed in Table 4.1. We matched the numbers with the rough orders of magnitude of the time constants and categorize them into a fast decay that lasts about a few picoseconds, a medium decay that corresponds to a time constant of sub-hundred picoseconds, and a slow decay that lasts hundreds of picoseconds. Since the PL data only covered 600 ps delay range and the DR measurements 300 ps, the few hundred to a thousand picosecond time constant of the slowest decay component can have an unknown large error bar.

We notice that the most significant dynamics difference happened between the PL decay dynamics of p-doped and undoped nanowires. While all the DR decay curves can be fitted reasonably well with a 30- to 40-ps component and a slow component regardless of the doping, the p-doping seems to have created a fast decay component right after the initial charge capture that was not probed in the DR experiments. The only difference between the p-doped and intrinsic nanowires is the added Mg source during the growth of the p-doped nanowires. Since the relative DR levels measured on these two samples are in the same order of magnitude, we would expect a similar carrier density in these two cases. Simply comparing the DR decay dynamics of the two samples that only have different doping levels, and we notice that the DR, similar to what we discussed in the MoS_2/graphene heterostructure case, measures the remaining charge in the InGaN nanowires, we find that the doping does not change the dynamics of total charge population in the nanowires, and we can consider it as the total recombination dynamics of charge carriers. But the radiative recombination of the photocarriers, which is what we measured with the TRPL experiments, seem to take a different path.

4.5.4 Density dependent TRDR

We would like to be cautious about the dynamics change with carrier density. The excitation source for the DR measurements is the second harmonic generation (SHG) of a RegA output which has a repetition rate of 250 kHz, which is about 350 times slower than the excitation source of the Ti:sapphire oscillator used for making the PL measurements but the average power and the focusing conditions are similar for these two experiments. Therefore, the optical energy fluence, which is proportional to the charge carrier density generated in the nanowire body, are different by about 350 times. It is possible that the PL and DR dynamics difference is due to the carrier density effect. One possible guess would be that the fast component corresponds to some efficient trap capture that leads to a fast decay in the carrier density after initial injection. With a high carrier density as in the DR experiments, the trap states are either screened or quickly saturated by the high density. The fast component might be hidden in the DR measurements but below the instrument sensitivity threshold.

The density dependent DR experiment is conducted with a long-focal-length lens and a slightly defocused pump beam as described earlier. The carrier injection density was down-scaled for about 100 times by expanding the pump beam spotsize by about 3 times in diameter and using a band pass filter centered at 480 nm with a bandwidth of 10 nm on the supercontinuum probe before the beam hits the sample. The resulting density dependent TRDR of the p-doped InGaN nanowires is shown in Figure 4.7. For this set of experiments, with the pump fluence decreasing from 2 μJ/cm^2 down to 0.2 μJ/cm^2, although the pulse energy fluence did not reach the level of excitation used in the PL experiments, we find that the trend of the recombination dynamics slows down with lower charge injection density. This trend of slowing down with decreased charge density is also be able to explain why we find that the medium fast process of the TRPL is in general slower than the corresponding component of the TRDR measurements. We again attempted to fit the decay curve with bi-exponential functions to study the dynamics characteristics. Figure 4.7c and 4.7d show the fitting parameters plotted against the pump fluence. Figure 4.7c shows the two time constants versus the pump fluence, and Figure 4.7d shows the ratio of the faster components takes up in the total signal. With the lowest pump fluence setting achieved in the experiments, the bi-exponential function fails to fit the dynamics, so we marked the ratio to be 0. The trend of the time constants is not clear enough to draw any meaningful conclusions. But the ratio of the faster components, which should actually be called the medium fast component, decreases with decreased pump fluence: no few-ps fast component appears within the instrument sensitivity range.

4.5.5 Discussions

We now discuss the possible physics corresponding to the three timescales we identified in our first set of experiments. First, we discuss the fast component that lasts for a few picoseconds, which is only observed in the p-doped InGaN. We recall that the DR signal measures the remaining charge population in the energy level it probes, and in the case of a significant inhomogeneous broadening, proportional to the remaining charge density in the vicinity of the energy level. Although the pump density dependent DR experiment was not able to reach the excitation level of the PL experiments shown in Figure 4.4, the trend is obvious: the faster component gets smaller under weaker excitation density, and the few-picosecend process was not detected. This indicates that after the initial charge carrier injection by the pump pulse, for the first few picoseconds there was some efficient radiative recombination, but after that, although the total charge density decreased by the time constant of 50 to 70 ps, the radiative recombination was suppressed. We believe that this process corresponds

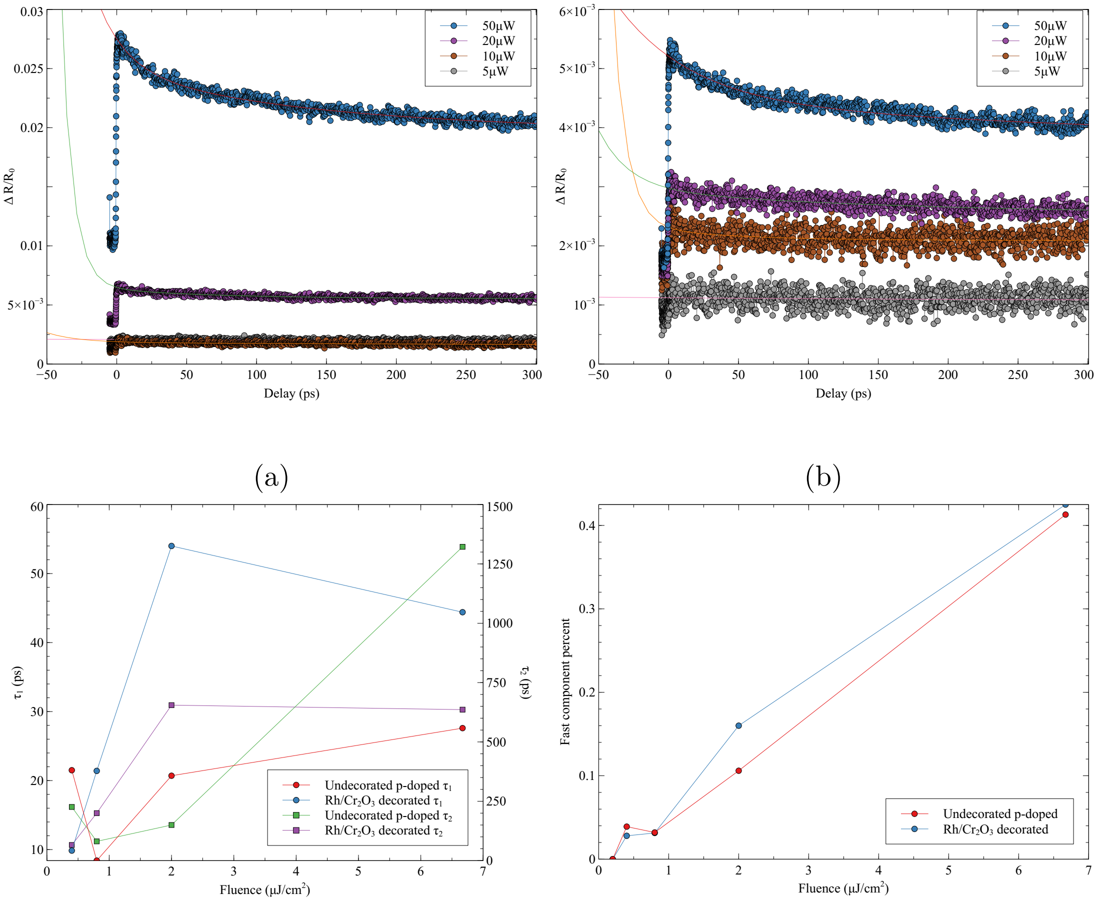

(a) (b)

(c) (d)

Figure 4.7: The density dependent TRDR curve of the p-doped InGaN nanowires. a shows the DR of nanowires with no decoration (sample N5099) and b shows the TRDR of the nanowires decorated with Rh/Cr_2O_3 co-catalysts (decorated sample N5099). The circles are the experiment data and the lines are the bi-exponential fits to the decay curves. An extra constant is appended as a fitting parameter to account for the process longer than the pulse intervals. c show the time constant fitting parameters of the medium fast component and the slow components of the bi-exponential fits to the TRDR decay curve, respectively. The faster time constant corresponds to the left axis and the slower time constant right axis. d shows the portion the faster components take up in the total DR signal.

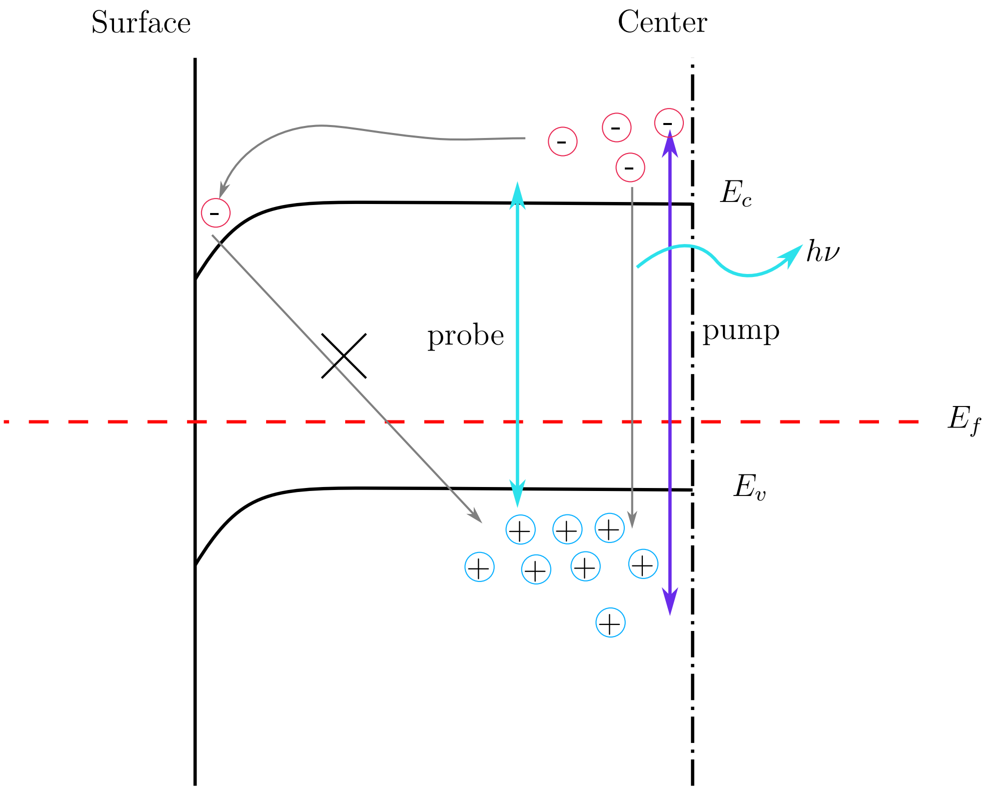

Figure 4.8: A schematic diagram of the charge separation in the self-assembled nanowires.

to the charge separation due to the band bending near the nanowire sidewall surface that drives the two kinds of charges drifting toward different directions based on three reasons: the absence of the fast component from the DR decay dynamics, the absence of the fast component from the intrinsic InGaN nanowires, and our estimate of the diffusion time based on the nanowire sizes.

Figure 4.8 shows a schematic diagram of a vertical cross-section of a nanowire. In a nanowire that is p-doped, because of boundary Fermi level pinning, there will be an internal polarization field that bends the band upwards as shown in the diagram according to previous work on the same system[17, 14, 13], and the electrons are driven toward the surface. When the nanowire is undoped, the bending will be weaker and downward according to previous calculations, which will drive the holes to the surface instead. Since the surface transport efficiency depends on the interplay of the transport, trapping, and recombination dynamics, the band bending significantly affects the photocatalysis (PC) efficiency as well as the recombination dynamics. Since the radiative recombination requires the presence of both the electrons and holes in the same location, the PL dynamics actually measures the dynamics of colocated carrier density. Previous studies on the InGaN, GaN and InN found that the electron mobility is in the range of 40 to 800 $\mathrm{cm}^2\mathrm{V/s}$[18, 19] which correspond to a diffusion rate D ranging from 1.2 to 20 cm^2/s under room temperature according to the Einstein's relation. The hole mobility is in the range of 3 to 200 $\mathrm{cm}^2\mathrm{V/s}$, which are a few times slower than the electrons, mainly due to the larger effective mass of holes compared to electrons. Although admittedly a high mobility is desired for the PC applications, the sample used in this study is not particularly engineered for high carrier mobility, we would expect the carrier mobility to be in the low end of its range. The scanning electron microscopy (SEM) image of a similar sample (Fig. 4.2b) shows that the top surface diameter of the nanowires range from 40 nm to 100 nm[17, 14, 13]. We then estimate the diffusion time to the surface to be about 0.2 to 3 ps for an average sized nanowire. A likely explanation is that the electrons diffuse faster than the holes and in p-doped nanowires the electrons generated in the bulk InGaN diffuse to the built-in polarization near the surface and then the built-in field drive the electrons further toward the surface, thus the electrons and holes are separated and the radiative recombination is surpressed. The fast component of the PL dynamics is attributed to the electron diffusion time to the surface. When the InGaN is intrinsic the band bending is reversed, and we are supposed to see the diffusion of holes. But since the effective mass of holes are a few time larger than the electrons in InGaN, the diffusion time will be longer and they may not be distinguishable with the medium fast component.

Then we discuss the slower time constants. Both of the medium fast and the slow components are present in both the DR and the PL dynamics, so they are not related to the charge separation. After the charge separation when there is no more charge transport, both the DR and the PL decay follow the remaining charge density decay. Therefore, we attribute the medium and slow components to the relaxation of carrier density, which may correspond to radiative recombination and the trapping at the surface among the relevant physical processes.

4.5.6 Summary

We have studied the TRPL and TRDR dynamics of the self-organized InGaN nanowire system for the purpose of photocatalysis applications. We summarize our findings and conclusions based on the previous discussions in this section.

We have presented the TRPL and TRDR results on three different samples, the Rh/Cr_2O_3 decorated p-doped nanowire (N5099-RhCr), the undecorated p-doped nanowire (N5099) and the intrinsic InGaN nanowires (N4773) where N4773 being the control sample. For all three cases both the DR spectrum near time-zero and the PL spectrum show a smooth broad feature meaning that the nanowires have significant inhomogeneous broadending that arises from the randomness of indium composition rate. All the DR dynamics have instantaneous rising edge and a decay time that can be described with two exponential components each in the order of 20 to 40 ps and more than 100 ps. However, the p-doped nanowires all have a fast component in the PL dynamics that is not observed in the DR signal. Since with significant inhomogeneous broadening the DR measurement will be proportional to the sum of electron and hole charge density but the PL emission will require the presence of both electrons and holes, we attribute the fast decay component of the PL dynamics to the electron diffusion and charge separation due to the band bending near the nanowire surface. The slower decay dynamics are observed in both the PL and the DR decay curves, and they are attributed to the charge density relaxation. In this study we demonstrated how the PL and DR combined can be applied to characterize charge separation in nanowires.

4.6 Charge separation in tilted quantum wells

4.6.1 Room temperature TRDR and TRPL of quantum well

We first conducted preliminary room temperature DR and PL experiments on the InGaN quantum well in nanowire samples. Both experiments use the excitation or pump source of RegA with similar level of carrier density. The setup for the DR experiment is essentially the same as the above-gap excitation DR experiment in the MoS_2/graphene heterostructure except for the excitation power and the spectral filtering for the different probe photon energies. The pump is the SHG of the RegA, which has a wavelength of 400 nm, and a repetition rate of 250 kHz, and the probe is also supercontinuum generated from the same RegA source. The probe beam is spectral filtered with a 550 nm short-pass filter to avoid excessive energy of longer wavelength components in the supercontinuum probe. The reason for the spectral filtering is that the power spectrum of the supercontinuum is heavily weighted towards the source wavelength, i.e., 800 nm, therefore the red components take up the most part of the total power, but they do not contribute to the spectroscopy because the preliminary PL spectrum under CW excitation mainly showed emissions near 510 nm. It is necessary to remove the excessive power to protect the sample from damaging. With the extra power removed, it gives the experiment more headroom to scale the excitation power for power-dependent experiments, and it also reduces unwanted thermal effects of the probe. In the PL measurements the sample is also excited with the same SHG source with the same focusing lens, and there is no probe involved. The sample is excited with normal incidence and the PL signal is also collected with the same focusing lens at normal direction. The PL signal is separated from the excitation source with a 450 nm short-pass dichroic mirror and directed towards a Chromex monochromator. A Hamamatsu photon multiplier tube (PMT) (model H4722-20) is placed at the exit of the monochromator and connected to a SR-400 pulse counter unit gated by an optical chopper placed on the excitation path. The PMT head has a GaAsP photocathode that is sensitive to the spectral range 300 nm to 720 nm with a peak quantum efficiency of 40%.

The focused beam size of the pump is estimated to be about 10 μm indicated by the 10% to 90% distance with a razor blade cutting method. The bandgap of GaN junctions or AlGaN barriers are all higher than that of the pump photon energy, so the pump only generates e-h pairs in the InGaN layers of the quantum well region ideally. In the quantum well region, the InGaN layers are pumped above their bandgap, possibly up to multiple quantum well levels, the exact numbers are still unclear. The probe photon energy range of the filtered supercontinuum covers a span of the energy levels around the most distinctive PL peak under the same excitation source (Fig 4.12a). The corresponding band structure is schematically shown in Fig. 4.9.

In the DR spectrum shown in Fig 4.11 two DR peaks appeared on the spectrum, at 479 nm and 506 nm, respectively. The higher energy DR peak does not show up in the room temperature PL spectrum while the 506 nm peak corresponds to the major peak of the PL. Both the DR peaks have shown a bipolar feature and are very sharp compared to the PL peaks. The higher energy PL peak matches with the sharp DR peak at 506 nm but the PL peak is much broader than that of the DR peak. Below the level of 506 nm, a broader PL peak around 550 nm probably exists, but it is hard to observe since it is near the edge of the edge pass filter used in the DR experiment. Here we notice that in order for PL emissions to occur, it requires both the presence of the electrons and holes upon the recombination of which the photons are generated. In Chapter 2 we mentioned that the transient absorbance or the differential reflectance signal only requires the existence of any species of carriers. So here if we trust the DR spectrum and believe that charge carriers, no matter which

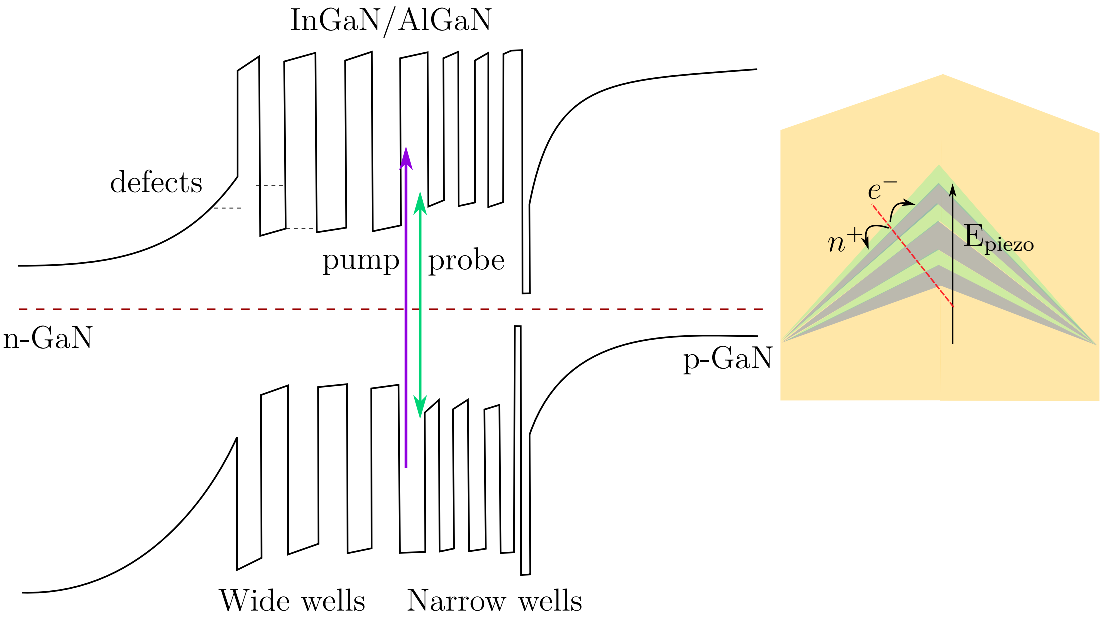

Figure 4.9: An illustrative band diagram of the InGaN quantum well. The right side is an exaggerated illustration of the tilted quantum well in nanowire structure and the left side is the band diagram roughly along the dashed red line on the right. The e and h pairs are created upon the pump excitation. They will relax into the well states before recombination. In the DR experiments the carrier occupation creates a positive DR. Due to the built-in piezo-electric field, the lateral component will cause charge separation.

kind, only have non-negligible occupation at the states indicated by the peaks, there is no straightforward way to have radiation outside the charge carrier occupation spectrum range. To solve the contradiction of spectrum shape widths there are the following possibilities

1. The PL has a very long lifetime while the DR spectrum is transient. There is a possibility that at the wavelengths between the DR peaks there are low charge density states that have a steady supply of charge carriers that come in and recombine. The low carrier density does not have measurable transient DR signal in a few picosecond (ps), but with a steady source of carrier injection, their integration over a full cycle of 4μs RegA interval can become prominent in the total PL spectrum.
2. The broad PL may correspond to not only the photon but also phonon emission spectrum. In other words, upon the recombination of electrons and holes, not only do they create a photon emission, which is the PL, but also one or few phonons. This creates a side band on the red side of the main spectral line (phonon side band).
3. Or we have to give up the assumption that the optical matrix element of the DR spectrum is smooth. Part of the sharp DR spectrum line has the contribution from the optical matrix element.

4.6.2 Low temperature experiments

With the questions about the DR and PL spectrum we carried out the TRPL experiments on the same sample with a Hamamatsu streak camera as described in Chapter 2. (Insert the source streak to characterize the resolution.) The optical setup is a typical PL setup with normal incidence except that the collected PL is directed to a spectrograph and a streak camera so that we are able to measure the dynamics of

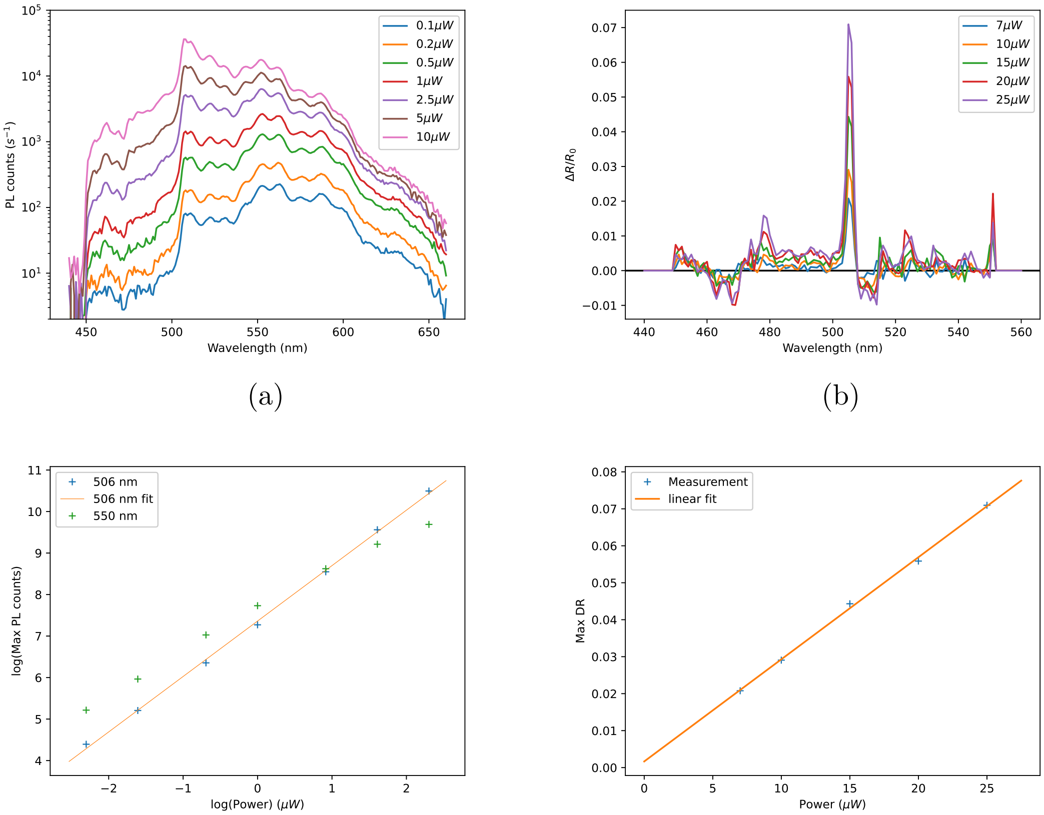

(a) (b)

(c) (d)

Figure 4.10: a The scaling of PL of the quantum well sample (F1921). b The power dependent DR spectrum. c The linear fit of the power dependent PL at 506 nm peak. d The linear fit of the power dependent DR at 506 nm peak.

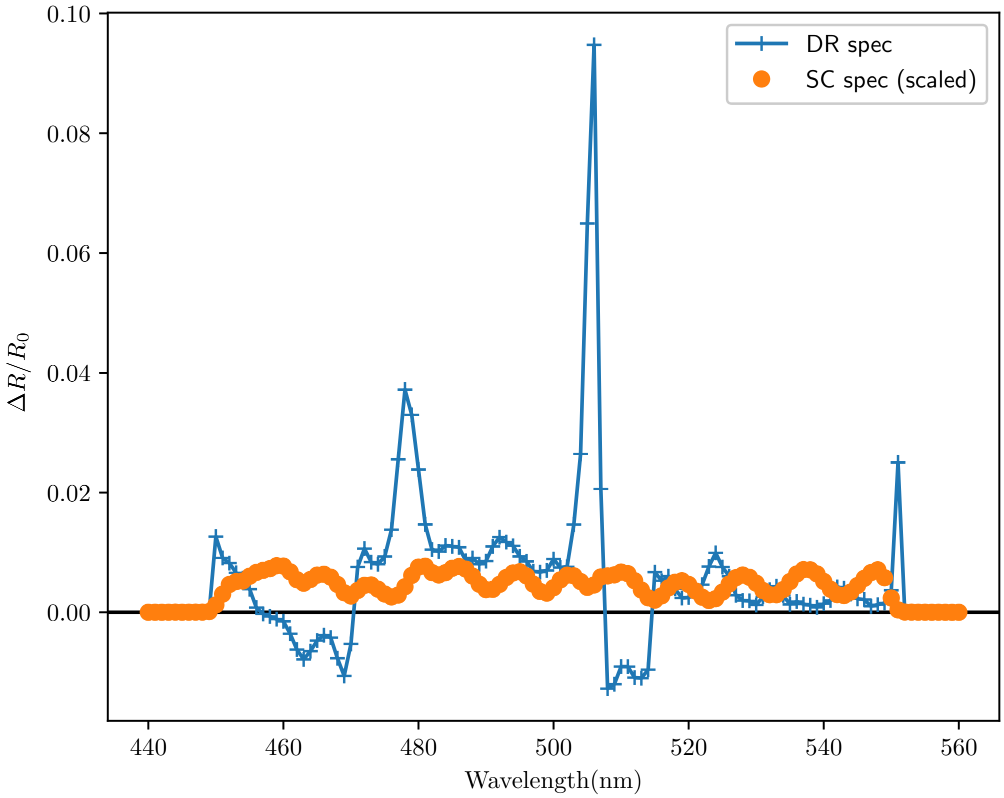

Figure 4.11: The spectral resolved room temperature DR at 5 ps after time zero. It was obtained with 400 nm pump pulses and probed with white light supercontinuum pulses. With the delay between the pump and probe pulses fixed at 5 ps (measured from the fast rising edge), a monochromator on the path of the reflectance of is scanned to obtain the spectral resolved DR. There are two distinct sharp DR peaks, at around 479 nm and 506 nm, respectively, each being bipolar.

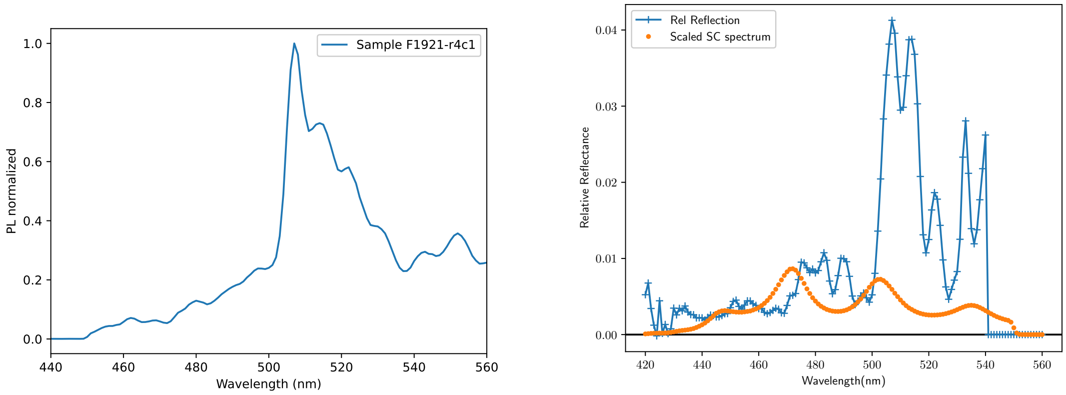

(a) (b)

Figure 4.12: (a) The PL spectrum of the InGaN quantum well in nanowire sample under room temperature. The excitation source is the 400 nm SHG generated with 250 kHz pulses. The major peak on the PL spectrum matches the major peak of the DR spectrum but the PL peak is much broader. Fringes on the PL spectrum show an even spacing of about 30 meV. (b) The (uncalibrated) reflectance spectrum of the same nanowire pattern as shown in the DR and PL spectrums.

each wavelength of the PL emissions. The excitation source is the 400 nm SHG of a Ti:sapphire oscillator that is focused onto the sample with an achromatic doublet lens at normal incidence. The PL is collected with the same lens, and separated with the residual excitation with a dichroic beam-splitter that cuts on at 450 nm. A 450 nm long-pass filter is also inserted at the PL collection path to further reduce the background of excitation source and to protect the photocathode screen and the CMOS camera of the streak camera.

We also further cooled the sample down with liquid nitrogen (LN2) to study the temperature dependent TRPL and phonon related physics. An Oxford Instrument Hi-res Microstat with sapphire window is used to hold the sample in the LN2 temperature. Because practically there was a slight leakage in our system, a turbo pump is continuously running to keep the pressure in the cryostat below the level of 10^{-5} mbar. The sample is first cooled down to 81K by flowing LN2 into the cryostat under atmospheric pressure and a constant flow of LN2 at the same rate is maintained with negative pressure at the vent of the cryostat that drains the evaporated N_2 gas. The sample temperature is controlled with a PID temperature controller that connects a temperature sensor and a heater attached to the cold finger where the sample mounts. After the sample is cooled down to 81 K, which is the lowest temperature achievable by our instruments using LN2, possibly limited by the cryogenic liquid flow rate and the thermal leakage of the vacuum chamber. The temperature of the sample is raised sequentially to 90 K, 100 K, 130 K, 160 K, and 200 K. Since it is not practical to directly measure the sample temperature, the sample will stay still at each of the temperature points for 30 minutes before the PL measurement to ensure thermal equilibrium with the cold finger, where the thermal couple probe of the temperature controller is attached to.

The raw data of temperature-dependent TRPL measured by the streak camera is shown in Fig. 4.14. The streak camera image was measured with sample temperature at 81 K, 90 K, 100K, 130K, 160K, 200K and room temperature, which is 300K. If we look at the PL dynamics of the raw TRPL data, the rising edge of the PL is fast and instrument-limited for all the spectral lines on all the measurements, and the decay time increases with longer emission wavelengths and lower temperature. The streak camera also measured non-zero PL counts before time-zero when the sample is cooled down. This indicates that the PL lifetime is longer than or comparable with the oscillator pulse interval time, which is about 13.2 nanoseconds (corresponding to a repetition rate of 75.8 MHz). The PL count before time-zero consistently increase with lower temperature, indicating that the radiative lifetime increases when the temperature decreases. The 479 nm line did show up on the PL spectrum under all the temperatures but only near the time zero. It was not directly shown in the data presented here, but during the experiment it was visually noticed that the brightness of the PL emission becomes distinctively brighter when the sample is cooled down. Fig. 4.15 shows the integrated PL of the same sample cooled down. At a glance of

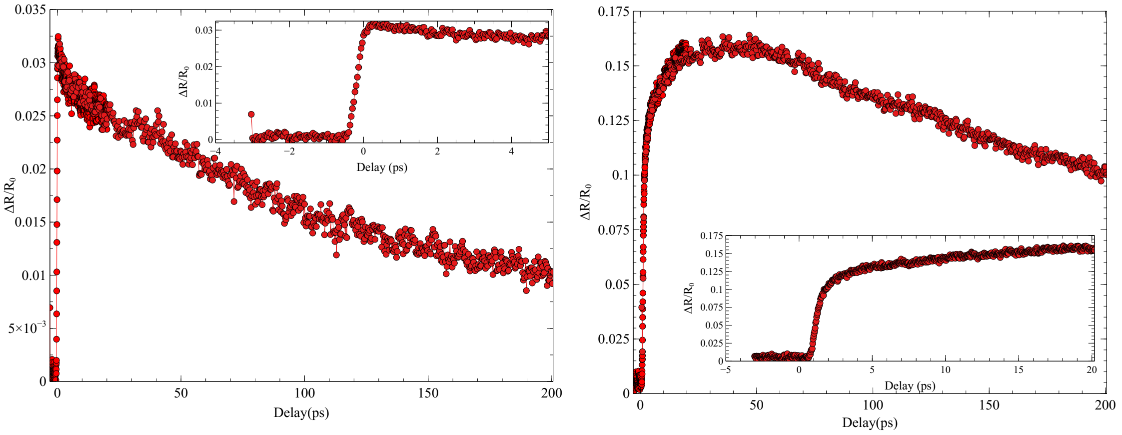

(a)

(b)

Figure 4.13: The time-resolved DR at the two major peaks and the TRPL under room temperature are shown on panel (a) and (b). At the 479 nm (Fig (a)) peak almost only a fast component is detected at the rising edge while at 506 nm peak (Fig (b)), at least a slow rising and a slow decay follows a fast rising edge. The inner sets show the zoomed-in rising edge of each curve, respectively.

the PL spectrum it was found that the PL intensity of the 479 nm line gets lower and the 506 nm line gets higher under low temperature.

4.6.3 Room temperature spectrum

Now with the TRPL data under low temperature we can get back to the fringe feature that appeared in the room temperature PL. If we compare the low temperature PL spectrum with the room temperature PL, the width of the fringe feature does not change. If it were the electronic effects, the fringe pattern that correspond to a series of electronic states should become sharper with weaker homogeneous broadening under low temperature, which contradicts with the experiment data. A similar fringe pattern was also discovered in the room temperature reflectance spectrum shown in Fig. 4.12b, which shows a broadened exciton resonance feature with a fringe modulation of $\sim 20\%$ depth on top. It only makes sense to assume that these fringes are due to pure dielectric features. In order to verify this assumption, we can match the

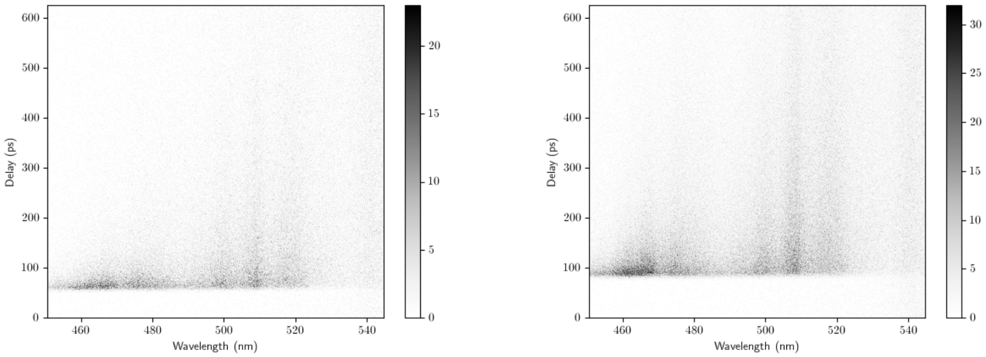

(a) 200 K

(b) 160 K

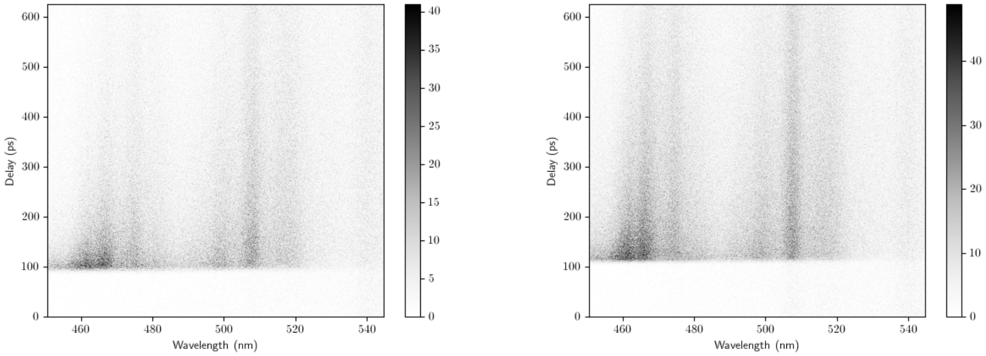

(c) 130 K

(d) 100 K

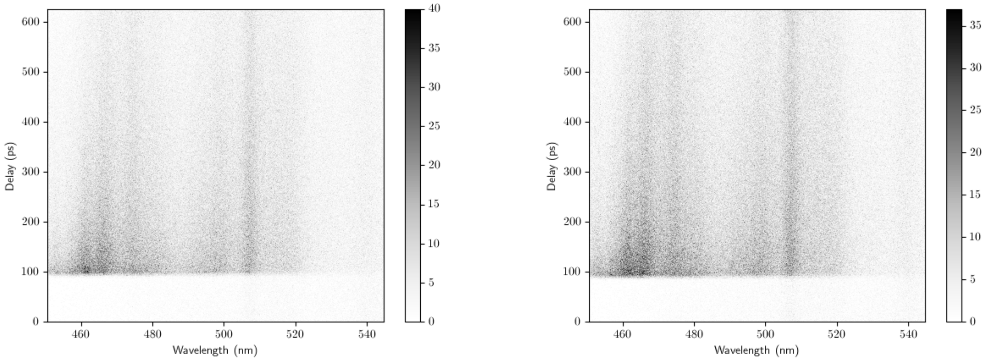

(e) 90 K

(f) 81 K

Figure 4.14: The TRPL spectrum taken by streak camera of the QW in NW sample under temperatures of 200K (a) to 81K (Fig 4.14f). The excitation source is the SHG from a Ti:sapphire oscillator with a repetition rate of 76 MHz at normal incidence and the PL is collected at the normal reflection.

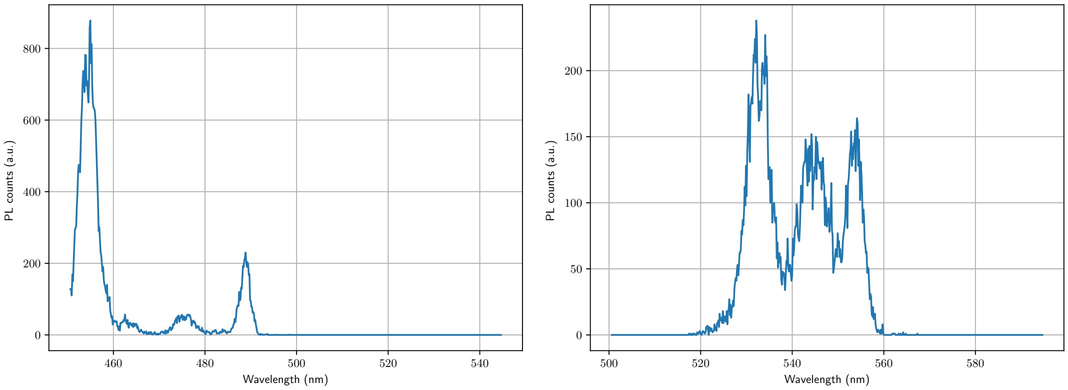

(a) 200 K, 500 nm center (b) 200 K, 550 nm center

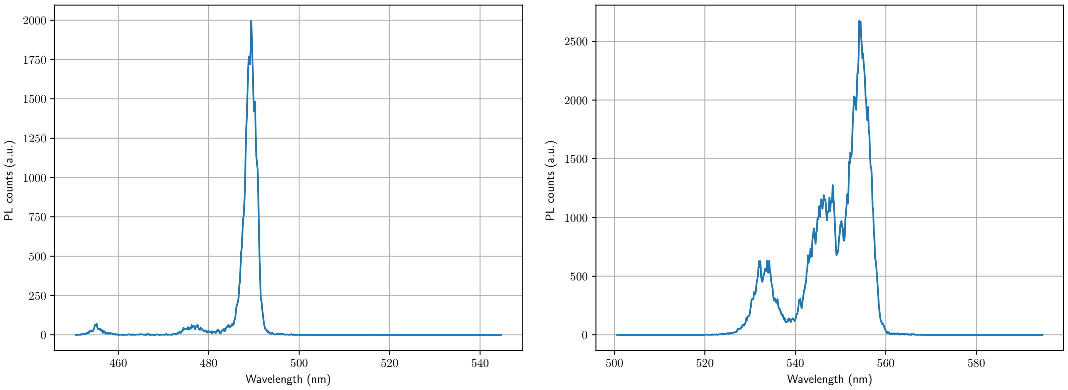

(c) 140 K, 500 nm center (d) 140 K, 550 nm center

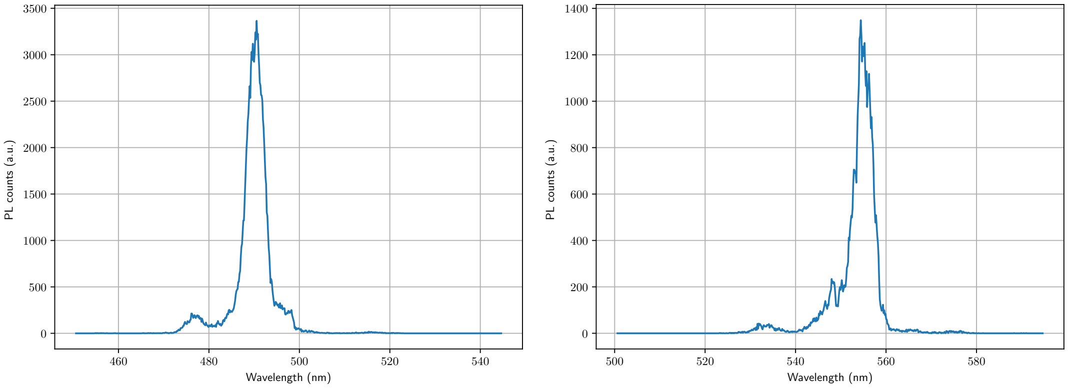

(e) 80 K, 500 nm center (f) 80 K, 550 nm center

Figure 4.15: The time integrated PL measured with the streak camera under focus mode.

peaks with a simple slab shape Fabry-Perot cavity with some thickness d and dielectric function $n(\lambda)$. The interference maximum is attained when the round-trip optical path length of the cavity is a multiple of the wavelength. Therefore, the wavelength of the k-th peak should follow the equation

$$\frac{2n(\lambda_k)}{\lambda_k} = \frac{k}{d} \tag{4.1}$$

Since the majority of the nanowires are consisted of GaN, we use the refractive index of GaN in published dataset[20]. We plot the $\frac{2n(\lambda_k)}{\lambda_k}$ against the peak count k on the PL spectrum, the curve (shown in Fig. 4.16) is almost perfectly linear except for a bump that corresponds to the 506 nm peak. This could be due to a strong exciton resonance that deviates from a simplified dispersion of GaN. From the slope of the linear fit (which should be $1/d$) we can estimate the thickness of the assumed slab cavity to be $d \approx 6.06$nm. Fig. 4.16 also shows the same plot but using the reflectance spectrum from the blank region on the same piece of the sample. The GaN thickness of the blank region is estimated to be $\sim 5\mu$m. The numbers here match with the thickness of the GaN buffer layer (as provided by the manufacturer of the GaN on sapphire wafer) and the length of the nanowires.

4.6.4 Temperature-dependent PL dynamics

In the following discussions we will focus on the dynamics at these two transition energies. The temperature dependent PL relaxation dynamics at these two wavelengths are shown in Fig. 4.17a and 4.17b, which also show the bi-exponential fit to the relaxation curve. The rising edge of the PL is instrument-limited, and the timing of the delay edge does not have a distinctive change through the measured spectral range, meaning that the PL emission start within ~ 1.4 ps after the initial excitation. As we have mentioned earlier about the raw streak camera traces, the

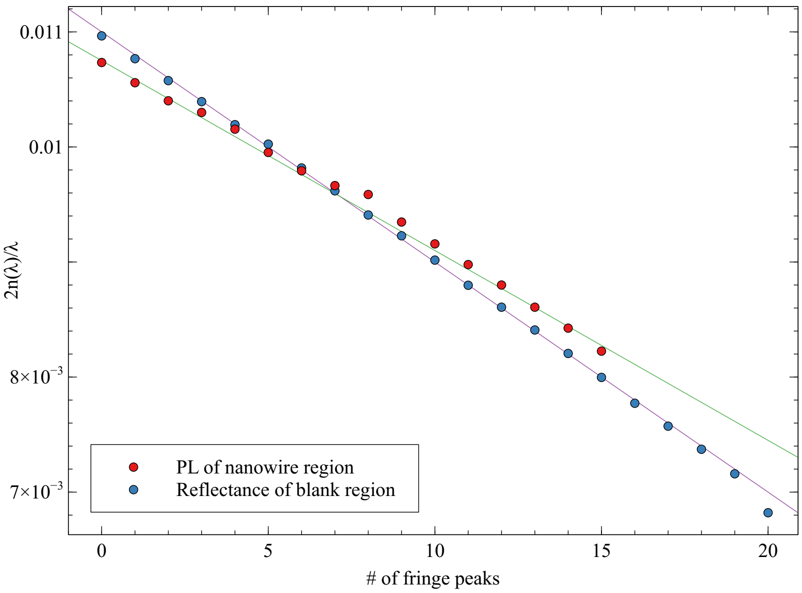

Figure 4.16: The wavenumber of the PL fringes and the reflectance on a blank region of the sample vs the peak index.

PL has a rather slow relaxation component that lasts longer than the pulse interval. Since the experiments presented in this work only covered the first few hundred picoseconds, the very slow decay is effectively a constant background when we study the faster relaxations in sub-ns timescale. Therefore, we have aligned the rising edges and shifted the counting levels in the PL relaxation curves shown in Fig. 4.17. Single exponential function fails to fit most of the relaxation curves except for the room temperature ones. The curves shown in Fig. 4.17a and 4.17b are bi-exponential fits ($f(t) = a_1 \mathrm{e}^{-t/\tau_1} + a_2 \mathrm{e}^{-t/\tau_2}$). The time constants of fits are listed in Table 4.2.

Since the time constant fitting parameters of the slower component turn out to be close to or longer than the window of measurement of the instrument for most of the curves shown in Table 4.2, we believe that they are quantitatively less trustworthy than the fast components. The fast component, however, showed some interesting trends. The decay time of the fast component at 506 nm increases monotonically with decreasing temperature while at 479 nm it has a turning point of $\sim$ 130 K. The integrated PL in Fig. 4.17b shows that the PL peak at 506 nm increases dramatically

Table 4.2: Bi-exponential fit time constant parameters.

Temperature	479 nm		506 nm	
	$\tau_1 (ps)$	τ_2 (ps)	τ_1 (ps)	τ_2 (ps)
81 K	250	804	64	470
90 K	266	878	62	445
100 K	215	1070	58	438
130 K	303	∞	53	360
160 K	113	524	43	325
200 K	64	335	38	290
300 K	11	64	25	N/A (single exp)

under low temperature compared to the other wavelengths. The measurement is also consistent with the observation by bare eyes that the brightness of the PL increases dramatically under low temperature. This indicates that the relaxation of the PL at 506 nm is dominated by coupling into non-radiative states under the temperature near the room temperature. The coupling to non-radiative states shows some thermal activation characteristics: they become faster when the lattice is warmer. We then borrow the Arrhenius's Law from chemical reaction dynamics to study the activation barrier. The Arrhenius's Law states that the reaction rate constant a can be related to the temperature T and an activation barrier energy ϵ by

$$a(T) = A\mathrm{e}^{-\frac{\epsilon}{k_B T}}. \tag{4.2}$$

We can understand this relation by thinking of the probability of a particle in a thermal distribution (which can be approximated by a Maxwell-Boltzmann distribution) occupying a state that has a higher energy than the activation barrier. In the context of chemistry, the exponential part are more commonly written in terms of the activation free energy per mole μ and RT, and it is exactly equivalent to Eq. (4.2). For an ideal system that follows the Arrhenius's Law perfectly, if we plot a curve of $\log a(T)$, in the context of our work, $\log \frac{1}{\tau_1}$, against $\frac{1}{T}$, which is the so-called Arrhenius plot, it should result in a straight line with its slope being the activation barrier energy.

Figure 4.17c and 4.17d show the Arrhenius plot of the quantum well in nanowire sample at the 479 nm and 506 nm peaks, respectively. The $\log \frac{1}{\tau_1}$ vs $\frac{1}{T}$ curve is concave for both 479 nm and 506 nm. For the 506 nm curve, it is still monotonically decreasing. It is possible that the activation barrier is not perfectly defined. In order to approximately characterize the temperature dependent decay dynamics, we applied linear fitting for the high temperature segment and low temperature segment separately. The fitting parameter for the activation barrier (most likely for thermal distributed acoustic phonon) is given by 14.5 meV and 3.4 meV under higher temperature and lower temperature, respectively. This number does not match anything structural in the design but the indium fluctuation. Our best speculation for the activation barrier energy is the local fluctuation of indium concentration. The Arrhenius curve of the 479 nm line is a little more complicated because it start to rise when the temperature goes below 130 K. We believe that there is another mechanism that determines the PL dynamics of the 479 nm emission.

Our initial room temperature studies found that both the PL and DR showed strong resonance at 479 nm (2.6 eV) and 506 nm (2.45 eV) under room temperature. Both the DR and the PL dynamics showed different timescales in these two wavelengths, therefore they belong to two different electronic states. They cannot be attributed to the same transition because the PL decay time are also different. The DR spectrum is sharp for both lines, therefore we believe that these should not be some trap or bulk states but rather some confined quantum well exciton states. Since the timescale of the 479 nm DR decay curve is quite slow and cannot be related to any of the dynamics of the 506 nm, they should be attributed to two different kinds of quantum wells, otherwise the higher level should relax into the lower level within picoseconds because they are more than 100 meV apart. From previous studies

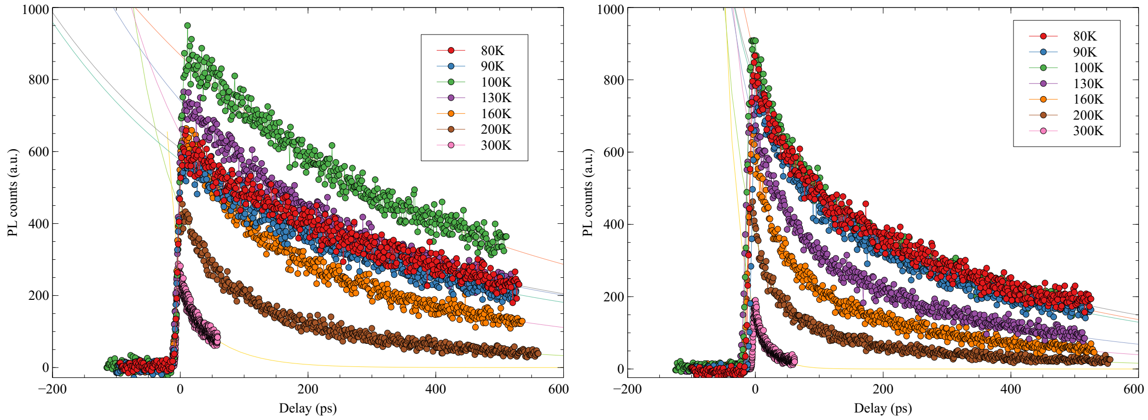

(a) TRPL at 479 nm.

(b) TRPL at 506 nm.

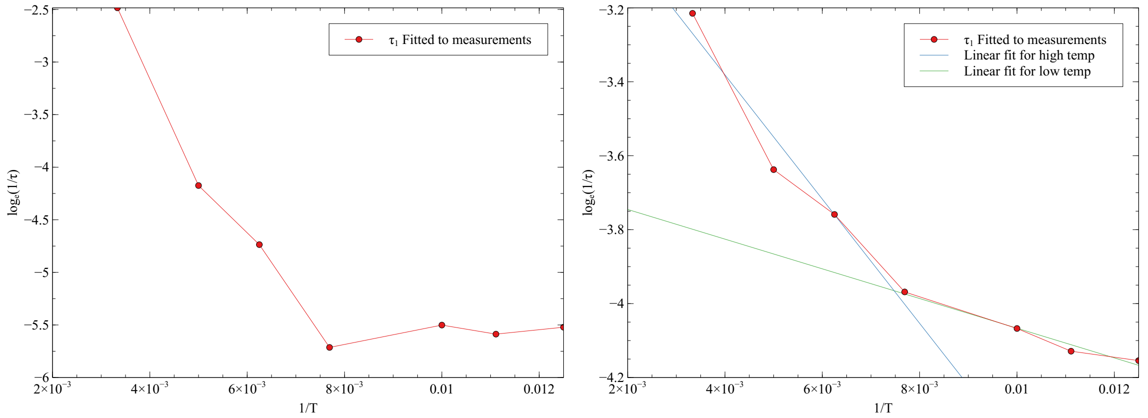

(c) τ_1 fit of 479 nm relaxation.

(d) τ_1 fit of 506 nm relaxation.

Figure 4.17: a and b show the temperature dependent time-resolved PL at 479 nm and 506 nm, respectively. All curves are aligned at time-zero by the initial rising curve and shifted to remove the PL counts before time-zero. The thin lines are the bi-exponential fits. The fast component time constants are plotted in c and d as Arrhenius plots against $\frac{1}{T}$. All measurements are made in one session under the same optical conditions and the streak camera settings.

on the same structure, the growth should be uniform in a same region of selective area epitaxy (SAE) patterns, there is less likely to be two distinct nanowires in the same region than two kinds of quantum wells within the same wire. When we refer back to earlier research on the same structure, it was reported that some variance of exciton central wavelengths between different quantum well layers was observed by cathodoluminescense spectroscopy[6], and SEM microscopy also showed a change in the quantum well thickness from layer to layer in this kind of structure[7], which is consistent with our results.

It is well established from previous research that the radiative recombination come from carriers captured in localized exciton states after off-resonance excitation[21, 22, 23]. The capture process happens in parallel for all the quantum well layers and the coupling between layers can also create complicated dynamics that we do not understand at this stage. But after the capture is completed, we then notice that the DR decay time for both the 479 nm and 506 nm lines are in the hundred picosecend level, while the PL decay time constants for the same transitions are both less than 30 ps in room temperature. This means after about 100 ps from the excitation, the charge carriers that get captured into the quantum well states are can still be probed by the DR signal, but the PL has reduced to a negligible level. The temperature dependent PL dynamics indicated that at room temperature the PL decay is determined by coupling into non-radiative states, but the DR results tells us that the carriers have not yet recombined. We can explain this by spatial charge separation.

In a tilted quantum well structure studied here, the transverse polarization field perpendicular to the quantum well plane is comparatively reduced from *c*-plane quantum wells, but the lateral component may be driving the two species of carrier apart after they have been captured into the quantum well states. The drift driven by the polarization field is limited by both the phonon, defect scattering and local traps. The temperature dependent PL decay dynamics is determined by the stochastic properties of the phonon, defect and the indium concentration fluctuation. We have observed the charge separation in two different types of quantum wells in this structure.

4.6.5 Summary and conclusions

We have studied the PL and the DR spectra and dynamics of InGaN quantum disk in nanowire structures, which contain tilted quantum wells that are expected to have reduced polarization fields, thus giving rise to enhanced PL and making them promising for LED applications. In this section, we synthesize the data presented above into a consistent picture of the structure and dynamics.

The DR spectrum near time-zero shows a narrow feature at two different probe photon energies, indicating that the two optical transitions arise from high-quality quantum wells with very uniform growth across the area probed by the experimental setup. (There are two different sets of quantum wells in the sample, with different widths.) The PL spectrum shows, in addition to emission at the quantum well energies, a very broad feature that is modulated by the Fabry-Perot effect of the top and bottom surfaces of the sample structure. There is no evidence in the spectra or dynamics that indicates that the broad PL feature is related to the quantum well emission – it appears to arise from states that are physically far from the quantum wells in the sample. The most likely interpretation is that this emission comes from localized states in the disordered GaN buffer layer, or the lower portion of the nanowire. These states are not particularly interesting in this study; they simply correspond to a background signal on which is superimposed the quantum-well optical transitions of interest.

For the quantum well transitions, we discovered two key features that provide considerable insight into the behavior of this system, and particularly the role of charge separation:

1. At room temperature, the dynamics of the two quantum-well transitions for

the DR both show a slow few hundred ps dynamics, while the PL at the corresponding emission lines exhibit a decay component of about 10 ps that is not observed in the DR dynamics.

2. The temperature-dependent PL dynamics of the quantum well transitions were found to slow down when the sample temperature is lowered to liquid nitrogen temperatures.

Our proposed interpretation is as follows.

1. The DR signal is proportional to the total carrier density in the quantum wells (as it is proportional to $f_e + f_h$); the electron and holes may be physically separated due to transport following photoinjection, but this will not appear in the DR signal. On the other hand, the PL signal is proportional to the product of the occupations ($f_e \cdot f_h$), and the electron and hole must be in the same physical location for recombination to occur. The presence of a fast decay component in the PL that does not appear in the DR implies that the integrated carrier density does not change rapidly in the quantum well (i.e. the decay is not due to trapping at defects), but the charges must be separating within the quantum well, producing a decay in the PL.

2. The slow components of the PL and DR dynamics are of the same magnitude (even though the densities are different), and we attribute the slow component to recombination. The recombination lifetime at room temperature is largely determined by non-radiative channels, as the quantum efficiency is much higher at low temperatures.

3. The PL decay rate decreases at lower temperature. The T-dependence shows a complex activation behavior, in that the PL decay (charge separation) is thermally activated, but not by a single energy, as the Arrhenius plots are not

linear. The nonlinear behavior arises from a distribution of activation energies in the system. Fitting different regions of the Arrhenius plots does show that the activation energies are on the order of a few meV to about 14 meV. This range of activation energies most likely arises from In-composition fluctuations in the quantum wells, i.e. alloy disorder.

4. The separation of charge in the lateral direction along the quantum wells implies the presence of a residual strain leading to a polarization field along the tilted wells.

The picture that emerges is that, following photoexcitation, the hot carriers quickly cool to near the band edge by optical phonon emission. At low temperatures, the carriers are trapped in potential fluctuations due to alloy disorder, where they radiatively recombine with high efficiency. As the temperature is increased, carriers are thermally excited out of these potential fluctuations, where they may separate laterally in the quantum well due to internal polarization fields. This is manifested as a decay component in the PL of 10–20 picoseconds. The DR signal shows only the total recombination. Because carriers may be trapped by defects near the surface following carrier separation, the radiative efficiency reduces at higher temperature.

The observation of lateral charge separation in very high quality InGaN quantum wells by comparison of the PL and DR dynamics is a novel way to probe the phenomenon of charge separation in these systems. As discussed throughout this thesis, charge separation lies fundamentally at the origin of photovoltaic systems as well as many photocatalytic systems. This effect is also important for LED's, as it would serve as a parasitic effect to be avoided in order to achieve high emission quantum efficiency.

BIBLIOGRAPHY

[1] Y. C. Shen, G. O. Mueller, S. Watanabe, N. F. Gardner, A. Munkholm, and M. R. Krames, “Auger recombination in InGaN measured by photoluminescence,” Appl. Phys. Lett., vol. 91, p. 141101, Oct. 2007.

[2] D. S. Chemla and D. a. B. Miller, “Room-temperature excitonic nonlinear-optical effects in semiconductor quantum-well structures,” J. Opt. Soc. Am. B, JOSAB, vol. 2, pp. 1155–1173, July 1985.

[3] D. A. B. Miller, D. S. Chemla, T. C. Damen, A. C. Gossard, W. Wiegmann, T. H. Wood, and C. A. Burrus, “Band-Edge Electroabsorption in Quantum Well Structures: The Quantum-Confined Stark Effect,” Phys. Rev. Lett., vol. 53, pp. 2173–2176, Nov. 1984.

[4] S. Y. Karpov, “Suppression of phase separation in InGaN due to elastic strain,” MRS Internet Journal of Nitride Semiconductor Research, vol. 3, p. 16, Dec. 1998.

[5] A. D. Bykhovski, B. L. Gelmont, and M. S. Shur, “Elastic strain relaxation and piezoeffect in GaN-AlN, GaN-AlGaN and GaN-InGaN superlattices,” Journal of Applied Physics, vol. 81, pp. 6332–6338, May 1997.

[6] S. Cheng, B. Langelier, Y.-H. Ra, R. Tonny Rashid, Z. Mi, and G. A. Botton, “Structural origin of the high-performance light-emitting InGaN/AlGaN quantum disks,” Nanoscale, vol. 11, no. 18, pp. 8994–8999, 2019.

[7] S. Cheng, Z. Wu, B. Langelier, X. Kong, T. Coenen, S. Hari, Y.-H. Ra, R. T. Rashid, A. Pofelski, H. Yuan, X. Li, Z. Mi, H. Guo, and G. A. Botton, “Nanoscale Structural and Emission Properties within “Russian Doll”-Type InGaN/AlGaN Quantum Wells,” Advanced Optical Materials, vol. 8, no. 17, p. 2000481, 2020.

[8] A. Kirubakaran, S. Jain, and R. K. Nema, “A review on fuel cell technologies and power electronic interface,” Renewable and Sustainable Energy Reviews, vol. 13, pp. 2430–2440, Dec. 2009.

[9] A. Fujishima and K. Honda, “Electrochemical Photolysis of Water at a Semiconductor Electrode,” Nature, vol. 238, pp. 37–38, July 1972.

[10] Y. Li and J. Zhang, “Hydrogen generation from photoelectrochemical water splitting based on nanomaterials,” Laser & Photonics Reviews, vol. 4, no. 4, pp. 517–528, 2010.

[11] M. César, Y. Ke, W. Ji, H. Guo, and Z. Mi, “Band gap of InxGa1-xN: A first principles analysis,” Appl. Phys. Lett., vol. 98, p. 202107, May 2011.

[12] M. Liu, L. Tan, B. Zhou, L. Li, Z. Mi, and C.-J. Li, “Group-III Nitrides Catalyzed Transformations of Organic Molecules,” Chem, vol. 7, pp. 64–92, Jan. 2021.

[13] D. Wang, A. Pierre, M. G. Kibria, K. Cui, X. Han, K. H. Bevan, H. Guo, S. Paradis, A.-R. Hakima, and Z. Mi, “Wafer-Level Photocatalytic Water Splitting on GaN Nanowire Arrays Grown by Molecular Beam Epitaxy,” Nano Lett., vol. 11, pp. 2353–2357, June 2011.

[14] M. G. Kibria, F. A. Chowdhury, S. Zhao, B. AlOtaibi, M. L. Trudeau, H. Guo, and Z. Mi, “Visible light-driven efficient overall water splitting using p-type metal-nitride nanowire arrays,” Nat Commun, vol. 6, p. 6797, Apr. 2015.

[15] S. Krishnamoorthy, F. Akyol, and S. Rajan, “InGaN/GaN tunnel junctions for hole injection in GaN light emitting diodes,” Appl. Phys. Lett., vol. 105, p. 141104, Oct. 2014.

[16] S. Krishnamoorthy, D. N. Nath, F. Akyol, P. S. Park, M. Esposto, and S. Rajan, "Polarization-engineered GaN/InGaN/GaN tunnel diodes," Appl. Phys. Lett., vol. 97, p. 203502, Nov. 2010.

[17] M. G. Kibria, S. Zhao, F. A. Chowdhury, Q. Wang, H. P. T. Nguyen, M. L. Trudeau, H. Guo, and Z. Mi, "Tuning the surface Fermi level on p-type gallium nitride nanowires for efficient overall water splitting," Nat Commun, vol. 5, p. 3825, Apr. 2014.

[18] L. Hsu, R. E. Jones, S. X. Li, K. M. Yu, and W. Walukiewicz, "Electron mobility in InN and III-N alloys," Journal of Applied Physics, vol. 102, p. 073705, Oct. 2007.

[19] P. Parkinson, C. Dodson, H. J. Joyce, K. A. Bertness, N. A. Sanford, L. M. Herz, and M. B. Johnston, "Noncontact Measurement of Charge Carrier Lifetime and Mobility in GaN Nanowires," Nano Lett., vol. 12, pp. 4600–4604, Sept. 2012.

[20] A. S. Barker and M. Ilegems, "Infrared Lattice Vibrations and Free-Electron Dispersion in GaN," Phys. Rev. B, vol. 7, pp. 743–750, Jan. 1973.

[21] F. Chen, A. N. Cartwright, H. Lu, and W. J. Schaff, "Time-resolved spectroscopy of recombination and relaxation dynamics in InN," Appl. Phys. Lett., vol. 83, pp. 4984–4986, Dec. 2003.

[22] M. Smith, G. D. Chen, J. Y. Lin, H. X. Jiang, M. Asif Khan, and Q. Chen, "Time-resolved photoluminescence studies of InGaN epilayers," Appl. Phys. Lett., vol. 69, pp. 2837–2839, Nov. 1996.

[23] C.-K. Sun, F. Vallée, S. Keller, J. E. Bowers, and S. P. DenBaars, "Femtosecond studies of carrier dynamics in InGaN," Appl. Phys. Lett., vol. 70, pp. 2004–2006, Apr. 1997.

CHAPTER 5

Summary, Conclusions and Future Work

In this thesis we have presented the ultrafast charge carrier separation and relaxations in three different nanostructures with ultrafast optical spectroscopy.

5.1 CVD MoS_2/graphene heterostructure

We have discovered very fast initial charge transfer from graphene to MoS_2 with the differential reflectance pump-probe technique, which indicates very efficient charge transfer, validating our initial guess. Our spectral-resolved DR near time-zero revealed a spectral shift of the exciton peak, which may correspond to a different screening conditions from direct carrier injection in the MoS_2 monolayer, therefore we argue that only one species of carrier transferred over, making the electrons and separated. Based on our previous knowledge, it should be the electrons that transferred over. Therefore, the proposed improvement by replacing one layer with MoS_2 monolayer is in principle a promising solution. We then studied the transfer back dynamics and found that the decay curve has a very long tail that can only be fitted with an ensemble of transfer rates that follows a Porter-Thomas distribution. This was explained by the disorder in the CVD grown MoS_2 according to the theory that explained the PTD of luminescence oscillator strength in low temperature III-V systems. After the initial separation and thermalization, the decay dynamics is completely governed by the disorder. The separated charges can take a relatively long time before they fully recombine. It may contribute to a higher responsivity of the phototransistor, in the meantime, also inhibit the bandwidth of its operation.

To sum up, our understandings before the work of this dissertation are:

- We know that charge transfer could have happened in the pure CVD-graphene photodetectors that contributes to the prolonged carrier lifetime and increased photo-responsivity but the transfer timescale was unclear.
- Previous experiments on exfoliated 2D TMD material heterostructures discovered fast interlayer charge transfer between monolayer TMDs (WS_2/MoS_2 and $MoS_2/MoSe_2$) or from TMD layer to graphene that happen in sub-100 fs timescale.

The contributions of this work are

- We observed efficient charge transfer from graphene to MoS_2 for the first time through ultrafast pump-probe experiments.
- The charge transfer was found to happen instantaneously after excitation, which is consistent with the other similar heterostructure systems.
- We studied the transfer-back dynamics of the heterostructure consisted of CVD-grown monolayers and found that the disorder dominates the transfer-back process. We modeled it with a simple Porter-Thomas distributed transfer rate after the initial thermalization.

The future works can focus on either the material growth for more controllable material quality, or on the device design to verify the idea in real applications, or on the fundamentals such as complete microscopic modeling of the carrier dynamics and the experiments with different barriers and bias levels across the two layers.

5.2 Self-organized InGaN nanowires

Before the study of this work we knew that self-organized InGaN nanowires have surface band bending that will greatly impact the hot carrier densities and the photochemical reaction efficiency. When the nanowires are p-doped, the band bends down toward the sidewall surface, driving the electrons toward the surface and the holes away from the surface. Ultrafast pump-probe experiments were conducted to study the hot carrier dynamics but with the pump-probe data alone, we could not have a convincing interpretation of the different physical processes. As an initial experimental study on the intrinsic characterization of InGaN nanowires, we have made the first TRDR and TRPL measurements of the photocatalytic InGaN nanowires. Under significant inhomogeneous broadening the DR measure the total remaining photocarrier density and the PL measures the recombination rate that corresponds to colocated electron and hole density. The carrier relaxation can be explained with processes in three different kinds of time constants that are fast (a few ps), medium fast (tens of ps) and slow (more than a few hundreds of ps). By comparing the p-doped and intrinsic nanowires grown under the same conditions we find that the fastest few-ps component only appear in the TRPL of InGaN nanowire samples that are p-doped with Mg, and never in the DR decay curve. We argue that the fast component corresponds to the charge separation driven by the band bending near the nanowire side wall. The previously reported diffusion rate and the nanowire size are consistent with the time constants we measured. The medium time constants are attributed to the recombination in the bulk InGaN and the slow process is the trapping to the surface. We preliminarily identified that the hot carriers arrive at the nanowire surface by diffusion in a few picoseconds.

The physics picture presented here still needs more careful verification. Further, the goal of the ultrafast study is to find the arrival time of the chemical reaction center but in the study presented in this thesis, we are only capable of probing the bulk InGaN states. In the future, directly probing the surface states, probing the chemical decorations on the surface or making an epitaxial shell layer will give more sensible results for the photocatalysis applications. Nonetheless, we may develop newer nanostructures for making the photocatalysts, and in the case that the epitaxial shell growth is challenging to implement, the methodology presented here will still be relevant for characterizing the charge separation in photocatalyst nanostructures.

5.3 InGaN quantum well in nanowires

On the spectroscopy side, we studied the PL and the DR spectra of these quantum well in nanowire structures. The DR spectrum near time-zero shows a narrow feature at two different probe photon energies, indicating that the two optical transitions have uniform growth across the area probed by the experimental setup. The PL spectrum shows a rather broad feature that is largely modulated by the Fabry-Perot effect of the top and bottom surfaces of the nanowire samples.

On the dynamics side, we found a similar fast decay component in the room temperature PL of the quantum well system that is not detected in the DR measurements. The temperature-dependent decay dynamics of the PL shows thermal activation feature that can be partially explained with the Arrhenius's Law. The charge carriers can get activated by thermal energy to couple with non-radiative centers that are still probed by the DR measurements. We find that the activation barrier is so low that it only be matched with the indium concentration fluctuation. We believe that the polarization field in the nanowires played a role in driving the two species of carriers laterally toward the opposite sides of the tilted quantum wells. The fast component of the TRPL decay curve corresponds to the hopping transport of carriers along the quantum well plane.

Before the studies of this work, our understandings about the InGaN based LEDs are

- In the SAE grown quantum disk in nanowire samples, it was observed that the alternating quantum well interface align with a tilted crystal plane. Due to reduced piezoelectric polarization across the direction of the quantum confinement, the reduced QCSE will lead to increased radiative recombination efficiency.
- The main impact factor for LED efficiency was unclear.

The main contributions of this work are

- Combining the room temperature TRPL and TRDR measurements, we were able to identify the main peaks in the PL spectrum to be corresponding to the different quantum well regions.
- By analyzing the low temperature TRPL data, we have observed spatial charge separation. Considering the geometry of the nanowires, these are attributed to the charge separation along the tilted quantum well plane driven by the lateral piezoelectric polarization.
- Following the study with the self-organized nanowires, we argue that the combination of time-resolved PL and pump-probe experiments is a novel approach for characterizing charge separation for InGaN based nanostructure systems.

The next step of this study would be a more sophisticated modeling of the excitonic states, the carrier dynamics and the dielectric properties to fully address the spectroscopy and the time-resolved results. We are still ambiguous about the broad PL spectrum, reflectance spectrum but a very narrow DR spectrum. Experimentally further studies about the coupling between the quantum wells by resonant excitation tuned to one of the sharp DR peaks should reveal more physics in these quantum well systems. On the material side, we found that although not due to QCSE, the piezoelectric effect will nonetheless affect the radiative recombination negatively by driving the two kinds of carriers toward opposite directions along the quantum well. A true nonpolar InGaN quantum well will be both challenging and rewarding for an LED device.